

# Correlated and Further Dynamics in Proteins by NMR Spectroscopy

Dissertation

for the award of the degree

*"Doctor rerum naturalium" (Dr. rer. nat.)*

Division of Mathematics and Natural Sciences

of the Georg-August-Universität Göttingen

submitted by

Korvin Walter

from Rheine

Göttingen 2011

Prof. Dr. Christian Griesinger (Reviewer)  
Max-Planck-Institut für biophysikalische Chemie,  
Abteilung für NMR-basierte Strukturbiologie

Prof. Dr. Claudia Steinem (Reviewer)  
Fakultät für Chemie an der Georg-August-Universität Göttingen  
Abteilung für biomolekulare Chemie

Prof. Dr. Helmut Grubmüller  
Max-Planck-Institut für biophysikalische Chemie,  
Abteilung für theoretische und computergestützte Biophysik

Date of oral examination: 15th of September 2011

It is declared that the presented thesis has been written independently and with no other sources and aids than quoted.

Göttingen, 29th july 2011

Korvin Walter





# Acknowledgement

This work would not have been possible without the support of many people, to which I want to express my deepest gratitude:

Prof. Christian Griesinger for giving me the opportunity to work on these very interesting projects and his continuous encouragement, advice and guidance.

Prof. Claudia Steinem and Prof. Helmut Grubmüller for their inspirational and helpful discussions at my thesis committee meetings.

Dr. Donghan Lee for teaching me so much about the handling of the spectrometers and the pulse sequence design and his invaluable support.

Dr. Stefan Becker, Karin Giller, Ann-Kathrin Brückner and Yvonne Laukat for providing all protein samples in an excellent quality.

Dr. Michael Sabo for a very nice cooperation on the methyl ccr project, many interesting discussions and for proofreading this thesis.

Dr. Adam Mazur for his help with the calculation of the cross-correlated relaxation and cross-relaxation rates.

Dr. Nils-Alexander Lakomek for introducing me to the experimental NMR spectroscopy and the RDC-based model free approach.

Manuel Schmidt for his help creating polyacrylamide gels.

David Ban for proofreading this thesis and for many helpful discussions.

Our colleagues from the theoretical and computational side, Prof. Xavier Salvatella, Dr. Bryn Fenwick, Prof. Bert de Groot, Prof. Raphael Brüsweiler, Dr. Dong Long, Prof. Jens Meiler and Prof. Eva Meirovitch, for our very interesting, informative and fruitful cooperations.

All my colleagues in the department and especially the guys in the cubicle for the great working environment.

Finally, I thank my parents, my brother and sister for their interest in my work and their moral support.

# Contents

<b>Acknowledgement</b>	<b>v</b>
<b>1 Introduction</b>	<b>1</b>
<b>2 Evaluation of the SCRM Method</b>	<b>7</b>
2.1 Introduction . . . . .	7
2.2 Theory . . . . .	9
2.3 Material and Methods . . . . .	10
2.4 Results and Discussion . . . . .	14
2.4.1 Synthetic Structural Noise . . . . .	14
2.4.2 Rosetta created Structures . . . . .	16
2.5 Summary and Outlook . . . . .	19
<b>3 Development of new NMR Experiments for the Measurement of Cross- Correlated Relaxation Rates</b>	<b>21</b>
3.1 Introduction . . . . .	21
3.2 Theory . . . . .	23
3.3 Correlated Motions of the Protein Backbone . . . . .	34
3.3.1 Material and Methods . . . . .	34
3.3.2 Comparison with predictions . . . . .	37
3.3.3 Results and Discussion . . . . .	38
3.4 Correlated Motions between Secondary Structure Elements . . . . .	42
3.4.1 Material and Methods . . . . .	42
3.4.2 Results and Discussion . . . . .	46
3.5 Long-Range Correlated Motions . . . . .	49

3.5.1	Material and Methods . . . . .	50
3.5.2	Results and Discussion . . . . .	53
3.6	Summary and Outlook . . . . .	54
<b>4</b>	<b>Quantitative NOE Buildups as an Indicator for Protein Dynamic</b>	<b>57</b>
4.1	Introduction . . . . .	57
4.2	Theory . . . . .	58
4.3	Material and Methods . . . . .	62
4.4	Results and Discussion . . . . .	64
4.5	Summary and Outlook . . . . .	68
<b>5</b>	<b>Investigations of Membrane Proteins in Hydrophobic Environments for Solution NMR</b>	<b>71</b>
5.1	Introduction . . . . .	71
5.2	Material and Methods . . . . .	72
5.3	Results and Discussion . . . . .	74
5.3.1	The Bicelle Composition . . . . .	74
5.3.2	The Protein Structure of OmpX in Bicelles . . . . .	78
5.3.3	The Membrane Protein - Bicelle Interface . . . . .	81
5.4	Summary and Outlook . . . . .	84
<b>6</b>	<b>Appendix</b>	<b>87</b>
	<b>Table of Abbreviations</b>	<b>87</b>
	<b>Pulseprograms</b>	<b>90</b>
	<b>Bibliography</b>	<b>131</b>
	<b>Curriculum Vitae</b>	<b>141</b>

# Chapter 1

## Introduction

This thesis treats several approaches for the investigation of proteins by solution state nuclear magnetic resonance (NMR) spectroscopy. NMR spectroscopy aside from x-ray crystallography is the only technique which is able to investigate biological molecules with atomic resolution. While the other two mentioned methods can only be applied to molecules in a solid phase, with NMR spectroscopy it is possible to study molecules in solution. This is especially interesting for the research on biological macromolecules under approximately physiological conditions. Also, for the investigation of the dynamical behavior of macromolecules NMR spectroscopy is a very powerful tool [1]. It is the only technique which can measure motional amplitudes of specific time ranges for individual atoms or internuclear vectors. Since the operation of a protein is often strongly depending on structural changes, the knowledge about the protein's dynamics are important for the understanding of its functionality.

In a first part of this study, three NMR parameter, residual dipolar couplings (RDCs), cross-correlated relaxation (CCR) rates and cross-relaxation rates were utilized for the investigation of different aspects of protein's dynamics. For many years there are many NMR experiments established to measure the amplitudes of protein dynamics for several time windows [1]. Using longitudinal relaxation ( $R_1$ ), transversal relaxation ( $R_2$ ) and the heteronuclear Nuclear Overhauser Effect (NOE) motion faster than the rotational correlation time ( $\tau_c$ ) can be detected [2, 3, 4]. The limiting  $\tau_c$  depends on the global rotation of the protein and therefore it depends on its size (the correlation time for constant temperature and solvent is approximately proportional to the mass) as well as on the solution conditions, but is in general in the ns time range. Local bond motion, but also the motion of flexible side chains and loop regions can occur on this time scale. Due to the large number of sampled states of such motion, it contributes strongly to the entropy of the protein [5, 6, 7, 8, 9], what is especially interesting regarding the entropies contribution to the binding of the proteins with other molecules [10, 11, 12, 13]. Relaxation dispersion experiments rely on chemical shift changes of the observed nuclei due to conformational changes [14, 15, 16].

In this way it is possible to measure motion in the time range between  $\mu\text{s}$  and  $\text{ms}$ . Conformational changes in this time range have been shown to be very important for catalytic processes in several proteins [17, 18, 19, 20, 21, 22, 23, 24, 25, 26]. The transition rates for conformational changes in the  $\text{ms}$  time range with clearly dispersed chemical shifts of the conformers can be measured by exchange experiments, while even slower structural changes can be measured in a real time manner by a series of consecutive experiments. For example, in this way hydrogen - deuterium exchange processes with the solvent can be measured to detect local or global unfolding [27, 28].

However, the time window between the rotational correlation time and  $\mu\text{s}$  was invisible for NMR spectroscopical methods, until in the last years new methods were established to use residual dipolar couplings (RDCs) to detect dynamics. RDCs are through space interactions between two nuclei and their size depends on the angle of the internuclear vector to the static magnetic field of the spectrometer. Hence, dynamical changes in the orientation of the internuclear vector are reflected in the averaged measurable RDCs. Since in an isotropic rotating molecule all orientations are equally populated, the dipolar couplings are averaged to zero. To measure RDCs it is necessary to induce an imbalance in the population of the orientations [29, 30]. This can be achieved by dissolving the protein in an anisotropic medium as for example liquid crystalline phases or polyacrylamide gels with anisotropic stretched cavities [31, 32, 33, 34, 35, 36]. The RDCs are averaged over all motion faster than around 20  $\text{ms}$  and therefore are able to close the former gap between the rotational correlation time  $\tau_c$  and  $\mu\text{s}$ , which is also called the supra- $\tau_c$  motion. Using RDC based methods it has been proposed that the supra- $\tau_c$  motion is important for the recognition process of biological macromolecules [37, 38, 39, 40, 41]. Several kinds of approaches are used to extract the dynamical informations from the RDCs. In the first place, RDCs can be used as restraints for the creation of structural ensembles, which can display the dynamical behavior up to  $\text{ms}$  [37, 42, 38]. In a second approach, the RDCs can be fit to specific motional model as for example the three-dimensional Gaussian Axial Fluctuation (3D GAF) [43, 44]. Thirdly there are approaches which calculate parameters of the dynamics like the motional amplitude or the strength of the motional anisotropy without using explicit assumptions about the motional modes. Such methods are the Direct Interpretation of Dipolar Couplings (DIDC) approach from the Group of Prof. Tolman [45] or the RDC-based model-free approach developed in the groups of Prof. Griesinger and Prof. Brüschweiler [46, 47, 48, 49]. The latter one was the topic of the research presented in chapter 2. For the application of the model-free approach extensive data sets of RDCs in various alignment media are needed. From the RDC data of each alignment medium the alignment tensor is determined, which describes the strength and direction of the anisotropic alignment of the medium. With sufficient RDC data sets and the according alignment tensors the motional amplitude and other parameters can be calculated. But for the determination of the alignment tensors the structure of the protein has to be known. Hence, structural noise on this structure

affects the precision of the resulting motional amplitudes [50, 51, 52, 53]. For this reason the model-free approach was extended to the self-consistent RDC based model free (SCRM) approach [49]. The SCRM approach use the informations about the average orientations of the internuclear vectors from the RDCs in an iterative manner to alleviate the structural noise from the used protein structure. In this study the ability of the SCRM approach to compensate structural noise is examined by two test scenarios with artificially constructed noisy structures.

By using the RDCs as restraints the recently created protein structural ensembles of the model protein ubiquitin [37, 42] should present a realistic description of the motional amplitudes for dynamics up to ms. Nevertheless, other aspects of the dynamical behavior are more difficult to validate experimentally. The RDC-based structural ensembles show strong correlated motion. For example, the EROS ensemble [37] displays a very distinct correlated motion between the  $\alpha$ -helix and the loop between two  $\beta$ -strands, which move concerted in a pincer like motion. The measurement of correlated motion on an atomic resolution is a very challenging task, which was attempted in chapter 3. As a probe for correlated motion cross-correlated relaxation (CCR) rates can be utilized. Cross-correlated relaxation occurs if a coherence is affected by two different relaxation processes which interfere with each other. Such relaxation processes can be dipole-dipole interactions between two nuclei or chemical shift anisotropy effects. For the measurement of correlated motion the dipole-dipole interactions are preferred, since they are simpler and don't require knowledge about the potentially conformation dependent chemical shift anisotropy. Dipolar interactions are fully understood, always axially symmetric with the internuclear vector being the symmetry axis. Since the size of the CCR rates depend on the angle between the direction of the two relaxation effects, for the cross-correlated relaxation of two dipole-dipole processes the angle between the two atom pairs of these relaxation processes can be probed [54, 55, 56]. Since different correlated modes lead to different changes in the intervector angle spanned between the two atom pairs, this has to be reflected in the dynamically averaged CCR rates [57, 58, 59, 60]. In this study several CCR experiments were developed and applied to measure CCR rates between atom pairs at specific sites of the protein. The challenge for such experiments is the generation of the double and zero quantum coherence between the two atom pairs which is necessary for a cross-correlated effect of the two relaxation processes. For atom pairs which are separated by only few bonds the build up of such a double and zero quantum coherence can be achieved in an effective manner using scalar couplings [58, 61]. But such CCR rates are very limited for the investigation of long range correlated motion. To detect informations about global correlated motions of the protein, CCR rates between two atom pairs on separated sites of the protein, for example two  $\beta$ -strands in the  $\beta$ -sheet or on two side chains. For such experiments the build up of the double and zero quantum coherence has to be achieved by a through space transfer from one atom pair to the other one. Possible transfer mechanisms are residual dipolar couplings, cross relaxation

[62] or a so called relaxation-allowed coherence transfer (RACT) [63], which are based on a cross-correlated relaxation process. Most of the through space transfer processes used in this study had sizes smaller than 10 Hz. Compared to other experiments which use scalar couplings along one or three bonds, the through space transfers are much less efficient. Especially since the double and zero quantum coherence has to become refocused through a second transfer step. The low transfer amplitudes make such experiments very insensitive. In this study experiments were applied and developed, which use scalar or residual dipolar couplings, cross relaxation or RACT processes for the transfers to measure CCR rates in the protein backbone, between opposing  $\beta$ -strands and between side chains in the hydrophobic core of the protein.

Aside from the residual dipolar couplings used in chapter 2 and cross-correlated relaxation rates in chapter 3, cross-relaxation rates can be used for the determination of protein dynamics. Cross relaxation describes a relaxation effect on a nucleus caused by the non-equilibrium state of a second nucleus. In this way magnetization can be transferred from one nucleus through space to another one which is known as the Nuclear Overhauser Effect (NOE) [62]. NOEs are one of most important parameters for structure determination by solution state NMR spectroscopy. NOESY experiments deliver an efficient way to obtain long range informations for distances of up to 5 Å and are very helpful for the determination of the secondary and tertiary protein structure. But in addition to these structural informations, the cross-relaxation rates also comprehend informations about the protein's dynamics. Under the commonly used assumption of isotropic molecular tumbling of the proteins, the cross-relaxation rates depend only on distance. If there is dynamics that affects the distance, this will be reported in the NOE. Also angular fluctuations of the internuclear vector will be reflected in the NOE rate. Recently, the cross-relaxation rates between the backbone amide protons of the protein ubiquitin were used to determine motional amplitudes [64, 65]. However, this study is limited by the small number of possible NOE transfers between the amide protons. Therefore the work in chapter 4 aims for the determination of cross-relaxation rates for the fully protonated protein to gain more long range motional information.

In the second part of this study, bicelles as a tool for the structure determination process of membrane proteins in solution NMR spectroscopy were investigated. Although 20-30 % of all proteins encoded in a typical genome are transmembrane proteins [66] and their essential role in many cellular processes as molecular recognition or transmembrane transports, compared to soluble proteins the structures of only very few transmembrane protein are solved. The basic problem for the structure determination of transmembrane proteins by solution state NMR spectroscopy is their need for an hydrophobic environment as an substitute for the natural lipid membrane. Since the relaxation increases with larger protein complexes, mostly amphiphilic detergents were used which form a micelle around the



hydrophobic regions of the protein and therefore increase the size of the complex only moderately [67, 68, 69, 70, 71]. Nevertheless, the differences between the micellar environment and the physiological lipid bilayer are severe, taking into account the strong curvature of the micelles surfaces and the different lateral pressure on the protein-detergent interface [72, 73]. The inadequacy of micelles to mimic physiological membranes is substantiated by the finding that some proteins lose their activity in a micelle [74, 75]. These problems could be solved by the use of bicelles which are hybrids of a liposome and a micelle and mimic more faithfully the hydrophobic environment for membrane proteins. Bicelles are consisting of a lipid bilayer surrounded at the edges by detergent micelle forming molecules [76, 77, 78]. While until now bicelles as a potential hydrophobic environment were studied with macromolecular peptides [79, 80, 81], in the work of chapter 5 the integral outer membrane protein OmpX was investigated in bicelles [82]. At first the composition of the bicelle was studied, next possible structural differences of OmpX in bicelles and micelles, followed by an investigation of the interface between the protein and the lipid-detergent complex.



## Chapter 2

# Evaluation of the SCRUM Method

### 2.1 Introduction

NMR spectroscopy is a very powerful tool for the investigation of the dynamical behavior of biological macromolecules [1]. Several NMR experiments have been established to measure motional amplitudes at atomic resolution. Each of these experiments can detect motion in a different time window. It is possible to detect motion faster than the total overall correlation time of the molecule (in general a few ns for proteins which depends linearly on the molecular weight) with  $R_1$ ,  $R_2$  and heteronuclear NOE measurements [2, 3, 4]. Motion in the time window between  $\mu\text{s}$  and ms can be detected by relaxation dispersion experiments [14, 15, 16]. It has been shown that on this time scale the opening and closing of hydrogen bridges and enzymatic reactions occur [17, 18]. Even slower motion than ms can be measured with exchange and real time experiments. But until a few years ago it was not possible to detect dynamics in the time window between ns to  $\mu\text{s}$  with liquid state NMR methods. This changed with the use of residual dipolar couplings (RDCs) as an indicator of protein dynamics. The RDCs are interactions between nuclei which became observable if the rotation of the protein gets restricted by measuring it in an anisotropic medium. The size of the RDC depends on the angle of the internuclear vector in the preferred protein orientation to the static magnetic field. Therefore changes of this angle by motion of the vector will influence the size of the averaged RDC. In this way RDCs are able to detect all motion faster than ms and can cover the earlier mentioned undetectable time window.

Such ns to ms motion became even more interesting when recently ensembles were created, which were restrained against RDCs and therefore could reflect the motion up to ms [37, 42]. These ensembles covered for the first time the full conformational space which ubiquitin adopts in complex with its binding partner. Since the ensembles base on experimental values from ubiquitin in solution without any complex partner, this indicates that free ubiquitin can already adopt all conformations necessary for their binding complexes (the concept of the conformational selection) and does not depend on conformational changes

induced by the binding partner (the concept of the induced fit). In contrast, earlier ensembles based on relaxation data [83, 84] covering only motion up to ns could not cover all binding conformers. Therefore the ns to  $\mu$ s motion seems to be very important for the interaction between proteins.

In order to convert RDCs into motional insight, several approaches were developed in the last years [85, 86, 87, 88]. One of them is the model-free approach developed in the groups of Prof. Griesinger and Prof. Brüschweiler [46, 47, 48]. A basic problem of the model-free approach is its dependency on a known protein structure. Structural noise will therefore affect the results of the calculations. To solve this problem the self-consistent RDC-based model free (SCRM) approach [49] was developed. It is an improved version of the model-free approach, which conducts an iterative procedure to use the calculated data not only for the identification of the protein dynamics, but also for the determination of the average structural orientation of the atom pair from which the RDCs originate. In this way errors in the used protein structure will be reduced in each iterative step until the internuclear vector orientations converge.

In a former work by Walter (diploma thesis [89]) the alleviation of structural noise from the used protein structure by the SCRM approach has been shown for a set of nine different structures of ubiquitin in different complexes. But the differences between these nine structures were relatively small. Therefore, in this work two scenarios were studied in which protein structures with stronger deviations to the known ubiquitin structures were used as starting structures for the SCRM approach.

As test subject the protein ubiquitin was used. This protein is easy to express, does not aggregate in concentrations of up to 5 mM and is quite small (around 8 kD) while having many relevant secondary structure elements. In addition, extensive investigations about the structural and dynamical properties of ubiquitin have already been conducted. Therefore, many structural ensembles and single structures for free ubiquitin and ubiquitin with one of its many binding partners are available for validation. Mainly the RDCs of the amide N-H groups in the protein backbone were measured and used for the SCRM approach.

## 2.2 Theory

The following short summary of the theoretical background of the RDC-based model-free approach is adapted from Lakomek et al. [49]:

The observable residual dipolar coupling depends on the strength and rhombicity of the alignment of the anisotropic medium in which the protein is solved as well as on the dynamically averaged internuclear vector relative to the static magnetic field of the spectrometer. In the alignment frame, unique for each anisotropic medium, the dipolar coupling is given by

$$\langle S^{exp} \rangle = \sqrt{\frac{4 \cdot \pi}{5}} D_{zz} \{ \langle Y_{2,0}(\theta, \phi) \rangle + \sqrt{\frac{3 \cdot \pi}{8}} R (\langle Y_{2,2}(\theta, \phi) \rangle \langle Y_{2,2}(\theta, \phi) \rangle) \} \quad (2.1)$$

with  $D_{zz}$  as the primary component of the alignment tensor,  $R$  as the rhombicity and  $\theta$  and  $\phi$  as the spherical coordinates of the internuclear vector. The brackets  $\langle \rangle$  denotes dynamical averaging. For the application of the SCRM approach a rotation from the individual alignment frames to an arbitrary, but common frame has to be conducted. Commonly the molecular frame is used for this reason. After applying a Wigner rotation around the angles  $\alpha$ ,  $\beta$  and  $\gamma$  the dipolar coupling is given by

$$S^{exp} \cdot D_{i,zz} = \sum_{M=-2}^2 F_{i,M} \langle Y_{2,M}(\theta_j^{mol}, \phi_j^{mol}) \rangle \quad (2.2)$$

with

$$F_{i,M} = \sqrt{\frac{4 \cdot \pi}{5}} (e^{-1M\alpha^i} d_{M0}^2(\beta^i) + \sqrt{\frac{3}{8}} R (e^{-1M\alpha^i} d_{M2}^2(\beta^i) e^{-12\gamma^i} + e^{-1M\alpha^i} d_{M-2}^2(\beta^i) e^{12\gamma^i})). \quad (2.3)$$

If the RDC data sets sufficiently cover the five-dimensional space of the alignment tensor, the inversion of the F-matrix in equation 2.2 yields the dynamical averaged spherical harmonics. As a description of the motional amplitudes, RDC-based order parameter are determined by

$$S_{RDC}^2 = \frac{4 \cdot \pi}{5} \sum_{M=-2}^2 \langle Y_{2,M}(\theta, \phi) \rangle_{ps}^{ms} \langle Y_{2,M}^*(\theta, \phi) \rangle_{ps}^{ms} \quad (2.4)$$

The order parameter are in range between 1 and 0, with 1 representing a completely fixed internuclear vector and 0 representing a totally delocalized internuclear vector.

In addition to the RDC-based order parameter also the dynamical averaged orientations of the internuclear vector can be determined by the SCRM approach. This is achieved by

another Wigner rotation around the angle  $(\theta_{av}, \phi_{av}, 0)$  maximizing

$$\max \langle Y_{2,0}(\theta', \phi') \rangle = \sqrt{\frac{4 \cdot \pi}{5}} \sum_{M=-2}^2 Y_{2,M}^*(\theta_{av}, \phi_{av}) \langle Y_{2,M}(\theta, \phi) \rangle \quad (2.5)$$

The angle  $\theta_{av}$  and  $\phi_{av}$  correspond to the dynamic averaged orientation of the internuclear vector in the molecular frame.

For the comparison of the SCRM results of the structures with artificial noise to the artificial noise free structures the Q values were determined by

$$Q = \sqrt{\frac{\sum S_{noise}^{RDC} - S_{noisefree}^{RDC}}{\sum S_{noisefree}^{RDC}}} \quad (2.6)$$

## 2.3 Material and Methods

### The SCRM Approach

The model-free approach for the determination of dynamics from RDCs was developed in the group of Prof. Griesinger in 2001 [46]. The general idea of the approach is that many RDCs of a protein are measured from various anisotropic media. The details of the approach are shown in Peti et al. [46], Meiler et al. [47] and Lakomek et al. [48]. The so called alignment tensor describes the direction and strength of the preferred orientation of the protein in the medium. It is calculated on base with the experimentally measured RDCs and a known structure of the protein. This tensor translates the orientation and dynamic properties of the observed atom pair described as spherical harmonics into the measurable residual dipolar coupling (equation 2.2). If RDC data from anisotropic media with five linear independent alignment tensors can be measured, the spherical harmonics of the correspondent internuclear vectors can be directly calculated. Since it is not possible to construct anisotropic media in a way that the alignment tensors are completely linearly independent, RDC data sets from more than five media have to be used to achieve a sufficiently good coverage of the five dimensional space. After solving the spherical harmonics not only order parameters can be calculated to describe the dynamical amplitudes according to equation 2.4, but also the dynamical averaged orientation of the internuclear vector according to equation 2.5.

It was shown that structural noise on the single protein structure used for the determination of the alignment tensors can contribute a strong systematic error to the results of the model-free approach [50, 51, 52, 53]. The SCRM approach is an iterative procedure (the SCRM

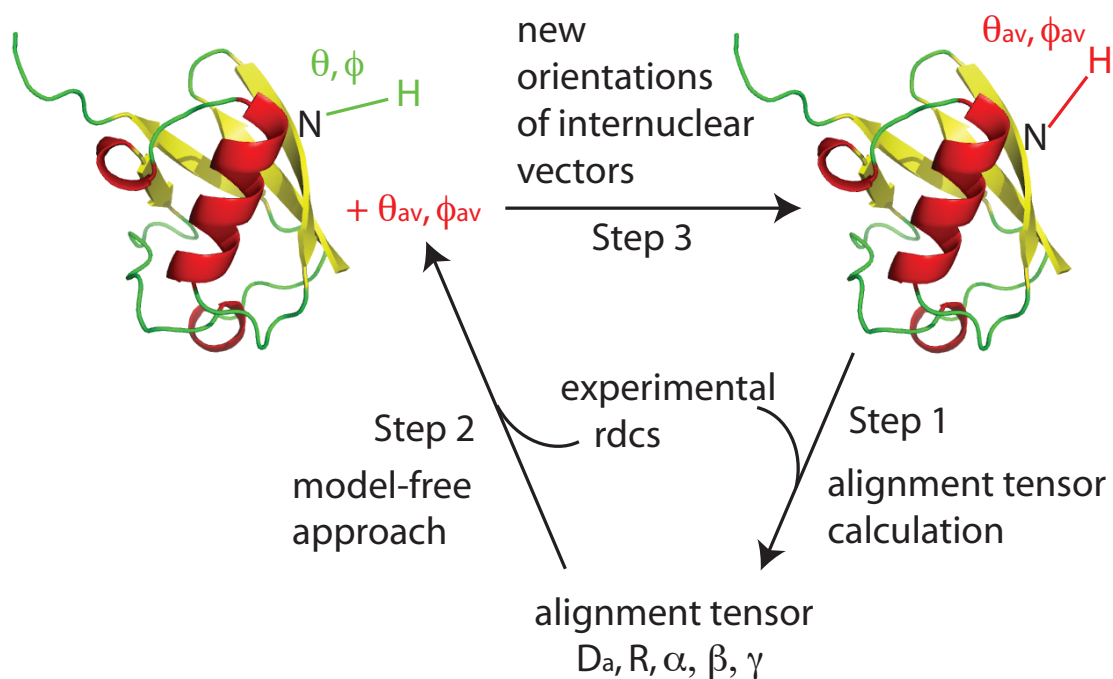


**Figure 2.1:** A graphical description of the SCRM cycles: In step 1 based on a protein structure and the experimental RDCs the alignment tensors are calculated. In step two these alignment tensors together with the RDCs are used for the model-free approach to determine the angles of the dynamically averaged internuclear vectors. In step three these angles are used to optimize the orientation of the internuclear vectors in the structure to reduce structural noise.

cycle is shown in figure 2.1) to reduce this influence of structural noise on the model-free approach. Therefore in a first cycle the noisy structure is used to determine a rough alignment tensor per alignment medium. With these tensors the model-free approach is used to calculate the order parameter and average internuclear vectors. These internuclear vectors are afterwards introduced into the protein structure, which is then used in a second cycle to calculate more accurate alignment tensors. These tensors are the base for another run of the model-free approach which delivers more accurate order parameters and internuclear vectors. These cycles are repeated until the values converge.

## The Residual Dipolar Couplings and Corresponding Alignment Media

A selection of 36 data sets (further on named D36M) [49] was used for the SCRM approach analysis [49].

Wild-type  $^{15}\text{N}$ ,  $^{13}\text{C}$ -labeled human ubiquitin was expressed according to a previous protocol by Johnson et al. [90].

For the first 13 alignment media 2.5 mg ubiquitin per sample were dispersed in a phosphate buffer (50 mM  $\text{NaPO}_4$ , 100 mM NaCl, pH = 6.5, 0.1 % (w/v)  $\text{NaN}_3$ , 10 % (v/v)  $\text{D}_2\text{O}$ ), if not else mentioned. The final ubiquitin concentration varied between 0.75 and 0.90 mM.

A1: A 7% positively charged gel sample was prepared according to Cierpicki and Bushweller [91]. The positive charge resulted from an addition of (3-acrylamidopropyl)-trimethylammonium chloride (APT-MAC) in a ratio to the acrylamide of 1:3.

A2: A 7% positively charged gel sample was prepared as A1, but with a APT-AMP : acrylamide ratio of 1:1.

A3: A 5% negatively charged gel according the same protocol as A1. The negative charge result from an addition of acrylic acid (Sigma-Aldrich, Inc.) in a ratio of acrylic acid: acrylamide of 1:1.

A4: The ubiquitin solution was mixed in a ratio of 2:1 with a dodecyl-penta(ethylene glycol) (C12E5) stock solution (15% w/v). The resulting solution became opalescent after addition of 1.5% (v/v) hexanol according to Ruckert und Otting [32].

A5: The ubiquitin was mixed into a suspension of 25 mg/mL Pf-1 phage (ASLA Ltd., Riga, Latvia) in 50 mM Na phosphate buffer with 100 mM NaCl, according to Zweckstetter and Bax [35].

A6: A Pf-1 phage sample was prepared as described for A5, but with a Pf-1 phage concentration of 20 mg/mL.

A7: A bicelle medium was created according to Triba et al. [31] by mixing 1,2-dimyristoyl-sn-glycero-3-phosphatidylcholine (DMPC) with 1,2-dihexanoyl-sn-glycero-3-phosphatidylcholine (DHPC) (Avanti Polar Lipids, Alabama) in a ratio of 3:1 with a total concentration of 15% (w/v) in a Na phosphate buffer at pH=6.5 containing 50 mM NaCl, 0.1% sodium azide and 10%  $\text{D}_2\text{O}$ . The total ubiquitin concentration was 0.9 mM.

A8: A bicelle medium was created from a mixture of 1,2-dimyristoyl-sn-glycero-3-phosphatidylcholine (DMPC), 1,2-dihexanoyl-sn-glycero-3-phosphatidylcholine (DHPC) and sodium dodecyl sulfate (SDS) (Serva, Heidelberg, Germany) in a ratio of 30:10:2 with a total concentration of 5% (w/v) in a Na phosphate buffer at pH=6.5 containing 15%  $\text{D}_2\text{O}$  by several cycles of cooling it in a ice bath, vortexing and heating similar to Triba et al. (2005) [31]. The total ubiquitin concentration was 0.75 mM.

A9: A bicelle medium was prepared as A8, with 1,2-dilauroyl-sn-glycero-3-phosphatidylcholine (DLPC) instead of DMPC and a total lipid concentration of 10% (w/v).

A10: A bicelle medium was prepared as A8, with tetradecylphosphocholine (C14PC) in-



stead of SDS and a lipid/detergent mixing ratio of 30:10:1.

A11: A bicelle medium was prepared as A8, with tetradecylphosphocholine (C14PC) instead of SDS and a total lipid concentration of 10% (w/v).

A12: A bicelle medium was prepared as A8, from a mixture of 1,2-dimyristoyl-sn-glycero-3-phosphatidylcholine (DMPC), 3([3-Cholamidopropyl]dimethylammonio)-2-hydroxy-1-propan-sulfonat (CHAPSO) and cetyltrimethylammoniumbromid (CTAB) in a ratio of 50:10:1 and a total lipid concentration of 10% (w/v) according to [92] .

A13: A bicelle medium was prepared as A8, with cetyltrimethylammoniumbromid (CTAB) instead of SDS, a lipid/detergent mixing ratio of 30:10:1 and a total lipid concentration of 8% (w/v).

All samples of the media A14-A18 contain 0.4-0.6 mM of ubiquitin in a buffer of 10mM  $NaPO_4$ , pH = 6.5, 0.1 % (w/v) and 10 % (v/v) D2O).

A14: A bicelle medium prepared according to Cornilescu et al. [93] with 1,2-dimyristoyl-sn-glycero-3-phosphatidylcholine (DMPC) with 1,2-dihexanoyl-sn-glycero-3-phosphatidylcholine (DHPC) (Avanti Polar Lipids, Alabama) in a ratio of 3:1 (5% w/v).

A15: A bicelle medium prepared according to Sanders and Prestegard [92](1998 ref) with 3([3-Cholamidopropyl]dimethylammonio)-2-hydroxy-1-propansulfonat (CHAPSO), 1,2-dilauroyl-sn-glycero-3-phosphatidylcholine (DLPC) and sodium dodecyl sulfate (SDS) in a ratio of 125:25:1 (5% w/v).

A16: A mixture of dodecyl-penta(ethylene glycol) (C12E5) and hexanol according to Ruckert und Otting [32] with a C12E5 surfactant-to-water ratio was 5 % (w/w) and the molar ratio of surfactant/alcohol was 0.985.

A17: Purple membrane fragments at 4 mg/mL and 100 mM NaCl according to Koenig et al. [33] were added to the ubiquitin solution.

A18: The ubiquitin was mixed into a suspension of 17 mg/mL Pf-1 phage (ASLA Ltd., Riga, Latvia) in 10 mM Na phosphate buffer with 350 mM NaCl, according to Zweckstetter and Bax [35].

All samples of the media A19-A23 contain 0.6-1.1 mM of ubiquitin in a buffer of 50mM  $NaPO_4$ , pH = 6.5, 0.1 % (w/v) and 10-15 % (v/v) D2O).

A19: A 7% uncharged gel sample was prepared according to Sass et al. [36].

A20: A sample was prepared according to Barrientos et al. [34] as a 3.5 % (w/v) solution of cetylpyridinium bromide and *n*-hexanol at a molar ratio of CPBr and *n*-hexanol of 1:1 with 25 mM NaBr. A21: A mixture of dodecyl-penta(ethylene glycol) (C12E5) and hexanol according to Ruckert und Otting [32] with a C12E5 surfactant-to-water ratio was 5 % (w/w) and the molar ratio of surfactant/alcohol was 0.985.

A22: Purple membrane fragments at 4 mg/mL and 50 mM NaCl according to Koenig et al. [33] were added to the ubiquitin solution.

A23: The ubiquitin was mixed into a suspension of 15 mg/mL Pf-1 phage (ASLA Ltd.,

Riga, Lativa) in 10 mM Na phosphate buffer with 400 mM NaCl, according to Zweckstetter and Bax [35].

As data set A19 - A36 NH RDCs data sets published by Ottiger et al. [94] (A19 and A20), by Briggman and Tolman [95] (A21 - A29) and by Ruan and Tolman [96] (A30 - A36) has been used.

## 2.4 Results and Discussion

To investigate the ability of the SCRM approach to alleviate structural noise from a starting structure two test cases of artificial structural noise were set up. For the first case random noise were added on the orientation of the NH vectors for the structure of ubiquitin. For the second case ubiquitin structures were generated by the program ROSETTA just on the base of the protein sequence.

### 2.4.1 Synthetic Structural Noise

Starting from the x-ray structure by Ramage et al. (pdb code: 1ubi) [97] with hydrogens added under standard geometry synthetic gaussian noise was added on the orientation of the NH backbone vector orientations. This was done using the program PALES [100] for all NH backbone vectors with an opening angle  $\theta$  and a polar angle  $\phi$  of a)  $10^\circ$  b)  $20^\circ$  and c)  $30^\circ$  as described by Zweckstetter and Bax [50]. For each of the cases a), b) and c) three structures with random noise were created. These noisy structures were kindly provided by Dr. Nils-Alexander Lakomek.

Each of the nine structures with artificial noise were used as a starting structure for the SCRM approach. The order parameters were calculated with the SCRM approach for these nine starting structures without any SCRM cycles and after four improvement cycles (shown in figure 2.2 graph A and B). The Q values calculated by equation 2.6 of the order parameters compared to the original x-ray structure are shown in table 2.1. Without SCRM cycles the model-free approach delivers order parameter which are strongly deviating from the reference ones of the artificial noise free original structure. Even the small angle changes of the three  $10^\circ$  angle structures lead to significant errors on the order parameter determination (an average Q-value of 0.18), what increases with the  $20^\circ$  and  $30^\circ$  structures even stronger (average Q-values of 0.30 and 0.70, respectively). After just four cycles of the SCRM approach these deviations are alleviated almost completely for all structures beside structure 1 of the  $30^\circ$  set (Q-values  $\leq 0.05$ ). For this structure the error due to the structural noise is still relatively high after the application of the SCRM iteration, nevertheless the deviation

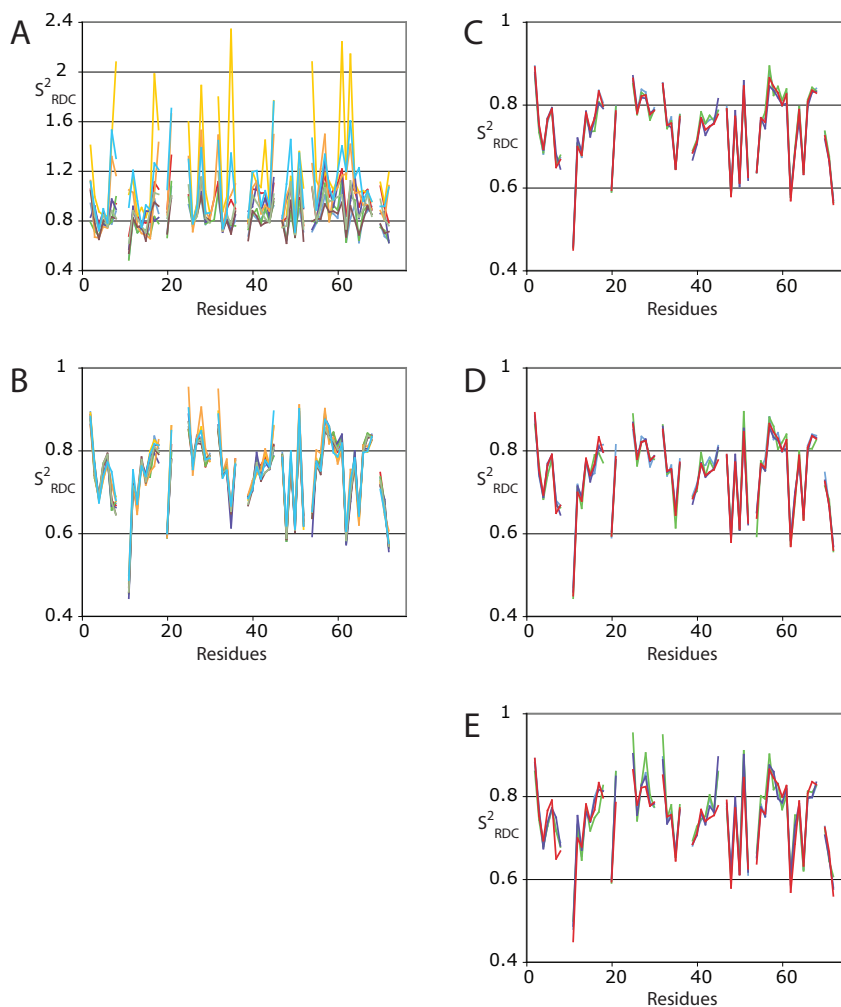


**Figure 2.2:** The graphs show the order parameter per residue calculated by the SCRM method with different protein structures. Graph A shows the order parameters calculated from all nine noisy structures before the structural improvement by the SCRM cycles, while in graph B the order parameters are shown after four iterative SCRM cycles. Graph C shows the order parameters after the four SCRM cycles from the starting structures with  $10^\circ$  deviation, graph D for the structures with  $20^\circ$  deviation and graph E for the structures with  $30^\circ$  deviation. The red graph represents the order parameters of the x-ray structure (pdb code: 1ubi) as a reference.

for this structure was already much stronger from the start (Q-value 0.93 compared to an total average Q-value of 0.45) than for the other structures.

**Table 2.1:** Q-values of the order parameters determined without and after four SCRM cycles for the nine noisy structures relative to the original structure

Starting structure	Q(without SCRM cycles)	Q (after four SCRM cycles)
10° Structure 1	0.13	0.01
10° Structure 2	0.22	0.02
10° Structure 3	0.20	0.02
10° Structure average	0.18	0.02
20° Structure 1	0.35	0.02
20° Structure 2	0.29	0.02
20° Structure 3	0.24	0.02
20° Structure average	0.30	0.02
30° Structure 1	0.93	0.14
30° Structure 2	0.51	0.05
30° Structure 3	0.57	0.04
30° Structure average	0.70	0.09
All nine structures	0.45	0.05

#### 2.4.2 Rosetta created Structures

For the second scenario ubiquitin structures were generated by the program ROSETTA [98, 99] just on the base of the protein sequence. Six structures with rmsds to the x-ray structure of around 3 Å were used as starting structures for the SCRM approach.

The ROSETTA structures were kindly provided by Prof. Jens Meiler.

With each of these six ROSETTA structures and the D36M RDC data sets the SCRM approach was conducted. The order parameters were determined by the model-free approach before the use of the SCRM cycles and after the application of eleven SCRM cycles (shown in figure 2.3). The Q-values calculated by equation 2.6 of the order parameters compared to the order parameters of the ubiquitin x-ray structure are shown in table 2.2.

The Q values from the calculations without the application of the SCRM cycles show that the structural deviations to the x-ray structure are larger than in the first scenario. The average Q value on base with the starting ROSETTA structures is 1.20 as compared to an average Q value of 0.45 for the nine structures in the first scenario. Therefore, it was necessary to extend the number of SCRM cycles. Eleven cycles were conducted and the Q values calculated. For five of the six structures the Q value drops to 0.14 or 0.15. This is a large improvement compared with the results of the model-free approach without the SCRM, but still significantly higher than for the first scenario with an average Q value of

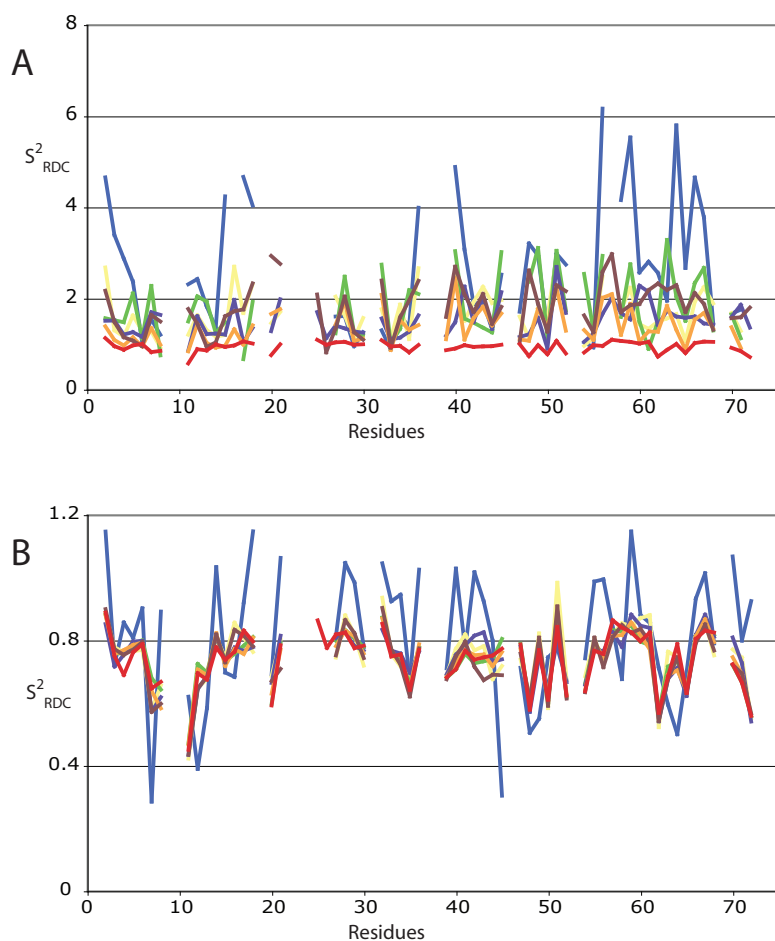


**Figure 2.3:** The graphs show the order parameters per residue calculated by the SCRM method using the six ROSETTA structures. The red graph represent the order parameter of the x-ray structure (pdb code: 1ubi) as a reference. The dark blue graph represents the order parameters from the ROSETTA structure 1, which has a exceptionally high deviation with respect to the x-ray structure.

0.05. This shows that it is not possible to completely compensate the larger structural noise. The order parameters do not fully converge to the values found when the initial structures are closer to the average structure, but reduce the influence of the structural noise to a level where reasonable information can be extracted from the order parameters.

**Table 2.2:** Q-values of the order parameters determined without and after eleven SCRM cycles for the six ROSETTA generated structures relative to the original structure

Starting structure	Q(without SCRM cycles)	Q (after eleven SCRM cycles)
Structure 1	2.09	0.29
Structure 2	0.89	0.15
Structure 3	1.12	0.14
Structure 4	0.70	0.14
Structure 5	0.58	0.14
Structure 6	1.06	0.14
All six structures	1.20	0.18

Only the order parameters for structure 1 of the ROSETTA structure set show an exceptional behavior (shown as the dark blue graph in figure 2.3). The Q values of its order parameters start with 2.09 relative to the x-ray structure and decrease only to 0.29. In figure 2.4 the convergence of the order parameters over the eleven SCRM cycles is shown. It is obvious that the order parameters based on the ROSETTA structures 2 - 5 converge already after 5 or 6 cycles, while for structure 1 the order parameter continue to vary strongly for many residues even after eleven cycles. An additional extension to more SCRM cycles does not seem reasonable, since the Q values no longer systematically decrease.

The protein ubiquitin is of course a special case for the program ROSETTA. Ubiquitin is so well investigated that several structures of it in free form or in complex with several binding partners are deposited in the protein data bank. Since ROSETTA works based on homology data from such databanks, it will be able to find the right fold for a protein which is so well characterized. For a protein with a less well known structure or where less homologous structures exist the ROSETTA created structures would probably deviate much more from the average one. Therefore, the SCRM will probably fail to deliver precise order parameter based on ROSETTA generated starting structure for such proteins.

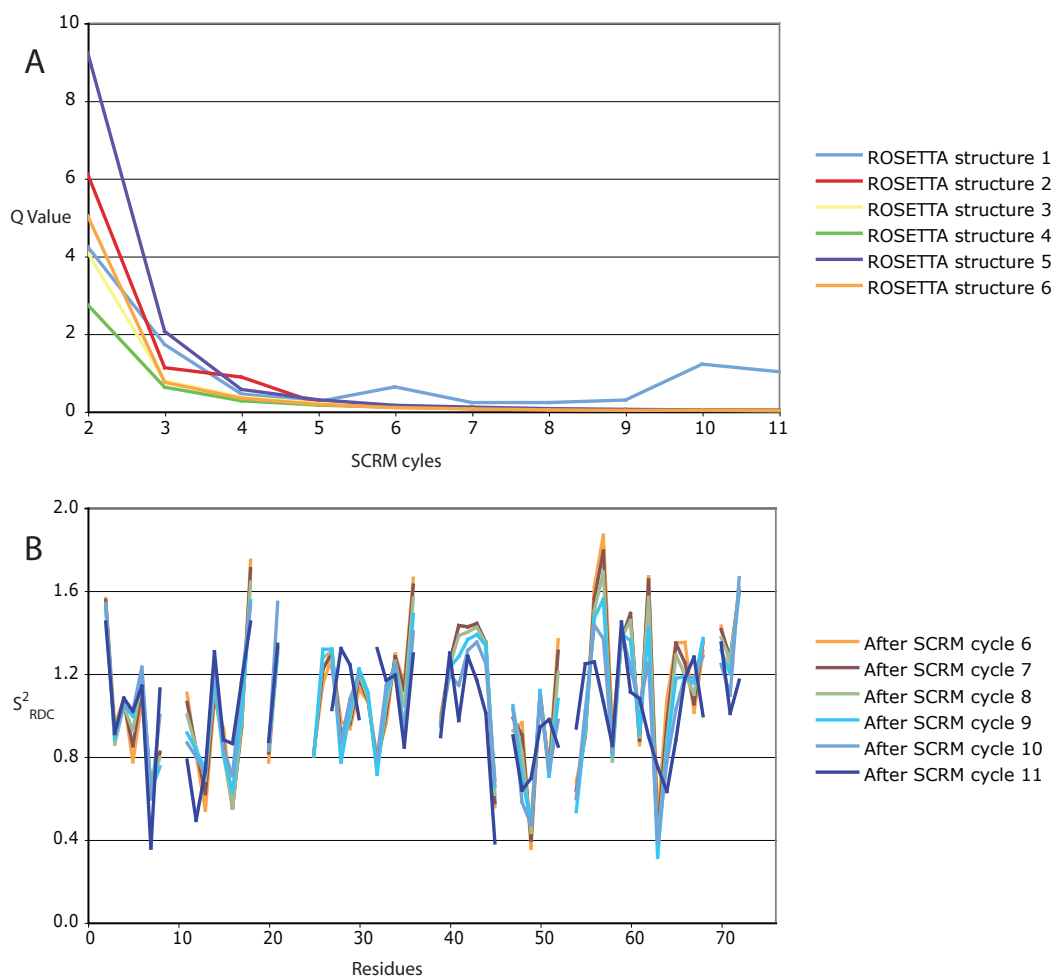


**Figure 2.4:** Graph A shows the changes of the order parameter after the SCRM cycles by a Q value (analog to equation 2.6 between the former and the new order parameters after the cycle). Graph B shows the order parameter per residue calculated by the SCRM method using the ROSETTA structure 1. Only the order parameters from the SCRM cycles five to eleven are shown. While for some residues the order parameters converge, for many other residues the order parameters vary over a broad range.

## 2.5 Summary and Outlook

Long time no NMR spectroscopical experiments were established to measure protein dynamic in the range between ns and  $\mu s$ . Only during the last years several methods were developed to determine on the basis of experimentally measured residual dipolar couplings protein dynamic in this time window. One of these methods is the model-free approach, which works without assumptions about the motional modes, but needs a known structure of the protein for the calculations. Therefore, the resulting order parameters are error-prone to structural noise of the used protein structure. The SCRM method was developed

as an improved version of the model-free approach to compensate for the structural noise by an iterative procedure and make the determination of the order parameters more reliable.

To test the ability of the SCRM approach to alleviate the influence of structural noise for the order parameter calculation two artificial test scenarios were investigated. In the first scenario the NH vectors of the protein x-ray structure were displaced by a gaussian noise of various standard deviation. In a second scenario it was tested if the SCRM approach needs a structure determined based on experimental structural data or if a structure generated with the program ROSETTA only on the basis of the protein sequence would be sufficient.

It could be shown that the SCRM approach is able to compensate strong structural errors. For the artificial displacement of the amide internuclear vectors by angles of up to  $30^\circ$  four cycles of the SCRM approach are able to alleviate the influence of the displacement for almost all cases. Also structures that are found with ROSETTA and exhibit larger differences to the average structure can in principle be used as starting structures for the SCRM approach. Starting from such structures it is still possible to calculate reliable order parameters. But for structures with even larger deviations the number of SCRM cycles have to be increased significantly. Nevertheless the SCRM approach failed to converge to remove the structural deviations from one of the ROSETTA generated structures. Therefore, the SCRM will probably fail to deliver precise order parameter based on ROSETTA generated starting structure for such proteins.



## Chapter 3

# Development of new NMR Experiments for the Measurement of Cross-Correlated Relaxation Rates

### 3.1 Introduction

The knowledge about the dynamics of a protein is important for the understanding of its functionality [1]. Several NMR spectroscopical experiments have been established to measure the amplitude of protein motion with an atomic resolution [2, 3, 4, 14, 15, 16, 85, 88, 49]. In combination with computational methods structure ensembles have been created, which are able to model a protein's dynamical behavior [83, 84, 42, 37]. Aside, from the correct reproduction of the motional amplitudes these ensembles have shown strong correlated motion in the protein. For example, the EROS ensemble [37] predicts a correlated pincer motion between one end of the  $\alpha$ -helix and a loop between two  $\beta$ -strands. One possibility for the detection of correlated motion is the use of cross-correlated relaxation (CCR) rates as an indicator [57, 58, 59, 60], because the size of a cross-correlated relaxation rate depends on the angle between two relaxation processes [54]. For dipole - dipole relaxation of two nuclei, the direction of such a process points along the internuclear vector. Therefore, the CCR rate depends on the angle between two internuclear vectors. Depending on the relative motion of the internuclear vectors the intervectorial angle is changing and therefore the averaged CCR rate can reflect this relative motion.

For this study, several experiments were developed to measure the CCR rates between atom pairs at specific sites of the protein. The most critical point for the development of such NMR pulse sequences is the build-up of the coherence between the two atom pairs. The

build-up of the coherence is achieved by a magnetization transfer either via a coupling, scalar or dipolar, or via a relaxation process, cross relaxation or cross-correlated relaxation, between the atoms. Since in all such experiments the coherence between the atom pairs has to be refocused on one of the pairs after the evolution of the CCR rates, always two transfer steps per experiment are needed. For an efficient transfer process, as an one-bond coupling, the build-up and the refocusing of the major part of the magnetization takes each only a few milliseconds. But for all transfers between atom pairs which are close in space, but without a significant electron density between them (e.g. in different strands in a  $\beta$ -sheet) the transfer process is much less efficient. For such processes it is already a challenge to accomplish transfer efficiencies of a few percent and therefore the sensitivities of the detected signals are limiting the success of these experiments. But especially such global dynamic modes of proteins would be very important for the understanding of their functionality and therefore the development of methods to measure such long range CCR rates are of special interest [103].

Experiments for three special sites of the protein (shown in figure 3.1) were investigated, the backbone, the  $\beta$ -sheet and the hydrophobic core. Experiments with four different transfer processes, scalar and dipolar coupling, cross and cross-correlated relaxation, were applied:

- The CCR rates of the NH -  $C\alpha H\alpha$  intraresidual pairs in the protein backbone using scalar couplings for the transfer
- The CCR rates of the NH - NH pairs in separated strands in the  $\beta$ -sheet using residual dipolar couplings for the transfer
- The CCR rates of the  $C\alpha H\alpha$  -  $C\alpha H\alpha$  pairs in separated strands in the  $\beta$ -sheet using cross-correlated relaxation for the transfer
- The CCR rates of the methyl CH pairs in the hydrophobic core using cross relaxation and cross-correlated relaxation for the transfer

As in chapter 2 the test object was the protein ubiquitin. This work was partially published in Fenwick et al. [42].

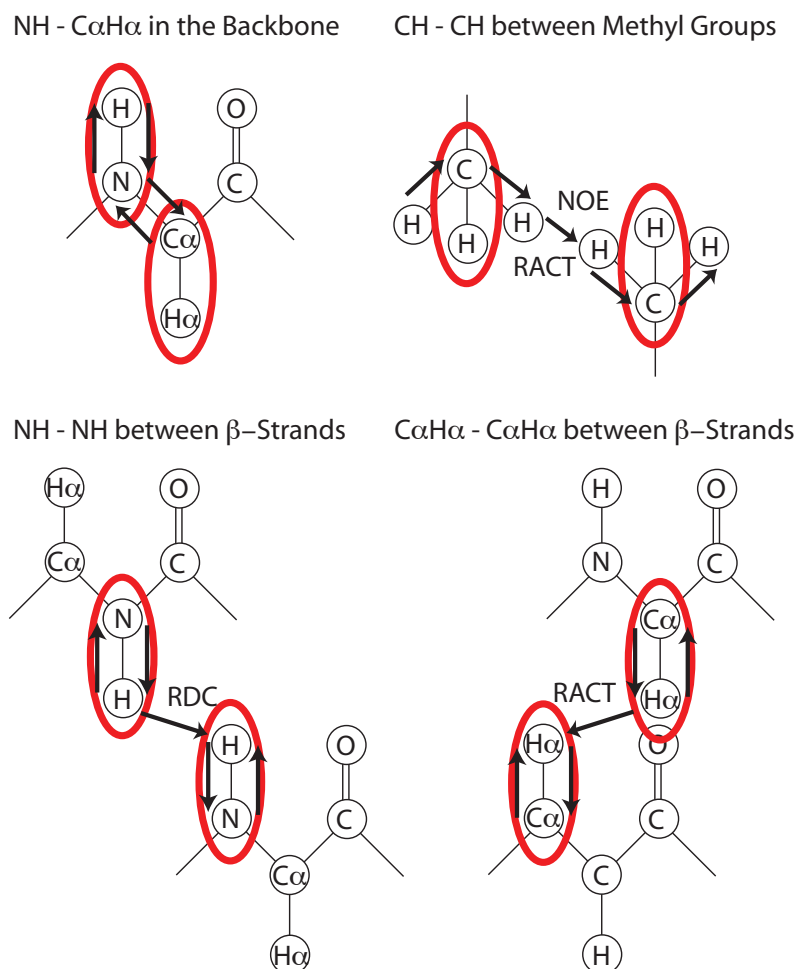


**Figure 3.1:** Schemes of the atom pairs between which the experiments measure cross correlated relaxation rates. The red ellipses highlight the atom pairs involved in the measured CCR process, while the arrows indicate the magnetization transfer path ways.

## 3.2 Theory

The following short summary of the cross-correlated relaxation theory is adapted from the papers of Reif et al. [54] and Voegeli and Yao [61]:

### The Cross-Correlated Relaxation Rate

In a system of two pairs of nuclei ( $A^1 - A^2$  and  $B^1 - B^2$ ) the double- and zero-quantum cross correlated relaxation rate  $\Delta_{A1A2,B1B2}$  can be measured under the requirements that

- the desired double- and zero-quantum coherence between  $A^1$  and  $B^1$  can be excited,
- there are sufficiently large J couplings between  $A^1$  and  $A^2$  on the one side and  $B^1$  and  $B^2$  on the other side and

c) the dipole-dipole interactions between  $A^1$  and  $A^2$  as well as  $B^1$  and  $B^2$ , respectively, are the dominating relaxation sources for single-quantum coherence on  $A^1$  and  $B^1$ , respectively. The dipole tensor between each of the two spin pairs is axially symmetric with the symmetry axis collinear to the internuclear vector.

In this summary four different kinds of relaxation are mentioned:

Eigen-relaxation is a relaxation process which is caused by a non-equilibrium magnetization state of a nuclear spin and affects the magnetization of the same spin. In contrast, a cross-relaxation process originated by a non-equilibrium spin is affecting the magnetization of a second spin. Autocorrelated relaxation and cross-correlated relaxation occur if two relaxation processes affect the non-equilibrium spin (or spins in the case of double- and zero-quantum coherence). The autocorrelated relaxation rates cover the contributions without any interference between the two relaxation processes, while the cross-correlated relaxation rates cover the contributions with interference of the two relaxation processes.

The easiest way to measure cross-correlated relaxation rates is by transverse double- and zero-quantum coherence, because in this case the spectral density  $j(\omega_q)$  is dominated by  $j(0)$ .

The time-dependent density matrix for the double- and zero-quantum coherence has the general form

$$(\hat{\sigma}_{\mu,\mu'}^{DQ/ZQ})^\bullet = [-\hat{\Gamma}^{DQ/ZQ} - i \cdot \hat{\hat{\Omega}}^{DQ/ZQ}] (\hat{\sigma}_{\mu,\mu'}^{DQ/ZQ}). \quad (3.1)$$

with

$$(\hat{\sigma}_{\mu,\mu'}^{DQ/ZQ})^\bullet = \begin{pmatrix} A^{1+} B^{1+} A^{1\mu} B^{2\mu} \\ A^{1-} B^{1+} A^{1\mu} B^{2\mu} \\ A^{1+} B^{1-} A^{1\mu} B^{2\mu} \\ A^{1-} B^{1-} A^{1\mu} B^{2\mu} \end{pmatrix} \quad (3.2)$$

The set of density matrices  $(\hat{\sigma}_{\mu,\mu'}^{DQ/ZQ})$  describes the double- and zero-coherences  $A^{1+} B^{1+} A^{1\mu} B^{2\mu}$ ,  $A^{1-} B^{1+} A^{1\mu} B^{2\mu}$ ,  $A^{1+} B^{1-} A^{1\mu} B^{2\mu}$  and  $A^{1-} B^{1-} A^{1\mu} B^{2\mu}$  with  $\mu$  and  $\mu'$  varying between  $\alpha$  and  $\beta$ . In equation 3.1 the isotropic chemical shift  $\hat{\hat{\Omega}}^{DQ/ZQ}$  is

$$\hat{\hat{\Omega}}^{DQ/ZQ} = (\Omega_{A1} \pm \Omega_{B1}) + \pi \begin{pmatrix} \pm J_{A1A2} + J_{B1B2} & 0 & 0 & 0 \\ 0 & \mp J_{A1A2} + J_{B1B2} & 0 & 0 \\ 0 & 0 & \pm J_{A1A2} - J_{B1B2} & 0 \\ 0 & 0 & 0 & \mp J_{A1A2} - J_{B1B2} \end{pmatrix} \quad (3.3)$$

with the chemical shifts  $\Omega_{A1}$  and  $\Omega_{B1}$  and the scalar couplings of the two nuclei pairs  $^1J_{A1A2}$

and  ${}^1J_{B_1B_2}$ . The  $\pm$  in equation 3.3 represents a + in the case of double quantum coherence and a - in the case of zero-quantum coherence and inverse for  $\mp$ . The relaxation matrix  $\Gamma^{DQ/ZQ}$  is

$$\hat{\Gamma}^{DQ/ZQ} = \begin{pmatrix} \Gamma^a + \Gamma_1 + \Gamma_{\alpha\alpha}^{DQ/ZQ} & -\Gamma_{T_1}(A_2) & -\Gamma_{T_1}(B_2) & -W_2 \\ -\Gamma_{T_1}(A_2) & \Gamma^a + \Gamma_1 + \Gamma_{\alpha\beta}^{DQ/ZQ} & -W_0 & -\Gamma_{T_1}(B_2) \\ -\Gamma_{T_1}(B_2) & -W_0 & \Gamma^a + \Gamma_1 + \Gamma_{\beta\alpha}^{DQ/ZQ} & -\Gamma_{T_1}(A_2) \\ -W_2 & -\Gamma_{T_1}(B_2) & -\Gamma_{T_1}(A_2) & \Gamma^a + \Gamma_1 + \Gamma_{\beta\beta}^{DQ/ZQ} \end{pmatrix}. \quad (3.4)$$

Herein  $-\Gamma_{T_1}(A_2)$  and  $-\Gamma_{T_1}(B_2)$  are the  $T_1$  relaxation rates of the nuclei A2 and B2, respectively, which lead to population exchange between  $A_2^\alpha(B_2^\alpha)$  and  $A_2^\beta(B_2^\beta)$ , and  $\Gamma_1 = \Gamma_{T_1}(A_2) + \Gamma_{T_1}(B_2)$ .  $\Gamma^a$  covers the autocorrelated relaxation of A1 via A2 and B1 via B2 and external relaxation of A1 and B1-DQ/ZQ coherences.  $W_2$  and  $W_0$  are the rates for nonsecular exchange over double ( $A_2^\alpha B_2^\alpha \rightleftharpoons A_2^\beta B_2^\beta$ ) and zero quantum ( $A_2^\alpha B_2^\beta \rightleftharpoons A_2^\beta B_2^\alpha$ ) transitions due to NOE between A2 and B2.  $\Gamma_{\alpha\alpha}^{DQ/ZQ}$  denotes the different eigen-relaxation rates due to heteronuclear dipolar interactions, including the dipole-dipole cross-correlated relaxation rate  $\Gamma_{A_1A_2, B_1B_2}^c$ , the chemical shift anisotropy (csa) - dipole-dipole cross-relaxation rates  $\Gamma_{A_1, A_2}^c$ ,  $\Gamma_{B_1, A_2}^c$ ,  $\Gamma_{A_1, B_2}^c$  and  $\Gamma_{B_1, B_2}^c$ , and the secular part of double and zero quantum transitions due to NOE between A2 and B2.

In the following relaxation due to heteronuclear dipolar couplings will be concentrated on. The general relaxation superoperator applied to a density matrix  $\sigma$  has the form

$$\Gamma_{VW}\sigma = b_V \cdot b_W \cdot \sum_q [A_V^{(-q)}, [A_W^{(q)}, \sigma]] \cdot j_{VW}^q(\omega_q) \quad (3.5)$$

with V and W referring to an anisotropic interaction maintained by either of the two interacting nuclei pairs (A1 and A2 or B1 and B2),  $A_V^{(-q)}$ ,  $A_W^{(-q)}$  are the tensor operators of the dipolar coupling,  $j_{VW}^q(\omega_q)$  the corresponding spectral density and

$$b_V = -\frac{\mu_0 \cdot \gamma_k \cdot \gamma_l \cdot \hbar}{4 \cdot \pi \cdot r_{kl}^3} \quad (3.6)$$

with the indices k and l either being A1 and A2 or B1 and B2.

Therefore based on equation 3.5 the contributions to the double- and zero-coherence from autocorrelated relaxation ( $V = W =$  dipolar coupling between A1 and A2 or B1 and B2) is

$$\begin{aligned} [\hat{\Gamma}_{A1A2,A1A2}^a + \hat{\Gamma}_{B1B2,B1B2}^a] \sigma_{\mu,\mu'}^{DQ/ZQ} &= b_{A1A2}^2 \cdot \sum_{q=-2}^2 [A_{A1A2}^{(-q)}, [A_{A1A2}^{(q)}, \sigma_{\mu,\mu'}^{DQ/ZQ}]] \cdot j_{A1A2,A1A2}^q(\omega_q) \\ &+ b_{B1B2}^2 \cdot \sum_{q=-2}^2 [A_{B1B2}^{(-q)}, [A_{B1B2}^{(q)}, \sigma_{\mu,\mu'}^{DQ/ZQ}]] \cdot j_{B1B2,B1B2}^q(\omega_q) \end{aligned} \quad (3.7)$$

and the contribution from cross-correlated relaxation ( $V \neq W$ ) is

$$\begin{aligned} [\hat{\Gamma}_{A1A2,B1B2}^a + \hat{\Gamma}_{B1B2,A1A2}^a] \sigma_{\mu,\mu'}^{DQ/ZQ} &= b_{A1A2} \cdot b_{B1B2} \cdot \sum_{q=-2}^2 [A_{A1A2}^{(-q)}, [A_{B1B2}^{(q)}, \sigma_{\mu,\mu'}^{DQ/ZQ}]] \cdot j_{A1A2,B1B2}^q(\omega_q) \\ &+ b_{B1B2} \cdot b_{A1A2} \cdot \sum_{q=-2}^2 [A_{B1B2}^{(-q)}, [A_{A1A2}^{(q)}, \sigma_{\mu,\mu'}^{DQ/ZQ}]] \cdot j_{B1B2,A1A2}^q(\omega_q) \end{aligned} \quad (3.8)$$

These contributions can now be calculated by introducing the double- and zero-quantum coherences ( $A^{1+}B^{1+}A^{1\mu}B^{2\mu}$ ,  $A^{1-}B^{1+}A^{1\mu}B^{2\mu}$ ,  $A^{1+}B^{1-}A^{1\mu}B^{2\mu}$  and  $A^{1-}B^{1-}A^{1\mu}B^{2\mu}$ ) for  $\sigma_{\mu,\mu'}^{DQ/ZQ}$ . As an example here the calculation will be shown for  $A^{1+}B^{1+}A^{1\mu}B^{2\mu}$ , the other coherences behave accordingly.

As already mentioned, the spectral density function  $j^{(q)}(\omega_q)$  is dominated by the term  $j^{(q)}(0)$  for double- and zero-quantum coherences. Therefore the autocorrelated relaxation is given by

$$\begin{aligned} &[\hat{\Gamma}_{A1A2,A1A2}^a + \hat{\Gamma}_{B1B2,B1B2}^a] A^{1+}B^{1+}A^{2\mu}B^{2\mu} \\ &= b_{A1A2}^2 \cdot \sum_{q=-2}^2 [A_z^2 A_z^1, [A_z^2 A_z^1, A^{1+}B^{1+}A^{2\mu}B^{2\mu}]] \cdot j_{A1A2,A1A2}^q(0) \\ &+ b_{B1B2}^2 \cdot \sum_{q=-2}^2 [B_z^2 B_z^1, [B_z^2 B_z^1, A^{1+}B^{1+}A^{2\mu}B^{2\mu}]] \cdot j_{B1B2,B1B2}^q(0) \\ &= \frac{1}{4} [b_{A1A2}^2 \cdot j_{A1A2,A1A2}^q(0) + b_{B1B2}^2 \cdot j_{B1B2,B1B2}^q(0)] \cdot A^{1+}B^{1+}A^{2\mu}B^{2\mu} \\ &= [\Gamma_{A1A2,A1A2}^a + \Gamma_{B1B2,B1B2}^a] \cdot A^{1+}B^{1+}A^{2\mu}B^{2\mu} \end{aligned} \quad (3.9)$$

and the cross-correlated relaxation by

$$\begin{aligned}
& [\hat{\Gamma}_{A1A2,B1B2}^a + \hat{\Gamma}_{B1B2,A1A2}^a] A^{1+} B^{1+} A^{2\mu} B^{2\mu} \\
= & b_{A1A2} \cdot b_{B1B2} \cdot \left[ \sum_{q=-2}^2 [A_z^2 A_z^1, [B_z^2 B_z^1, A^{1+} B^{1+} A^{2\mu} B^{2\mu}]] \cdot j_{A1A2,B1B2}^q(0) \right. \\
& \left. + \sum_{q=-2}^2 [B_z^2 B_z^1, [A_z^2 A_z^1, A^{1+} B^{1+} A^{2\mu} B^{2\mu}]] \cdot j_{B1B2,A1A2}^q(0) \right] \quad (3.10) \\
= & \frac{1}{2} \cdot b_{A1A2}^2 \cdot b_{B1B2}^2 \cdot j_{A1A2,B1B2}^q(0) \cdot A^{1+} B^{1+} A^{2\mu} B^{2\mu} \\
= & \Gamma_{A1A2,B1B2}^a \cdot A^{1+} B^{1+} A^{2\mu} B^{2\mu}
\end{aligned}$$

By an analogous calculation for the operator  $A^{1-} B^{1+} A^{1\mu} B^{2\mu}$ ,  $A^{1+} B^{1-} A^{1\mu} B^{2\mu}$  and  $A^{1-} B^{1-} A^{1\mu} B^{2\mu}$ , the autocorrelated and cross-correlated relaxation rates for each peak of the quartet for the double- and zero-quantum magnetization can be determined. All together the  $\alpha\beta$  and  $\beta\alpha$  peaks are affected by a total relaxation rate of  $(\Gamma_{A1A2,A1A2}^a + \Gamma_{B1B2,B1B2}^a) + \Gamma_{A1A2,B1B2}^c$ , while the peaks of  $\alpha\alpha$  and  $\beta\beta$  are affected by  $(\Gamma_{A1A2,A1A2}^a + \Gamma_{B1B2,B1B2}^a) - \Gamma_{A1A2,B1B2}^c$ . This is reflected in different peak intensities for the inner and the outer peaks of the quartet.

In the case of isotropic reorientation for a spherical top molecule the dipole-dipole cross-correlated relaxation rate for each multiplet line of the quartet is given by

$$\Gamma_{A1A2,B1B2}^a = \frac{\gamma_{A1} \cdot \gamma_{A2}}{r_{A1A2}^3} \cdot \frac{\gamma_{A1} \cdot \gamma_{A2}}{r_{A1A2}^3} \cdot \left( \frac{\mu_0 \cdot \hbar}{4 \cdot \pi} \right)^2 \cdot \frac{1}{5} \cdot (3 \cos^2 \theta_{A1A2,B1B2} - 1) \cdot \tau_c, \quad (3.11)$$

where  $\theta$  is the projection angle between the A1A2 and the B1B2 internuclear vector and  $\tau_c$  is the overall rotational correlation time.

Analogous calculations are conducted for the cross correlated relaxation rate between the chemical shift anisotropy of A1 or B1 and the dipolar couplings between A1 and A2, or B1 and B2, respectively. The resulting total relaxation rates are for the double-quantum

spectrum

$$\begin{aligned}
\Gamma_{\alpha\alpha}^{DQ} &= +\Gamma^a + \Gamma_{A1A2,B1B2}^c + \Gamma_{A1,A1A2}^c + \Gamma_{B1,A1A2}^c + \Gamma_{A1,B1B2}^c + \Gamma_{B1,B1B2}^c + W_2 + \Gamma_1 \\
\Gamma_{\alpha\beta}^{DQ} &= +\Gamma^a - \Gamma_{A1A2,B1B2}^c - \Gamma_{A1,A1A2}^c - \Gamma_{B1,A1A2}^c + \Gamma_{A1,B1B2}^c + \Gamma_{B1,B1B2}^c + W_0 + \Gamma_1 \\
\Gamma_{\beta\alpha}^{DQ} &= +\Gamma^a - \Gamma_{A1A2,B1B2}^c + \Gamma_{A1,A1A2}^c + \Gamma_{B1,A1A2}^c - \Gamma_{A1,B1B2}^c - \Gamma_{B1,B1B2}^c + W_0 + \Gamma_1 \\
\Gamma_{\beta\beta}^{DQ} &= +\Gamma^a + \Gamma_{A1A2,B1B2}^c - \Gamma_{A1,A1A2}^c - \Gamma_{B1,A1A2}^c - \Gamma_{A1,B1B2}^c - \Gamma_{B1,B1B2}^c + W_2 + \Gamma_1
\end{aligned} \tag{3.12}$$

and for the zero-quantum spectrum

$$\begin{aligned}
\Gamma_{\alpha\alpha}^{ZQ} &= +\Gamma^a - \Gamma_{A1A2,B1B2}^c + \Gamma_{A1,A1A2}^c - \Gamma_{B1,A1A2}^c - \Gamma_{A1,B1B2}^c + \Gamma_{B1,B1B2}^c + W_0 + \Gamma_1 \\
\Gamma_{\alpha\beta}^{ZQ} &= +\Gamma^a + \Gamma_{A1A2,B1B2}^c - \Gamma_{A1,A1A2}^c + \Gamma_{B1,A1A2}^c - \Gamma_{A1,B1B2}^c + \Gamma_{B1,B1B2}^c + W_2 + \Gamma_1 \\
\Gamma_{\beta\alpha}^{ZQ} &= +\Gamma^a + \Gamma_{A1A2,B1B2}^c + \Gamma_{A1,A1A2}^c - \Gamma_{B1,A1A2}^c + \Gamma_{A1,B1B2}^c - \Gamma_{B1,B1B2}^c + W_2 + \Gamma_1 \\
\Gamma_{\beta\beta}^{ZQ} &= +\Gamma^a - \Gamma_{A1A2,B1B2}^c - \Gamma_{A1,A1A2}^c + \Gamma_{B1,A1A2}^c + \Gamma_{A1,B1B2}^c - \Gamma_{B1,B1B2}^c + W_0 + \Gamma_1
\end{aligned} \tag{3.13}$$

Since the Intensities of a peak are directly connected to the total relaxation rate by

$$I_{\mu\nu} \propto \exp(-\Gamma_{\mu\nu} \cdot t)$$

it is possible to calculate the pure dipole-dipole cross correlated relaxation rate  $\Gamma_{A1A2,B1B2}^{c,DQ}$  and  $\Gamma_{A1A2,B1B2}^{c,ZQ}$  from the four intensities of the quartets by

$$\Gamma_{A1A2,B1B2}^{c,DQ} = \frac{1}{4 \cdot T} \ln \frac{I^{DQ}(\alpha\beta) \cdot I^{DQ}(\beta\alpha)}{I^{DQ}(\beta\beta) \cdot I^{DQ}(\alpha\alpha)} + \frac{1}{2}(W_2 - W_0) \tag{3.14}$$

and

$$\Gamma_{A1A2,B1B2}^{c,ZQ} = \frac{1}{4 \cdot T} \ln \frac{I^{ZQ}(\alpha\alpha) \cdot I^{ZQ}(\beta\beta)}{I^{ZQ}(\alpha\beta) \cdot I^{ZQ}(\beta\alpha)} - \frac{1}{2}(W_2 - W_0). \tag{3.15}$$

with T being the delay during which the double- and zero-quantum coherences are evolving.

The average of the  $\Gamma_{A1A2,B1B2}^{c,DQ}$  and  $\Gamma_{A1A2,B1B2}^{c,ZQ}$  is given as

$$\frac{\Gamma_{A1A2,B1B2}^{c,DQ} + \Gamma_{A1A2,B1B2}^{c,ZQ}}{2} = \frac{1}{8 \cdot T} \ln \frac{I^{ZQ}(\alpha\alpha) \cdot I^{ZQ}(\beta\beta) \cdot I^{DQ}(\alpha\alpha) \cdot I^{DQ}(\beta\beta)}{I^{ZQ}(\alpha\beta) \cdot I^{ZQ}(\beta\alpha) \cdot I^{DQ}(\alpha\beta) \cdot I^{DQ}(\beta\alpha)} \tag{3.16}$$

and depends only on the experimentally measurable intensities of the double- and zero-quantum quartets.



## The Cross-Correlated Relaxation in the Cartesian Product Operator Formalism

The following section is adapted from Boisbouvier & Bax [63]:

For the case of a three spin system A, M, X with negligible CSA the transfer between the four M-spin single-quantum coherences can be described by

$$\frac{d}{dt} \begin{pmatrix} M_+(t) \\ 2M_+A_z(t) \\ 2M_+X_z(t) \\ 4M_+A_zX_z(t) \end{pmatrix} = -(L + iK) \begin{pmatrix} M_+(t) \\ 2M_+A_z(t) \\ 2M_+X_z(t) \\ 4M_+A_zX_z(t) \end{pmatrix} \quad (3.17)$$

with

$$L = \begin{pmatrix} R(M_+) & 0 & 0 & \Gamma_{MA,MX}^{DD,DD} \\ 0 & R(2M_+A_z) & \Gamma_{MA,MX}^{DD,DD} & 0 \\ 0 & \Gamma_{MA,MX}^{DD,DD} & R(2M_+X_z) & 0 \\ \Gamma_{MA,MX}^{DD,DD} & 0 & 0 & R(4M_+A_zX_z) \end{pmatrix} \quad (3.18)$$

and

$$K = \begin{pmatrix} \omega_M & \pi \cdot J_{MA} & \pi \cdot J_{MX} & 0 \\ \pi \cdot J_{MA} & \omega_M & 0 & \pi \cdot J_{MX} \\ \pi \cdot J_{MX} & 0 & \omega_M & \pi \cdot J_{MA} \\ 0 & \pi \cdot J_{MX} & \pi \cdot J_{MA} & \omega_M \end{pmatrix}, \quad (3.19)$$

where  $\omega_M$  is the Larmor frequency of spin M,  $J_{IS}$  is the scalar coupling between spins I and S,  $R(I)$  is the autorelaxation rate of spin I and  $\Gamma_{MA,MX}^{DD,DD}$  is the dipole-dipole cross-correlated relaxation rate between the spin vectors MA and MX. From this the exchange between the four M-spin single-quantum coherences are in the absence of scalar couplings for an initial condition of  $M_+ = 1$ :

$$M_+ \cosh(-\Gamma_{MA,MX}^{DD,DD} t) \exp(-R_2 t) + 4M_+A_zX_z \sinh(-\Gamma_{MA,MX}^{DD,DD} t) \exp(-R_2 t) \quad (3.20)$$

and for  $M_+A_z = 1$ :

$$M_+A_z \cosh(-\Gamma_{MA, MX}^{DD, DD} t) \exp(-R_2 t) + 4M_+X_z \sinh(-\Gamma_{MA, MX}^{DD, DD} t) \exp(-R_2 t) \quad (3.21)$$

These rules for the evolution of CCR can also be derived directly from equations 3.10 of the last section by introduction of cartesian product operators instead of the single product operators.

### The CCR Evolution Building Block

In this study three kinds of experiments are used for the measurement of the cross-correlated relaxation rates:

- 1) Experiments with an coupled indirect dimension as for the measurement of backbone  $NH - C_\alpha H_\alpha$  CCR rates. In this experiments a quartet from the two involved couplings is detected, from which using the peak intensities the CCR rates can be determined using equation 3.16.
- 2) Experiments which use cross-correlated relaxation as a transfer mechanism (RACT) between the two atom groups. In these experiments the intensity of the cross peak is directly depending on the CCR rates according to the equations 3.20 and 3.21.
- 3) Experiments which have a special block built in which, the cross-correlated relaxation is allowed to evolve as in Felli et al. [55]. The behavior of the chemical shift anisotropy and the dipole-dipole interactions is discussed in the following:

An example of such a block from the inter methyl experiment is shown in figure 3.2 with starting transverse magnetization on the carbons. The block includes three  $180^\circ$  pulses separating four delays  $((\tau + \Delta)/4, (\tau - \Delta)/4, (\tau + \Delta)/4$  and  $(\tau - \Delta)/4$ ). Therefore the magnetization transfer between the residues i and j in the block is given by

$$\begin{aligned} 4H_{iz}C_{ix}C_{jy} &= 4H_{iz}C_{ix}C_{jy}[\cosh(\Gamma_{C_i H_i C_j H_j}^c \tau) \cos^2(\pi J_{CH} \Delta') - \sinh(\Gamma_{C_i H_i C_j H_j}^c \tau) \sin^2(\pi J_{CH} \Delta')] \\ &\quad - 4H_{jz}C_{jx}C_{iy}[\sinh(\Gamma_{C_i H_i C_j H_j}^c \tau) \cos^2(\pi J_{CH} \Delta') + \cosh(\Gamma_{C_i H_i C_j H_j}^c \tau) \sin^2(\pi J_{CH} \Delta')] \end{aligned} \quad (3.22)$$

For the determination of the CCR rate the experiment has to be conducted twice. Once with  $\Delta = 0$  as a reference experiment and once cross experiment with  $\Delta = 1/(2J_{CH})$ . Since

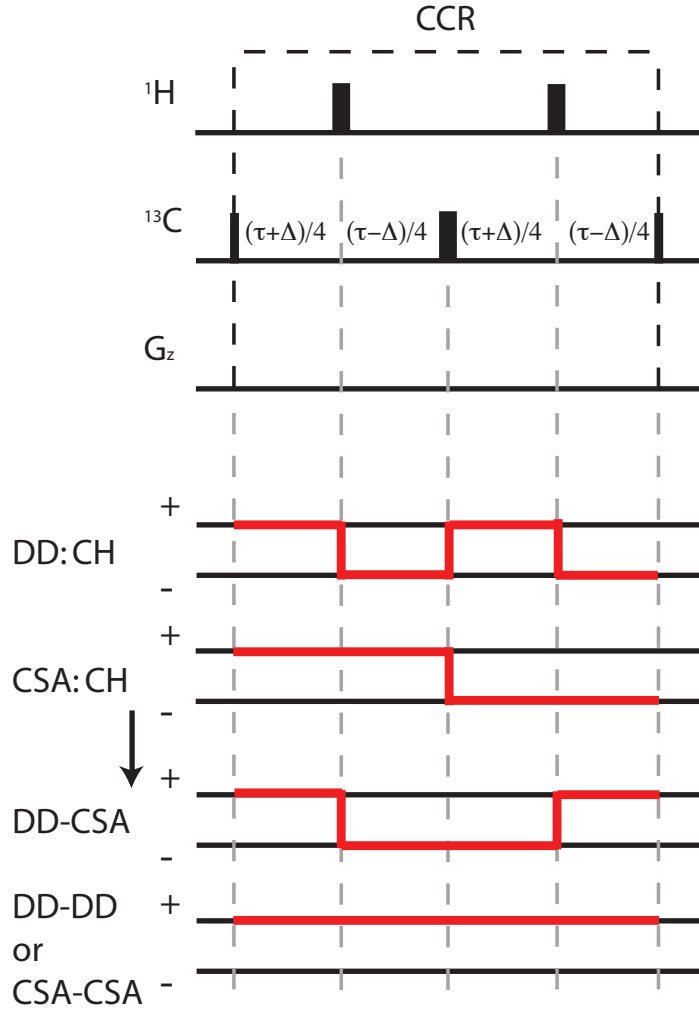


**Figure 3.2:** The top of the figure shows the typical block from pulse sequences that are used later on, in which the cross-correlated relaxation is allowed to evolve. Three  $180^\circ$  pulses are separate four delays,  $(\tau + \Delta)/4$ ,  $(\tau - \Delta)/4$ ,  $(\tau + \Delta)/4$  and  $(\tau - \Delta)/4$ . The lower part of the figure shows the signs of the evolution of the dipole-dipole (DD) and chemical shift relaxation (CSA) relaxation processes and their combinations from these four delays. The signs for CCR rates based on DD-DD and CSA-DD interactions are shown in equations 3.12 and 3.13. From these equations also the change in the signs by a  $180^\circ$  pulse can be determined by comparing the signs for  $\Gamma_{\alpha\alpha}$  and  $\Gamma_{\beta\beta}$  or  $\Gamma_{\beta\alpha}$  and  $\Gamma_{\alpha\beta}$ , respectively.

the second term  $4H_{jz}C_{jx}C_{iy}$  leads to the transfer between the residues  $i$  and  $j$ , the intensity of the reference experiment is therefore modulated by  $\sinh(\Gamma_{C_iH_iC_jH_j}^c\tau)$ , while it is in the cross experiment modulated by  $\cosh(\Gamma_{C_iH_iC_jH_j}^c\tau)$ . By dividing of the two intensities the CCR rate can be determined by

$$I^{cross}/I^{ref} = \tanh(\Gamma_{C_iH_iC_jH_j}^c\tau) \quad (3.23)$$

For experiments in which the transverse magnetization is on the hetero atoms during the CCR block also the chemical shift anisotropy (CSA) has to be taken into consideration for the cross-correlated relaxation process. Therefore the evolving CCR rate could in principal not only consist of the desired dipole-dipole( $C^1H^1$ ) - dipole-dipole( $C^2H^2$ ) interaction, but also of dipole-dipole( $C^1H^1$ ) - CSA( $C^1$ ), dipole-dipole( $C^1H^1$ ) - CSA( $C^2$ ), dipole-dipole( $C^2H^2$ ) - CSA( $C^1$ ), dipole-dipole( $C^2H^2$ ) - CSA( $C^2$ ) and CSA( $C^1$ ) - CSA( $C^2$ ) interactions. With the construction of the CCR block these undesired interactions can be cancelled out as described in the following:

As shown in figure 3.2 the dipole-dipole interactions will be inverted by each of the three  $180^\circ$  pulses, while the CSA relaxation process is only inverted by the  $180^\circ$  carbon pulse, since the carbon CSA is independent of any hydrogens. The combination of dipole-dipole( $C^1H^1$ ) - dipole-dipole( $C^2H^2$ ) or CSA( $C^1$ ) - CSA( $C^2$ ) is therefore evolving for the whole total delay  $\tau$ . The combination of any dipole-dipole interaction with a CSA process is evolving positively for the delays 1 and 4, but negatively for the delays 2 and 3. Since delay 1 is equal to 3 and delay 2 to 4, the evolution in total is refocused.

The CSA( $C^1$ ) - CSA( $C^2$ ) interaction can be cancelled out using another attribute of the CCR building block. The reference and the CCR evolving experiments differ only by a different value of  $\Delta$ , which leads to a shift of the two  $180^\circ$  pulses on protons. However the CSA relaxation process is independent of any protons and therefore is not affected by this change of  $\Delta$ . Therefore the CSA - CSA process contribute the same to the CCR rate in the reference and the CCR evolving experiment and is cancelled out by the division of the intensities of the two experiments.

## Separation of the Time Scales for the Calculation of CCR Rates

The following section origins from the work of Dr. Donghan Lee (unpublished) based on [56]:

For the cross-correlated relaxation of two bonds (A-B and C-D),

$$R_{AB,CD} = \frac{\mu_0^2}{4} \cdot \frac{\gamma_A \cdot \gamma_B \cdot \gamma_C \cdot \gamma_D \cdot \gamma_A \cdot h^2}{4 \cdot \pi \cdot r_{AB}^3 \cdot r_{CD}^3} \langle j_{CCR}(0) \rangle \quad (3.24)$$

with

$$\frac{1}{\tau'} = \frac{1}{\tau_c} + \frac{1}{\tau_{CCR}} \quad (3.25)$$

If the motion is much faster than the overall tumbling ( $\tau_{CCR} \ll \tau_c$ ),  $\tau' = \tau_{CCR}$ , the spectral density is given by

$$j_{CCR}^{fast}(\omega) = \frac{2}{5} \left( \frac{S^2 \tau_c}{1 + (\omega \tau_c)^2} + \frac{(P_2(\cos \theta) - S^2) \tau_{CCR}}{1 + (\omega \tau_{CCR})^2} \right) \quad (3.26)$$

If the motion is much slower than the overall tumbling ( $\tau_{CCR} \gg \tau_c$ ),  $\tau' = \tau_c$ , the spectral density is given by

$$j_{CCR}^{fast}(\omega) = \frac{2}{5} \left( \frac{S^2 \tau_c}{1 + (\omega \tau_c)^2} + \frac{(P_2(\cos \theta) - S^2) \tau_c}{1 + (\omega \tau_c)^2} \right) = \frac{2}{5} \cdot \frac{P_2(\cos \theta) \tau_c}{1 + (\omega \tau_c)^2} \quad (3.27)$$

From this it leads to

$$\begin{aligned} R_{AB,CD} &= \frac{\mu_0^2}{4} \cdot \frac{\gamma_A \cdot \gamma_B \cdot \gamma_C \cdot \gamma_D \cdot \gamma_A \cdot h^2}{4 \cdot \pi \cdot r_{AB}^3 \cdot r_{CD}^3} \left\langle \frac{2}{5} \cdot P_2(\cos \theta) \tau_c \right\rangle \\ &= \frac{\mu_0^2}{4} \cdot \frac{\gamma_A \cdot \gamma_B \cdot \gamma_C \cdot \gamma_D \cdot \gamma_A \cdot h^2}{10 \cdot \pi \cdot r_{AB}^3 \cdot r_{CD}^3} \langle P_2(\cos \theta) \tau_c \rangle \end{aligned} \quad (3.28)$$

Thus,

$$R_{AB,CD} = \frac{\mu_0^2}{4} \cdot \frac{\gamma_A \cdot \gamma_B \cdot \gamma_C \cdot \gamma_D \cdot \gamma_A \cdot h^2}{10 \cdot \pi \cdot r_{AB}^3 \cdot r_{CD}^3} P_2(\cos \theta) \tau_c S_{AB}^{RDC} S_{CD}^{RDC} S_{AB}^{libr} S_{CD}^{libr} \quad (3.29)$$

and

$$R_{AB,CD} = \frac{\mu_0^2}{4} \cdot \frac{\gamma_A \cdot \gamma_B \cdot \gamma_C \cdot \gamma_D \cdot \gamma_A \cdot h^2}{10 \cdot \pi \cdot r_{AB}^3 \cdot r_{CD}^3} \langle P_2(\cos \theta) \rangle \tau_c S_{AB}^{libr} S_{CD}^{libr} \quad (3.30)$$

for the static structure and the ensembles, respectively, with  $\mu_0$  the magnetic susceptibility of vacuum,  $\hbar$  the Plank constant,  $\gamma_x$  the gyromagnetic ratio of nucleus X,  $r_{XHx}$  the distance between the nuclei X and Hx,  $\theta_{XHx,YHy}$  the angle between the internuclear vectors XHx and YHy and  $\tau_c$  the correlation time of ubiquitin. The  $S^{libr}$  factor = 0.95 is used to compensate for a well-known effect that a part of the dynamic of the bond vector is absorbed by the tensor optimization routine when computing NH order parameter from ensembles restrained with rdc [104].  $S^{RDC}$  is the correction factor for the contribution of sub-ms uncorrelated dynamics. This is calculated by Dr. Bryn Fenwick and Prof. Xavier Salvatella from the ERNST ensemble [42] as described in [37].

### 3.3 Correlated Motions of the Protein Backbone

The rdc-derived structural ensembles mentioned in chapter 1 show various correlated motions. CCR rates of NH-NH internuclear vectors of sequential residues and CCR rates of the  $NH - C\alpha H\alpha$  intraresidual internuclear vectors were used to validate the correctness of the predicted correlated backbone motions under consideration of the restraining parameter of the structural ensembles. With the combination of NH-NH and  $NH - C\alpha H\alpha$  CCR rates all degrees of freedom in the protein backbone should be covered (assuming perfectly fixed peptide planes). Also, with the interresidual NH-NH CCR rates correlated motion along the backbone planes it is possible to connect correlated motions between sequential residues and follow in this way long distance correlated motions. Therefore, these backbone CCR rates are an important factor to verify the dynamical aspects of ensembles. Since the atom pairs are only separated by three bonds (NH-NH) or one bond ( $NH - C\alpha H\alpha$ ) all transfers in the experiments can be achieved via scalar couplings in a very effective manner.

#### 3.3.1 Material and Methods

##### The Sample

The wild-type  $^{15}N, ^{13}C$ -labeled human ubiquitin expressed according to a previous protocol by Johnson et al. [90] was kindly provided by Dr. Stefan Becker and Karin Giller. 10 mg ubiquitin were dissolved in 350  $\mu L$  50 mM sodium phosphate buffer with 100 mM NaCl at pH = 6.8, 0.1 % (w/v) together with  $NaN_3$ . The measurements were conducted at a temperature of 308 K.

The CCR rates of the intraresidual  $C\alpha H\alpha$  atom pairs were measured by a NMR experiment adapted from Vögeli & Yao [61]. The pulse sequence scheme is shown in figure 3.3. In this 3D-experiment the amide proton magnetization is first transferred to the amide nitrogen, followed by a constant-time block in which the nitrogen chemical shift is probed (point a) and the common coherence between the NH and the  $C\alpha H\alpha$  group is built up. In the following block, the magnetization on the nitrogen and the carbon are both transverse (point b) and therefore in the second incremented time the sum of the chemical shifts of both spins is measured. Since the protons are not decoupled the NH- and the  $C\alpha H\alpha$ -couplings are evolving and the signal of each residue results in this dimension as a quartet. Each peak of the quartet represents one of the four possible combinations of  $\alpha$  and  $\beta$  state of the amide proton and the  $H\alpha$ . The intensities of all four peaks have different dependencies on the CSA and the dipole-dipole relaxation rates. Afterwards, the antiphase operator between nitrogen and carbon is refocused, while the coupling to the amide proton evolves (point c). In the final INEPT step the transverse magnetization is transferred back and refocused on the proton (point d), where it is then detected.

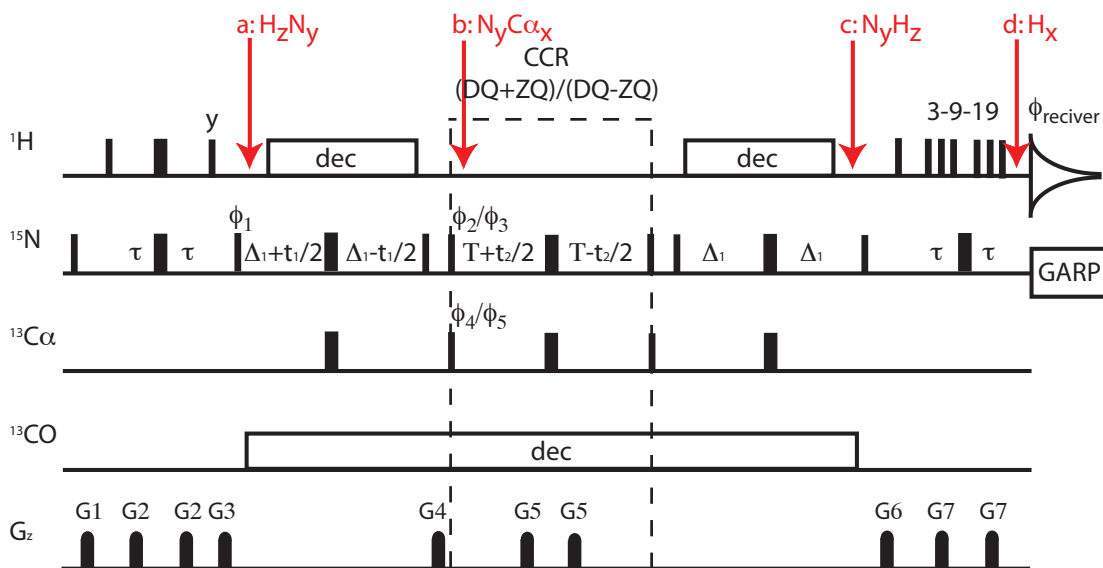


**Figure 3.3:** Pulse scheme for the NH -  $C\alpha H\alpha$  CCR rate measurement. Three-dimensional  $^{15}\text{N}$  - ( $^{15}\text{N} + ^{13}\text{C}$ ) -  $^1\text{H}$  transfer scheme. Narrow and wide pulses correspond to flip angles of  $90^\circ$  and  $180^\circ$ , respectively. Unless indicated otherwise, all radio-frequency pulses are applied with phase x. The  $^1\text{H}$  decoupling is conducted with a dipsi2 decoupling ( $\nu = 263$  Hz), while the selective CO decoupling is achieved with a selective seduce decoupling sequence. The water suppression is achieved by a 3-9-19 Watergate [105]. Quadrature detection in the  $^{13}\text{C}$  dimension is achieved by incrementing  $\phi_1$  in the usual States-TPPI manner. The  $\Delta_1$  delays are set to 14 ms, T delays are set to 14.42 ms and the  $\tau$  delays are set to 2.7 ms. Phase cycling:  $\phi_1 = x, -x$ ;  $\phi_2 = 2(x), 2(-x)$ ;  $\phi_3 = 4(x), 4(-x)$ ;  $\phi_4 = 2(y), 2(-y)$ ;  $\phi_5 = 4(y), 4(-y)$ ;  $\phi_{receiver} = x, -x, -x, x, -x, x, x, -x$ . The interleaved manner of this experiment is achieved by switching after each experiment from the phases  $\phi_2$  and  $\phi_4$  to  $\phi_3$  and  $\phi_5$  and back. All gradients are sine shaped, with a duration of  $G_{1,2,3,4,5,6,7} = 1000, 700, 1000, 800, 800, 1000, 800 \mu\text{s}$ . The measurement was run with  $85(t_1) \times 33(t_2) \times 512(t_3)$  complex points. The relaxation delay is 1.0 s

This pulse sequence records the sum and the difference of the double quantum (DQ) and the zero quantum (ZQ) magnetization in an interleaved manner. This means that each experiment step is conducted twice once measuring the sum of (DQ + ZQ) and afterwards the difference (DQ - ZQ). In this way small changes in the experimental environment like small temperature changes affects both spectra in the same way. The measured data are afterwards split and processed separately to a (DQ + ZQ) and a (DQ - ZQ) spectrum. These spectra are afterwards added and subtracted from each other to achieve pure DQ and ZQ spectra. One example spectrum is shown in figure 3.4. The processing was conducted using

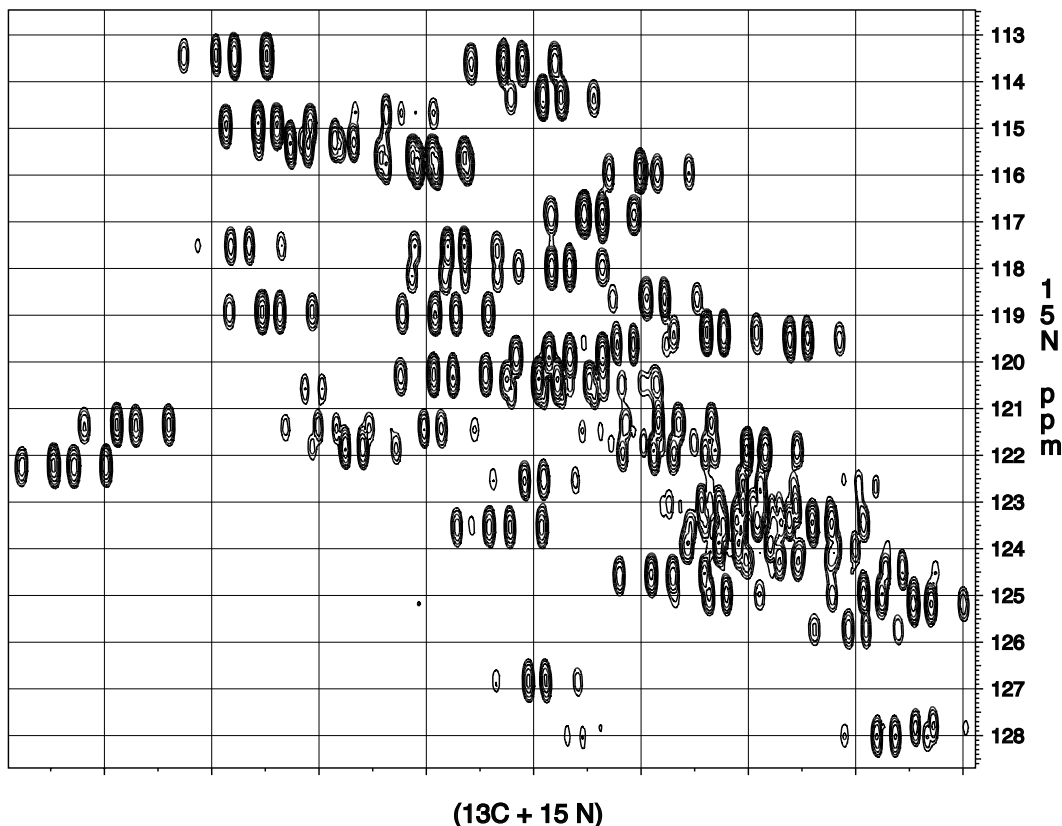


**Figure 3.4:** Spectrum of the  $^{15}\text{N}$ , ( $^{15}\text{N} + ^{13}\text{C}$ ) dimensions of the backbone CCR measurement. The measurement was conducted on a 600 MHz spectrometer equipped with a QCI cryo-probe head. For window functions, square cosine functions were used and spectra were zero-filled to 2048 x 256 x 2048 complex points.

the program NMRPipe [106].

In the second indirect dimension due to the two splittings of the  $^{15}\text{N}^1\text{H}$  and the  $^{13}\text{C}_\alpha^1\text{H}_\alpha$  scalar couplings each residue shows a quartet. The peaks were assigned and the intensities determined using the program CARA (R. Keller and K. Wuthrich [107]). By division of the intensities of the outer peaks by the intensities of the inner peaks of the quartet (equation 3.16) the dependency of the CSA relaxation effects can be removed and the pure dipole-dipole relaxation part of the NH -  $\text{C}_\alpha\text{H}_\alpha$  atom pairs can be extracted.

$$R_{CCR} = \frac{1}{8 \cdot 28.84 \cdot 10^{-3} \cdot s} \ln \frac{I^{ZQ}(\alpha\alpha) \cdot I^{ZQ}(\beta\beta) \cdot I^{DQ}(\alpha\alpha) \cdot I^{DQ}(\beta\beta)}{I^{ZQ}(\alpha\beta) \cdot I^{ZQ}(\beta\alpha) \cdot I^{DQ}(\alpha\beta) \cdot I^{DQ}(\beta\alpha)} \quad (3.31)$$



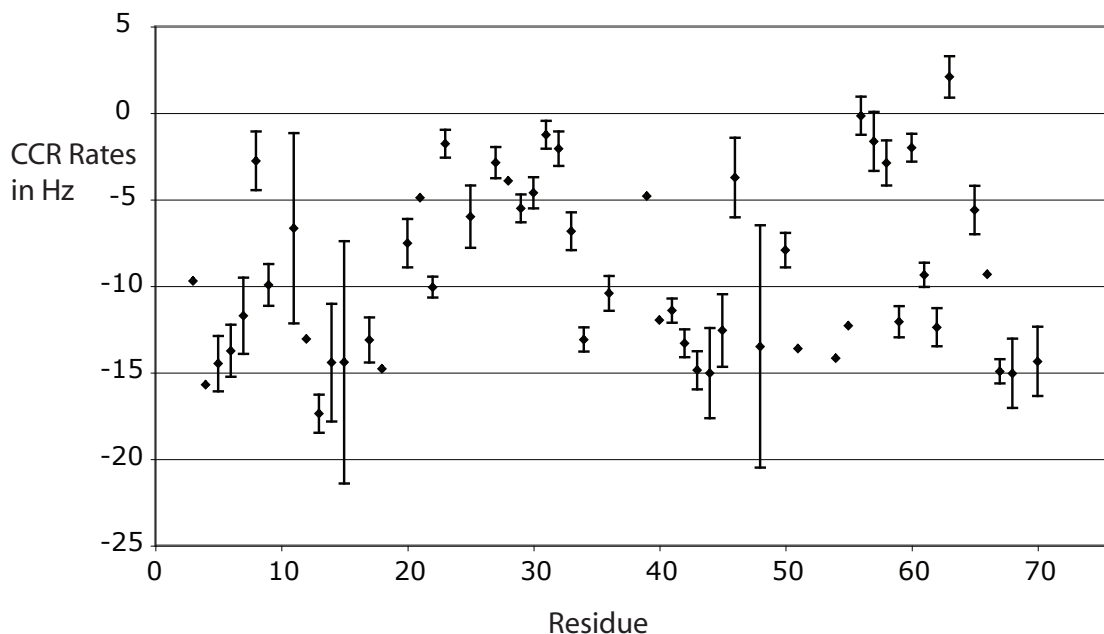


**Figure 3.5:** The graph shows the experimentally measured CCR rates and corresponding experimental errors of NH -  $C\alpha H\alpha$  pairs in the protein backbone of ubiquitin.

CCR rates of 55 residues could be determined. They are shown in figure 3.5 and in the appendix in table 6.1.

### 3.3.2 Comparison with predictions

Ubiquitin is a very well investigated protein and several structures and ensembles are published. Many of the structures and ensembles describe the dynamical aspects of the protein in different ways. Some like the structure by Vijay-Kumar et al. (pdb code: 1ubq) [108] determined by x-ray crystallography or the structure ensemble by Cornilescu et al. (pdb code: 1d3z) [109] determined by NMR spectroscopy includes no information about the dynamics of the protein in liquid state, while the later one use NH RDCs as structural restraints. Another two structure ensembles by Richter et al. (pdb code: 2nr2) [83] and by Lindorff-Larsen et al. (pdb code: 1xqq) [84] were restrained against Lipari-Szabo order parameter and therefore can represent the protein dynamic up to ns. Finally, two rdc based structure ensembles were used for the comparison. The ERNST ensemble by Fenwick et al. (pdb code: 2kox) [42] is restrained against the NH backbone RDCs, while the EROS ensemble by Lange & Lakomek et al. (pdb code: 2k39) [37] also used the H(N)C' backbone RDCs and from the side chain the methyl group CH rdc.

The CCR rates for the structural ensembles (1d3z, 2nr2, 1xqq, 2k39, 2kox) were calculated by Dr. Bryn Fenwick using equation 3.30 and equation 3.29 for the static structure of 1ubq.

In addition to the newly measured NH -  $C\alpha H\alpha$  CCR rates, complimentary NH - NH CCR rates of sequential residues published by Pelupessy et al. [58] were used for the evaluation based on the CCR rate prediction of the structures and ensembles.

### 3.3.3 Results and Discussion

The extracted CCR rates were used to validate the prediction of correlated backbone motions by several ubiquitin structures and ensembles. The correlation plots of the experimental CCR rates against the backcalculated ones are shown in figure 3.6 for the NH - NH CCR rates and in figure 3.6 for the  $C\alpha H\alpha$  CCR rates.

The comparison between predicted and experimentally measured backbone CCR rates show clearly the better prediction of correlated motions correlation for the rdc-restrained ensembles (rmsd: EROS: 0.50 Hz (NH-NH) respective 1.66 Hz ( $NH-C\alpha H\alpha$ ), ERNST: 0.46 Hz respective 0.61 Hz) than for the other structures and ensembles (rmsd: 1ubq: 1.05 Hz respective 2.10 Hz, 2nr2: 1.35 Hz respective 2.06 Hz and 1xqq: 1.63 Hz respective 2.38 Hz). Only the structure 1d3z (1d3z: 0.57 Hz respective 1.76 Hz) comes near to accuracy of the RDC-based ensembles. This can be explained with the use of RDCs as orientation restraints in the creation process of this structure.

In this way it is possible to validate that the RDC-based ensembles are a good representation at least for short range correlated motions. Due to the overlap of intraresidual  $NH-C\alpha H\alpha$  and interresidual NH-NH CCR rates it is possible to investigate correlated motions of the protein backbone also for longer distances. These results are published in Fenwick et al. [42].

It is possible to distinguish special modes from each other from the experimentally CCR rates. For this purpose the experimentally  $NH - C\alpha H\alpha$  CCR rates are divided by the backcalculated CCR rates from the average inter vector angle of the structure ensemble ERNST (pdb code: 2kox) [42] and the RDC derived order parameters of the involved atom pairs as shown in figure 6.2. A fully correlated motional mode, in which the internuclear vectors move always in the same direction and therefore the inter vector angles stays constant, would have a quotient larger than 1. In contrast, a fully anticorrelated motional mode, in which the internuclear vectors move always in opposing directions, would have a quotient smaller than 1.

The implemented three-dimensional experiment is an efficient way to measure the CCR rates between atom pairs as long as the joint coherence between the atom pairs can be built up by sufficiently large scalar couplings. Even with the relatively large coupling between the amide nitrogen and the Ca of around 18 Hz it took around 3 days measurement time at a 600 MHz spectrometer with a cryo probehead to achieve a sufficiently high signal to noise.

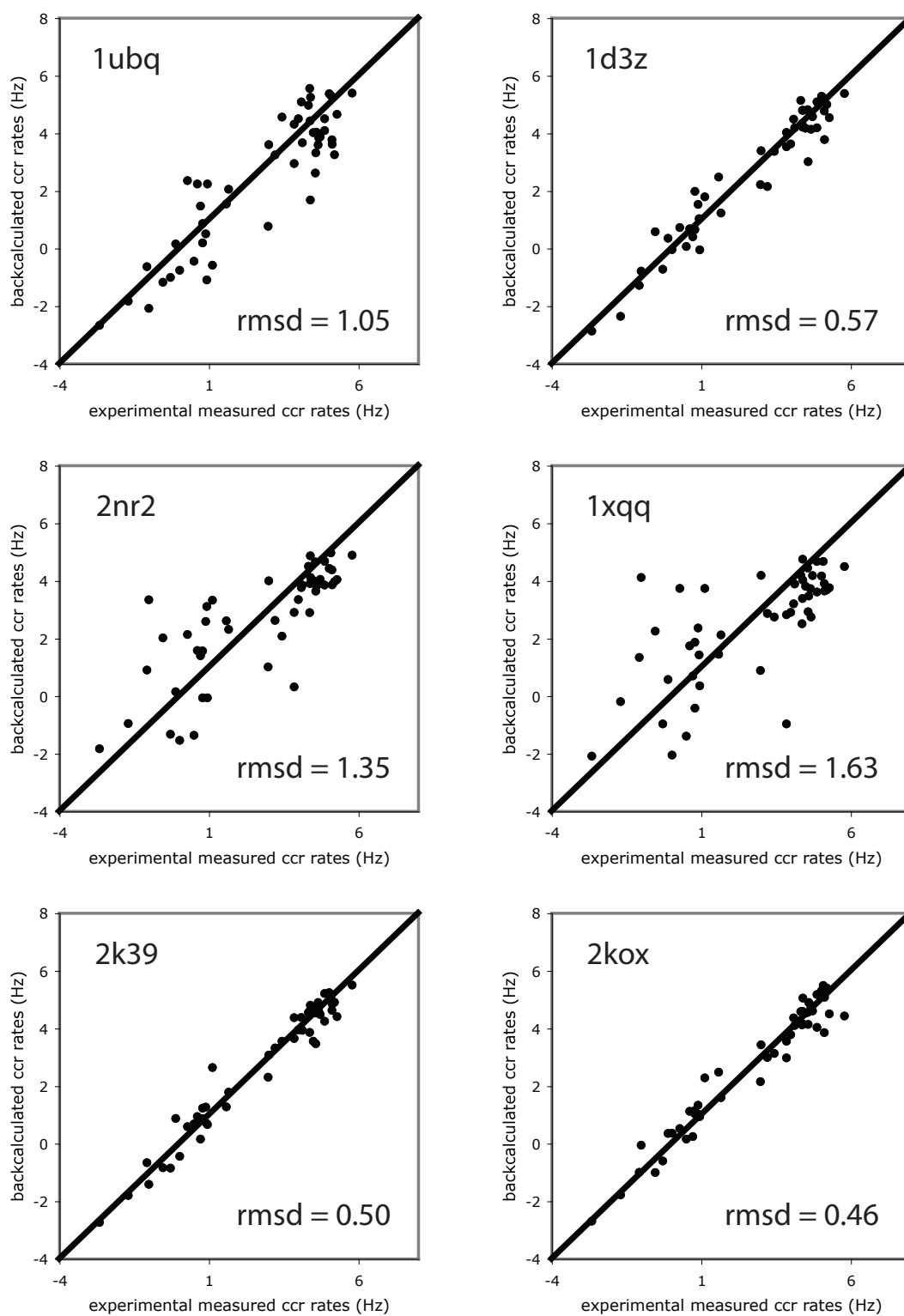


**Figure 3.6:** Correlation plots of the experimental and backcalculated NH - NH CCR rates.

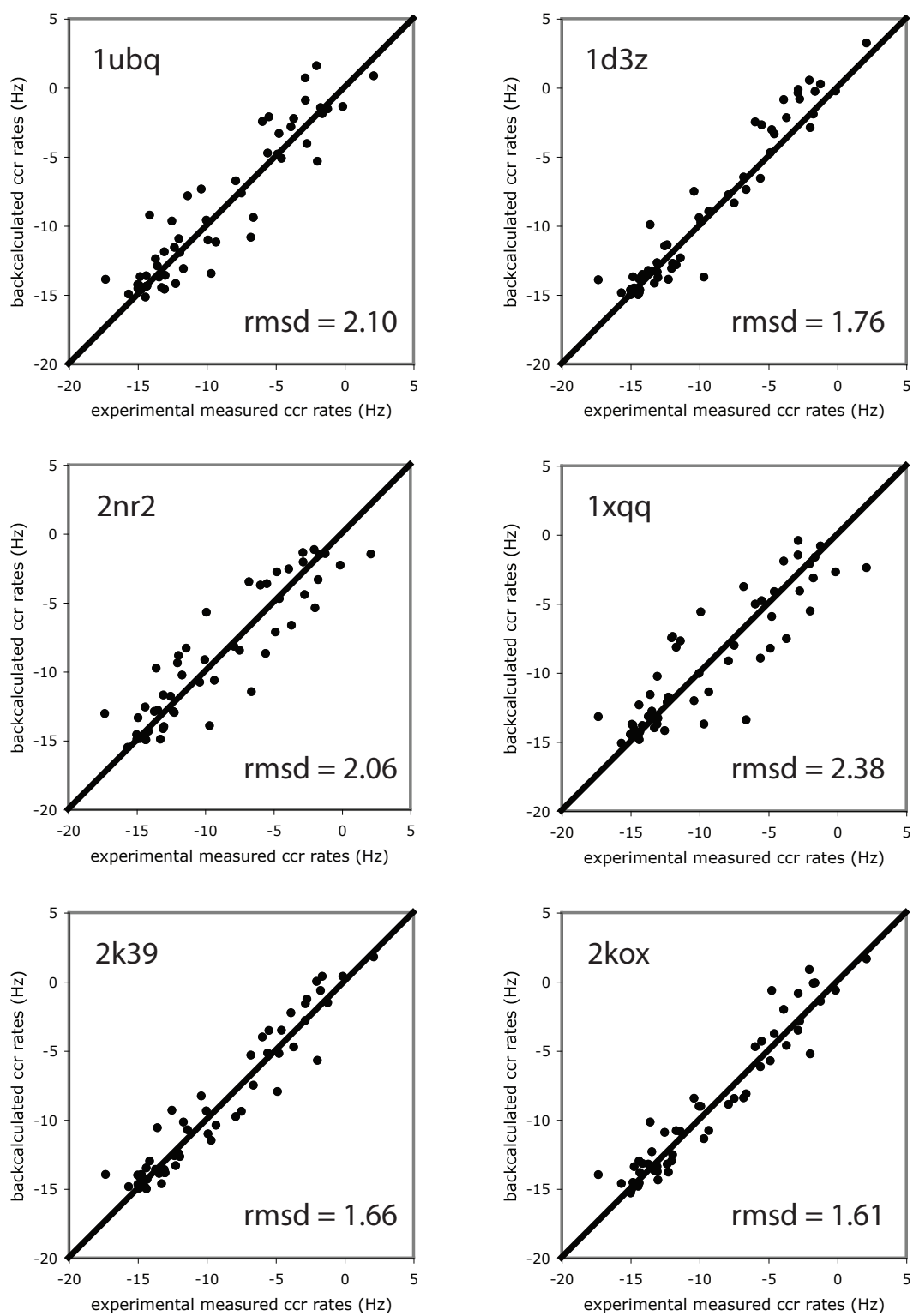


**Figure 3.7:** Correlation plots of the experimental and backcalculated NH -  $C\alpha H\alpha$  CCR rates.

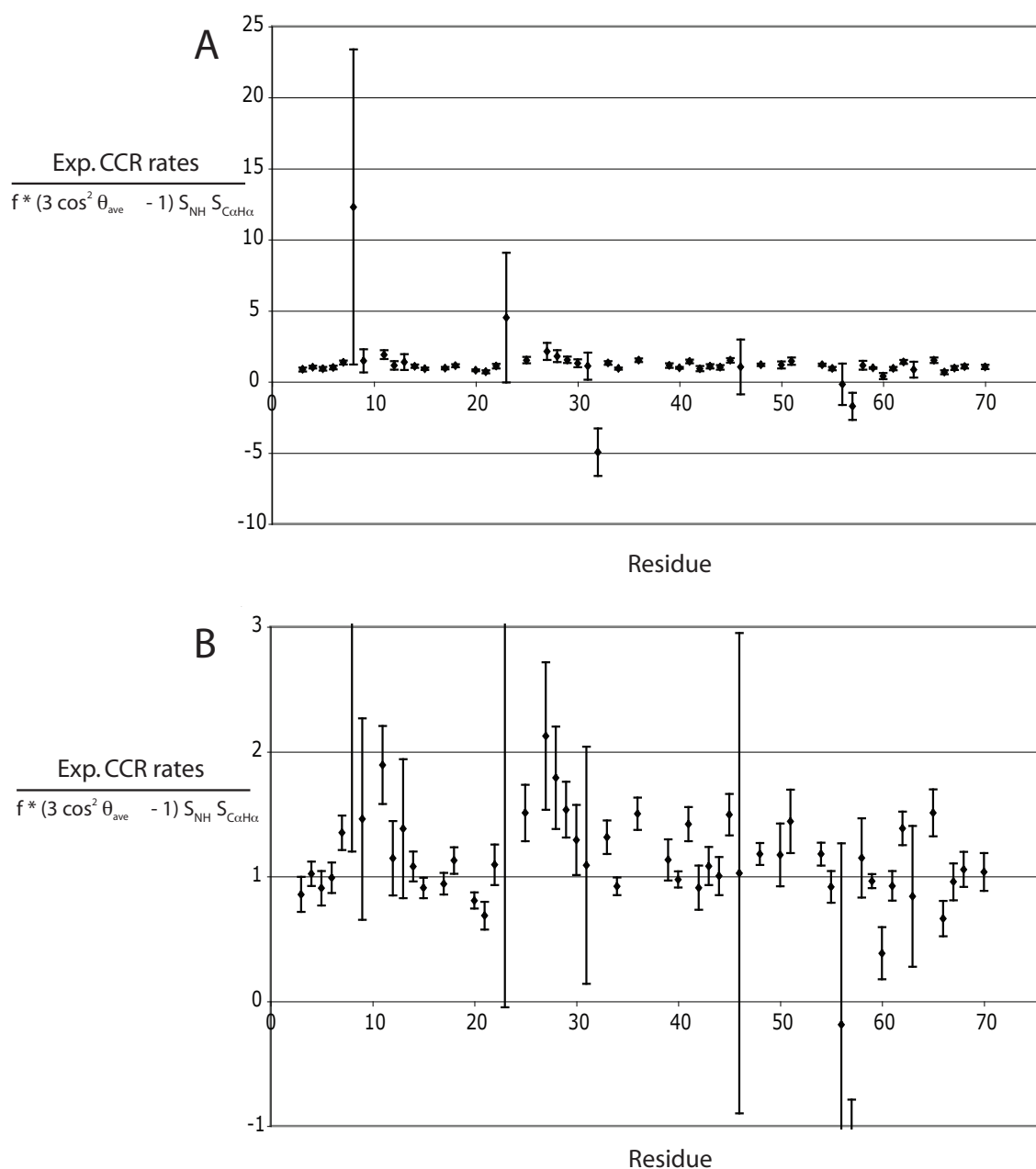


**Figure 3.8:** Graph A shows the quotient of the experimental CCR rates of  $NH - C\alpha H\alpha$  pairs in the protein backbone of ubiquitin divided by the theoretical CCR rates back calculated from the average inter vector angles of the ERNST ensemble (pdb code: 2kox) [42] and the RDC derived order parameters of the involved atom pairs. The prefactor  $f$  equals  $(\frac{\mu_0}{4\pi})^2 \cdot (\frac{\hbar}{2\pi})^2 \cdot \frac{\gamma_N \cdot \gamma_H}{r_{NH}^3} \cdot \frac{\gamma_C \cdot \gamma_H}{r_{C\alpha H\alpha}^3} \cdot \frac{2}{5} \cdot \tau_c$ . Graph B shows an expanded view of Graph A in the most interesting region around a quotient of 1.

### 3.4 Correlated Motions between Secondary Structure Elements

In Fenwick et al. [42] it has been shown that the ERNST structural ensemble is able to reproduce the experimentally measured backbone CCR rates well. In addition trans-hydrogen bond scalar couplings  ${}^3hJ_{NC'}$  have been used to investigate correlated motion between two connected  $\beta$ -strands. In this way it was possible to identify correlated secondary structure motion in the  $\beta$ -sheet. For an additional independent validation three experiments were developed to measure CCR rates between either amide NH or  $C\alpha H\alpha$  groups on separated  $\beta$ -strands.

In the NH experiment residual dipolar couplings (RDCs) have been used for the magnetization transfer from one  $\beta$ -strand to the second. Therefore the protein sample had to be prepared in a strong anisotropic alignment medium, which produced sufficiently large H-H rdc's, but also caused problems for the measurement due to inhomogeneities in the sample volume and increased relaxation.

For the measurement of the  $C\alpha H\alpha$  CCR rates, two experiments were used on basis of the relaxation-allowed coherence transfer (RACT) transfer [110, 111, 112, 113]. In the first experiment the measurement of the CCR rate was conducted with a building block in which the cross-correlated relaxation effect is evolving (as shown in figure 3.2). In this way the CCR rate of the  $C^1\alpha H^1\alpha - C^2\alpha H^2\alpha$  pair can be measured. The second experiment uses the transfer amplitudes of the two RACT transfers, which depend directly on the cross-correlated relaxation rates, for the measurement of the CCR rates. Due to the two transfer steps, the two CCR rates  $C^1\alpha H^1\alpha - H^1\alpha H^2\alpha$  and  $C^2\alpha H^2\alpha - H^1\alpha H^2\alpha$  are measured in this experiment.

#### 3.4.1 Material and Methods

##### The $\beta$ -Strand NH Amide CCR Experiment

The wild-type  ${}^{15}N$ -labeled human ubiquitin expressed according to a previous protocol by Johnson et al. [90] was kindly provided by Dr. Stefan Becker and Karin Giller. Samples of ubiquitin were dissolved in two anisotropic alignment media:

Bicelles: 40.2 mg DLPC, 9.8 mg DHPC ( DLPC:DHPC ratio 3:1, 10% (w/v) purchased by Avanti Polar Lipids Inc., AL, USA) were dissolved in 500  $\mu L$  phosphate buffer (50 mM  $NaPO_4$ , 100 mM NaCl, pH = 6.8, 0.1 % (w/v)  $NaN_3$ , 10 % (v/v) D2O). The splitting of the deuterium signal due to the anisotropic medium was 16.7 Hz. 8.5 mg of  ${}^{15}N$ -labeled

ubiquitin was solved in this alignment medium.

Phages: 16 mg phages (purchased by Asla Biotech, Riga, Latvia) was solved in 350  $\mu\text{L}$  phosphate buffer (50 mM  $\text{NaPO}_4$ , 100 mM NaCl, pH = 6.8, 0.1 % (w/v)  $\text{NaN}_3$ , 10 % (v/v) D2O). The splitting of the deuterium signal due to the anisotropic medium was 25.0 Hz. 16.4 mg of  $^{15}\text{N}$ -labeled ubiquitin was solved in this alignment medium.

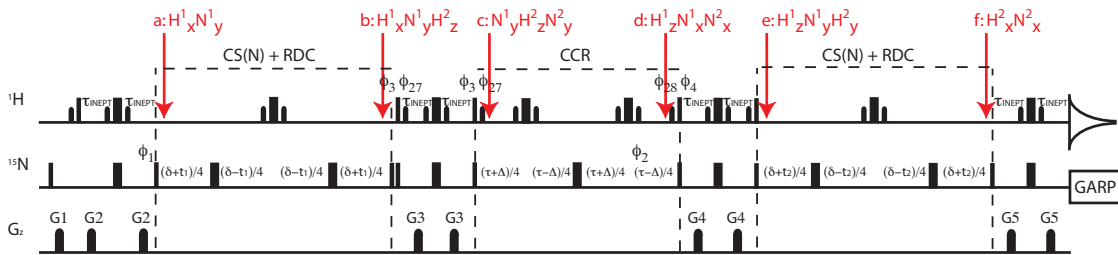


**Figure 3.9:** Pulse scheme for transfer amplitude modulated NH - NH CCR rate measurement. Narrow and wide pulses correspond to flip angles of  $90^\circ$  and  $180^\circ$ , respectively. Unless indicated otherwise, all radio-frequency pulses are applied with phase x. The shaped flip back  $^1\text{H}$  pulses are of the  $90^\circ$  gaussian type (1500 ms length at 900 MHz). Quadrature detection in the  $^{15}\text{N}$  dimension is achieved by incrementing  $\phi_1$  in the usual States-TPPI manner. The INEPT delay  $\tau_{\text{INEPT}}$  is 2.7 ms. The delay  $\delta$  for the build up of the RDCs and the refocusing of the joint coherence on both NH groups is 30 ms. The  $\Delta$  duration is set to 0 ms (for the reference experiment) or 5.4 ms (for the CCR evolving experiment), while the CCR evolution time  $\tau$  is 50 ms. The relaxation delay is 1.0 s. Phase cycling:  $\phi_1 = x, -x$ ;  $\phi_2 = 2(x), 2(-x)$ ;  $\phi_3 = 4(y), 4(-y)$ ;  $\phi_4 = 8(y), 8(-y)$ ;  $\phi_{27} = 4(-y), 4(y)$ ;  $\phi_{28} = 8(-y), 8(y)$ ;  $\phi_{\text{receiver}} = (-x, x, x, -x), 2(x, -x, -x, x), (-x, x, x, -x)$ . All gradients are sine shaped, with a duration of  $G_{1,2,3,4,5} = 500, 500, 500, 500, 500 \mu\text{s}$ . The measurement was run with  $(t_1 = 1024) \times (t_2 = 60) \times (t_3 = 60)$  complex points. The measurement was conducted on a 900 MHz spectrometer equipped with a TCI cryo-probe head.

A 3-dimensional  $^{15}\text{N}$ ,  $^{15}\text{N}$ ,  $^1\text{H}$  experiment was developed to measure the NH - NH CCR rates in the  $\beta$ -Sheet. The pulse sequence scheme is shown in figure 3.9. The experiment starts with building up antiphase magnetization from the  $^1\text{H}$  to the  $^{15}\text{N}$  of the first  $\beta$ -strand followed by converting the magnetization into multiquantum coherence (point a:  $H_x^1 N_y^1$ ). Afterwards in a constant time block, the chemical shift of the nitrogen is probed in the incremented time  $t_1$ ; In parallel in the delay  $\delta$ , the residual dipolar coupling is evolving between the proton of the first  $\beta$ -strand to a proton of the second  $\beta$ -strand. At the end of the constant time period, the joint coherences on the  $\beta$ -strands are present (point b:  $H_x^1 N_y^1 H_z^2$ ). The following INEPT step refocuses and defocuses the inphase and antiphase

operators on both  $\beta$ -strands, which leads to the coherence  $N_y^1 H_z^2 N_y^2$  at the start of the CCR evolution block (point c). The cross correlated relaxation is evolving the coherence  $N_y^1 H_z^2 N_y^2 \rightarrow N_y^1 H_z^2 N_y^2 \cdot \cosh(-\Gamma \cdot \tau) + H_z^1 N_x^1 N_x^2 \cdot \sinh(-\Gamma \cdot \tau)$  (point d). The second operator leads to the desired magnetization, which is converted again to  $H_z^1 N_y^2 H_y^2$  by another INEPT step (point e). The second constant time block probes the nitrogen chemical shift on the second  $\beta$ -strand in the incremented time  $t_2$  and allows the residual dipolar coupling to refocus the antiphase operator between the two protons in the delay  $\delta$  (point f:  $N_x^2 H_x^2$ ). The last INEPT step refocuses the antiphase magnetization on the second amide group and finishes with detection on the proton.

### The $\beta$ -Strand $C^1\alpha H^1\alpha - C^2\alpha H^2\alpha$ CCR Experiment

The wild-type  $^{13}\text{C}$ -labeled human ubiquitin expressed according to a previous protocol by Johnson et al. [90] was kindly provided by Dr. Stefan Becker and Karin Giller. 13.4 mg ubiquitin were dissolved in 300  $\mu\text{L}$  phosphate buffer (50 mM  $\text{NaPO}_4$ , 100 mM NaCl, pH = 6.8, 0.1 % (w/v)  $\text{NaN}_3$ , 10 % (v/v) D2O). The measurements were conducted at a temperature of 277 K.

For the measurement of the  $C^1\alpha H^1\alpha - C^2\alpha H^2\alpha$  CCR rates between  $\beta$ -strands, a 2-dimensional  $^{13}\text{C}, ^1\text{H}$  experiment was created. The restriction to only two dimensions shortens the experiment time and increases the sensitivity, but it lowers the dispersion of the signals and makes it more difficult to identify the cross peaks from successful transfers between the  $\beta$ -strands. The scheme of the pulse sequence is shown in figure 3.10.

After an initial INEPT transfer the carbon chemical shift of the first  $C_\alpha$  was probed. The following first RACT step transfers the magnetization from  $H_y^1 C_z^1$  (point a) to  $H_y^1 H_z^2$  (point b). Another INEPT step converts the magnetization to  $H_y^1 H_x^2 C_z^2$  at the start of the CCR evolution block (point c). The CCR evolution time turns the magnetization from  $H_y^1 H_x^2 C_z^2$  to  $H_y^1 H_x^2 C_z^2 \cdot \cosh(-\Gamma \cdot \tau) + H_x^1 C_z^1 H_y^2 \cdot \sinh(-\Gamma \cdot \tau)$  (point d). The inphase and antiphase operator of the desired second term,  $H_x^1 C_z^1 H_y^2$ , are afterwards refocused and defocused in another INEPT step to  $H_z^1 H_y^2$  (point e). The magnetization is refocused on the proton of the second  $\beta$ -strand by a second RACT step and is detected.

### The $\beta$ -Strand $C^{1/2}\alpha H^{1/2}\alpha - H^1\alpha H^2\alpha$ CCR Experiment

Starting from the previous  $C\alpha H\alpha - C\alpha H\alpha$   $\beta$ -Sheet experiment a second shorter variant was created similar to Bouisbouvier et al. [63], which can be used to measure the CCR rates of  $C^1\alpha H^1\alpha - H^1\alpha H^2\alpha$  and  $C^2\alpha H^2\alpha - H^1\alpha H^2\alpha$ . The idea is that since the through space transfer is achieved by the cross-correlated relaxation effect the transfer efficiency



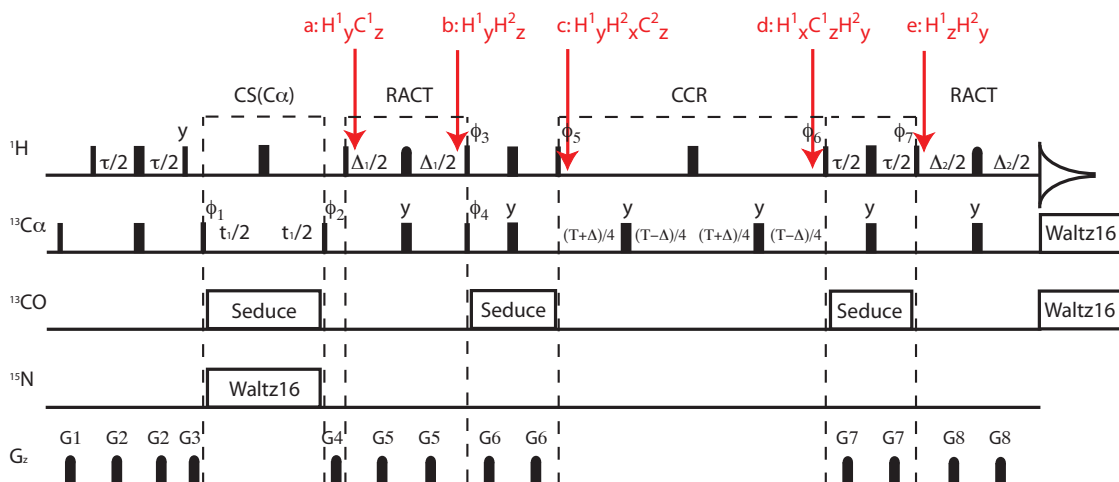


**Figure 3.10:** Pulse scheme for  $C\alpha H\alpha - C\alpha H\alpha$  CCR rate measurement. Two-dimensional  $^{13}C - \{^1H\} \rightarrow ^1H - \{^{13}C\}$  transfer scheme, where the  $\{\}$  brackets mark the undetected nuclei involved in the cross-correlation relaxation process. Narrow and wide pulses correspond to flip angles of  $90^\circ$  and  $180^\circ$ , respectively. Unless indicated otherwise, all radio-frequency pulses are applied with phase x. The  $^{13}C$  decoupling during detection is achieved by a waltz16 decoupling sequence. The selective  $^{13}CO$  decoupling sequence is of the SEDUCE type, while the  $^{15}N$  decoupling is conducted by a waltz16 sequence. The shaped  $^1H$  pulses are of the  $180^\circ$  REBURP type (2700 ms length at 900 MHz). Quadrature detection in the  $^{13}C$  dimension is achieved by incrementing  $\phi_1$  in the usual States-TPPI manner. The  $\Delta_1$  and  $\Delta_2$  durations are set to  $n/{}^1J_{CH}$  and  $m/{}^1J_{CH}$  (with  $n$  and  $m$  as integer numbers). The relaxation delay is 1.0 s, the INEPT delay  $\tau$  is 1.7 ms, the CCR evolution delay  $T$  is 10 ms and  $\Delta$  is either set to 0 ms for the reference experiment or 3.4 ms for the CCR evolving experiment. Phase cycling:  $\phi_1 = x, -x$ ;  $\phi_2 = 2(x), 2(-x)$ ;  $\phi_3 = 8(x), 8(-x)$ ;  $\phi_4 = 4(y), 4(-y)$ ;  $\phi_5 = 16(x), 16(-x)$ ;  $\phi_6 = 32(x), 32(-x)$ ;  $\phi_7 = 64(x), 64(-x)$ ;  $\phi_{receiver} = 2(x, -x, -x, x), (-x, x, x, -x)$ . All gradients are sine shaped, with a duration of  $G_{1,2,3,4,5,6,7,8} = 1000, 700, 200, 300, 500, 600, 500, 500 \mu s$ . The measurement was run with  $(t_1 = 90) \times (t_2 = 1024)$  complex points

directly depends on the CCR rates. Therefore the CCR evolution block of the  $C\alpha H\alpha - C\alpha H\alpha$   $\beta$ -Sheet experiment could be removed and instead the CCR rates could be determined from the transfer efficiencies. The pulse sequence scheme is shown in figure 3.11. This modification has the advantage that the experiment is shortened by the length of the CCR evolution block.

Up to the end of the first RACT step (point a) the magnetization transfer is the same as in the  $C^1\alpha H^1\alpha - C^2\alpha H^2\alpha$  CCR experiment. Directly following the first RACT block, another RACT step refocus the magnetization from  $H_z^1 H_y^2$  (point b) to  $H_y^2 C_z^2$  (point c). In the final INEPT step, the magnetization is refocused on the proton of the second  $\beta$ -strand and then

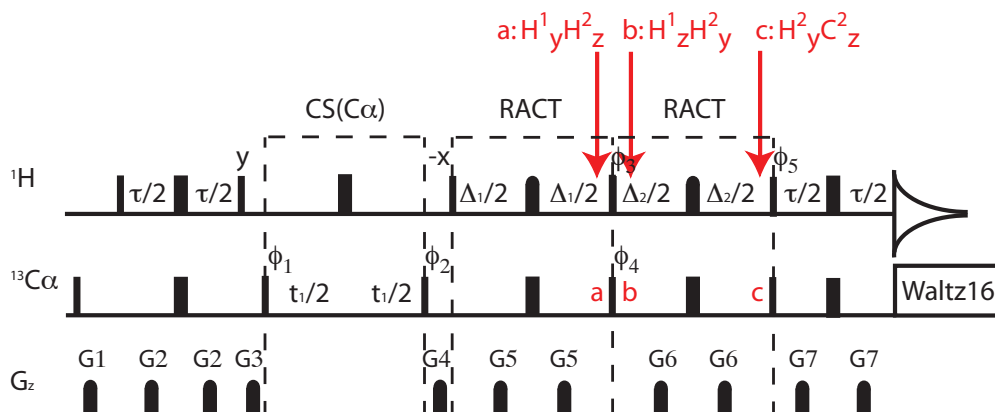


**Figure 3.11:** Pulse scheme for transfer amplitude modulated  $C\alpha H\alpha - C\alpha H\alpha$  CCR rate measurement. Two-dimensional  $^{13}C - \{^1H\} \rightarrow ^1H - \{^{13}C\}$  transfer scheme, where the  $\{\}$  brackets mark the undetected nuclei involved in the cross-correlation relaxation process. Narrow and wide pulses correspond to flip angles of  $90^\circ$  and  $180^\circ$ , respectively. Unless indicated otherwise, all radio-frequency pulses are applied with phase x. The  $^{13}C$  decoupling is achieved by a waltz16 decoupling sequence. The shaped  $^1H$  pulses are of the  $180^\circ$  REBURP type (2700 ms length at 700 MHz). Quadrature detection in the  $^{13}C$  dimension is achieved by incrementing  $\phi_1$  in the usual States-TPPI manner. The  $\Delta_1$  and  $\Delta_2$  durations are set to  $n/{}^1J_{CH}$  and  $m/{}^1J_{CH}$  (with  $n$  and  $m$  as integer numbers). The relaxation delay is 1.0 s and the INPET delay  $\tau$  is 1.7 set to ms. Phase cycling:  $\phi_1 = x, -x$ ;  $\phi_2 = 2(x), 2(-x)$ ;  $\phi_3 = 16(x), 16(-x)$ ;  $\phi_4 = 8(x), 8(-x)$ ;  $\phi_5 = 4(y), 4(-y)$ ;  $\phi_{receiver} = -x, x, x, -x$ . All gradients are sine shaped, with a duration of  $G_{1,2,3,4,5,6,7} = 1000, 1000, 800, 1000, 1000, 1000, 1000$   $\mu s$ . The measurement was run with  $(t_1 = 90) \times (t_2 = 512)$  complex points

detected.

### 3.4.2 Results and Discussion

The basic problem of the NH-NH experiment is the need for a strong anisotropic alignment medium for the sample. The calculation of the residual dipolar couplings between the amide protons of opposing  $\beta$ -strands predicts couplings in a range of 0 to 10 Hz, depending on the orientation of the specific NH bonds in the alignment media. Starting from these predicted RDCs the transfer delay was optimized experimentally to a value of 30 ms. Due to the different alignment tensors, the use of two different anisotropic media results in two unique sets of RDCs per each residue. Therefore a cross  $\beta$ -sheet transfer could be more efficient for a residue in one medium than in the other medium.

From these measurements, only five potential cross peaks could be identified (residue 3 to 15, 5 - 13, 4 - 65, 42 - 70 and 45 - 48). Unfortunately the intensities of the cross peaks are in a signal to noise range of 1 to 3 and therefore not large enough to separate the weak CCR interactions from other influences. This situation is direct result of the anisotropic media due to two reasons. First, the media causes problems with the homogeneity of the sample. The inhomogeneity results in additional peak broadening, reducing the signal to noise ratio. The reduction in signal to noise leads to a stronger overlap of signals, making it more difficult to identify potential cross peaks between amide groups from two  $\beta$ -strands. In addition, from the induced dipolar couplings between the active and the surrounding nuclei, especially the protons, increases significantly the relaxation.

Due to the strong overlap in the 2-dimensional spectra of both  $C\alpha H\alpha$  -  $H\alpha H\alpha$  experiments, only four cross peaks of successful transfers between two  $\beta$ -strands could be identified (from residue 14 to residue 4, from 12 to 6, from 43 to 69 and 69 to 43). These peaks are shown in figure 3.12. The  $C\alpha H\alpha$  -  $H\alpha H\alpha$  CCR rates for these three residue pairs were backcalculated from five ensembles (pdb code: 1d3z [109], pdb code: 2nr2 [83], pdb code: 1xqq [84], pdb code: 2kox [42], pdb code: 2k39 [37]). The averages of the backcalculated CCR rates for the six transfers between these three residue pairs are shown in table 3.1.

**Table 3.1:** Average  $C\alpha H\alpha$  -  $H\alpha H\alpha$  CCR rates backcalculated from five structure ensembles

Atom Pairs	CCR rate [Hz]
$C\alpha(44)H\alpha(44)$ - $H\alpha(44)H\alpha(70)$	3.2
$C\alpha(70)H\alpha(70)$ - $H\alpha(44)H\alpha(70)$	3.0
$C\alpha(13)H\alpha(13)$ - $H\alpha(13)H\alpha(7)$	6.8
$C\alpha(7)H\alpha(7)$ - $H\alpha(13)H\alpha(7)$	6.6
$C\alpha(5)H\alpha(5)$ - $H\alpha(5)H\alpha(15)$	4.9
$C\alpha(15)H\alpha(15)$ - $H\alpha(5)H\alpha(15)$	4.5

The differences of the two CCR rates for a residue pair is based on the different angles of the  $H\alpha H\alpha$  to the two  $C\alpha H\alpha$  vectors. The calculated transfer efficiencies based on these rates with the measured transfer delay (3.5 ms, 7 ms, 10.5 ms and 14 ms) are very small. Nevertheless, the experimentally measured cross peak intensities show that the transfer amplitude optimal delay is shorter than 14 ms. the short optimal transfer delays probably results from couplings to other protons, especially the  $H\beta$ s, and dipolar interactions due to the protonated side chains.

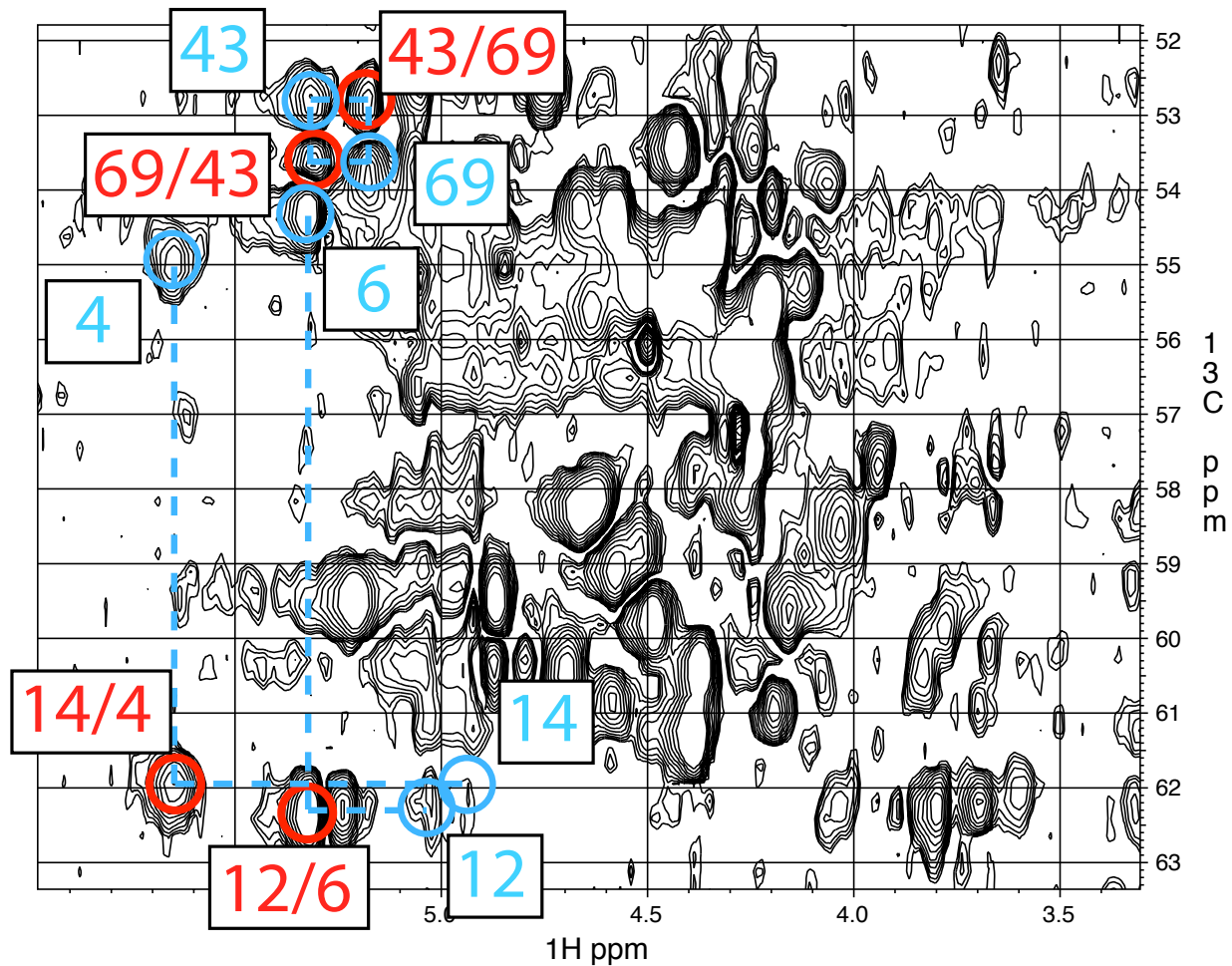


**Figure 3.12:** A section of the spectrum of the  $\beta$ -Strand  $C^\alpha H^\alpha - H^1 \alpha H^2 \alpha$  CCR measurement. The measurement was conducted on a 700 MHz spectrometer equipped with a QCI cryo-probe head. The blue circles mark the peaks of the magnetization which does not transfer and stays on the first residue. The red circles mark the cross peaks from a magnetization transfer between residues of separate  $\beta$ -strands.

Unfortunately the intensities of the four peaks in the  $C\alpha H\alpha - C\alpha H\alpha$  experiment are only slightly above the range of the noise level and therefore not useable for a serious determination of the CCR rates.

The second CH - HH CCR experiment achieves higher sensitivity, however, at the expense of introducing several additional problems compared to the CH - CH CCR experiment. The first disadvantage is that the H-H distances are not fixed like the C-H distances. Since the cube of the distance is inversely proportional to the size of the CCR rate, inaccuracies in the determination of the distances can lead to significant errors in the calculation of the CCR rates. The second point is that the intensity of the cross peak depends on two transfer efficiencies on the basis of two separate CCR rates,  $C^1\alpha H^1\alpha - H^1\alpha H^2\alpha$  and  $C^2\alpha H^2\alpha - H^1\alpha H^2\alpha$ . This fact makes the separation of the two rates from the intensity less accurate. The third and most important disadvantage is that for this kind of experiment no reference measurement can be conducted in which no evolution of the cross-correlated relaxation occurs. Therefore there is no easy way to cancel out the other relaxation effects. Therefore the overall transfer efficiency depends on the following relation.

$$I \propto \sinh(-\Gamma^1\Delta^1) \cdot \exp(-R_2^1\Delta^1) \cdot \sinh(-\Gamma^2\Delta^2) \cdot \exp(-R_2^2\Delta^2), \quad (3.32)$$

with the CCR rates  $\Gamma^1$  and the corresponding transverse relaxation rate  $R_2^1$  of the  $C^1\alpha H^1\alpha - H^1\alpha H^2\alpha$  CCR transfer in the delay  $\Delta^1$ ,  $\Gamma^2$  and the corresponding transverse relaxation rate  $R_2^2$  of the  $C^2\alpha H^2\alpha - H^1\alpha H^2\alpha$  CCR transfer in the delay  $\Delta^2$ . By measuring the intensities for different combinations of incremented  $\Delta^1$  and  $\Delta^2$  delays it should be possible to use a fitting procedure with the  $\Gamma$  and  $R_2$  values as variables to extract the CCR rates.

The relative intensities for the four cross peaks in the  $C^a\alpha H^a\alpha - H^1\alpha H^2\alpha$  CCR experiment for all 16 measured delay increment combinations for  $\Delta^1$  and  $\Delta^2$  are shown in the appendix. The signal to noise ratio of these signal were in a range of 5 to 10 for the spectra with short  $\Delta^1$  and  $\Delta^2$  delays, but decrease to 1 to 5 with longer  $\Delta^1$  and  $\Delta^2$  delays. A fitting procedure was applied to these values, but the procedure was not able to achieve reasonable  $\Gamma$  and  $R_2$  values. The reason for this failure are probably the weaker and therefore less accurate intensities of the longer incremented transfer delays.

### 3.5 Long-Range Correlated Motions

While the CCR rates between groups in the  $\beta$ -sheet could deliver information about correlated motions in the secondary structure of the protein, global correlated motions of the tertiary structure are also of strong interest. The methyl groups of the side chains could work as very useful probes to detect correlated motions in the hydrophobic core. For example, the measurement of CCR rates between the methyl groups of LEU15, ILE13 and VAL5 on the second  $\beta$ -strand with respect to the loop between the two first  $\beta$ -strands and the methyl groups of ILE 30 and ILE 36 on the  $\alpha$ -helix could be an independent verification of the strong pincer mode, which the EROS ensemble shows [37]. Therefore two experiments

were created to measure the CH-CH CCR rates between two methyl groups. The first experiment uses the NOE effect for the through the space magnetization transfer between the two methyl groups, while the second experiment use two RACT transfer steps to detect the CCR rates via the transfer amplitude.

### 3.5.1 Material and Methods

#### The Inter Methyl NOE Experiment

The used wild-type human ubiquitin was  $^{15}\text{N}$ ,  $^{13}\text{C}$ -labeled, while all hydrogen positions aside from the methyl groups of isoleucine, leucine and valine were deuterated according to Goto et al. [114]. It was kindly provided by Dr. Stefan Becker and Karin Giller. 12.5 mg ubiquitin were dissolved in 350  $\mu\text{L}$  phosphate buffer (50 mM  $\text{NaPO}_4$ , 100 mM  $\text{NaCl}$ ,  $\text{pH} = 6.5$ , 0.1 % (w/v)  $\text{NaN}_3$ , 100 % (v/v)  $\text{D}_2\text{O}$ ). The measurements were conducted at a temperature of 308 K.

For the measurement of the methyl-methyl CCR rates a new 3-dimensional  $^{13}\text{C}$ ,  $^{13}\text{C}$ ,  $^1\text{H}$  experiment with two NOE transfer steps and one CCR evolution block was developed. The pulse sequence starts with an INEPT magnetization transfer from the methyl protons to the carbon, where subsequently the chemical shift of the carbon of the first methyl group is probed in the first incremented time. Afterwards the antiphase magnetization is brought back to the z axis (point a:  $H_z^1 C_z^1$ ) and the first NOE step transfers proton magnetization from the first methyl group to the second one (point b:  $C_z^1 H_z^2$ ). Afterwards an INEPT step evolves the CH coupling on the second methyl group and brings the magnetization on the protons to the z axis, while the magnetization on the carbons is in the transverse plain (point c:  $C_y^1 H_z^2 C_y^2$ ). In the following building block the cross correlated relaxation of this magnetization can evolve (up to point d):

$$C_y^1 H_z^2 C_y^2 \rightarrow C_y^1 H_z^1 C_y^2 \cdot \cosh(-\Gamma \cdot \tau) + H_z^1 C_x^1 C_x^2 \cdot \sinh(-\Gamma \cdot \tau)$$

The first term  $C_y^1 H_z^2 C_y^2$  will lead to the diagonal peak, where both indirect carbon dimensions probe the carbon of the first residue, while the second term  $H_z^1 C_x^1 C_x^2$  lead to the cross peak, which will probe in the second indirect dimension the chemical shift of the carbon of the second residue as shown in the following. For this coherence the next INEPT refocus the magnetization on the proton of the first residue (point e:  $H_z^1 C_z^2$ ), before the second NOE transfer refocuses the magnetization to the second methyl group (point f:  $H_z^2 C_z^2$ ). Subsequently the second incremented delay probes the carbon chemical shift of the second residue and a final INEPT step leads to the detection on the methyl proton of the second residue.

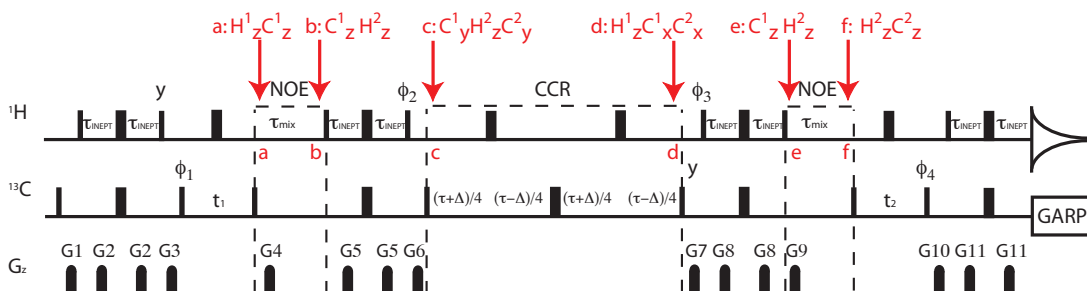


**Figure 3.13:** Pulse scheme for the inter methyl CH - inter methyl CH CCR rate measurement. Three-dimensional  $^{13}\text{C} - \{^1\text{H}\} \rightarrow ^1\text{H} - ^{13}\text{C}$  transfer scheme, where the  $\{\}$  brackets mark the undetected nuclei involved in the cross-correlation relaxation process. Narrow and wide pulses correspond to flip angles of  $90^\circ$  and  $180^\circ$ , respectively. Unless indicated otherwise, all radio-frequency pulses are applied with phase x. Quadrature detection in the  $^{13}\text{C}$  dimension is achieved by incrementing  $\phi_1$  in the usual States-TPPI manner. The mixing time  $\tau_{mix}$  is optimal at 600 ms. The relaxation delay is set to 1.0 s, the INEPT transfer delay is  $\tau_{INEPT} = 2$  ms and the CCR evolving time is  $\tau = 25$  ms. The  $\Delta$  duration is set to 0 ms (for the reference experiment) or 1 ms (for the CCR evolving experiment). Phase cycling:  $\phi_1 = x, -x$ ;  $\phi_2 = 8(y), 8(-y)$ ;  $\phi_3 = 4(y), 4(-y)$ ;  $\phi_4 = 2(x), 2(-x)$ ;  $\phi_{receiver} = (-x, x, x, -x), 2(x, -x, -x, x), (-x, x, x, -x)$ . All gradients are sine shaped, with a duration of  $G_{1,2,3,4,5,6,7,8,9,10,11} = 1000, 500, 1000, 800, 500, 800, 1000, 1000, 500, 500, 500 \mu\text{s}$ . The measurement was run with  $(t_1 = 1024) \times (t_2 = 60) \times (t_3 = 90)$  complex points. The measurement was conducted on a 900 MHz spectrometer equipped with a TCI cryo-probe head.

In the case of the methyl group, the effective internuclear vector of the cross-correlated dipole-dipole relaxation process is not aligned with one of the three CH vectors, but is averaged about all of their positions due to the fast rotation of the methyl group. Therefore the effective vector is pointing along the  $C - C_{methyl}$  axis.

As shown in the theory section (figure 3.2) all CSA - dipole-dipole and CSA - CSA interactions are not contributing to the measured CCR rates. Therefore only the intra methyl  $dd(C^1H_a^1) - dd(C^1H_b^1)$  and the long range inter methyl  $dd(C^1H^1) - dd(C^2H^2)$  interactions contribute to the measured CCR rates. To separate the first from the latter the intra methyl CCR rate were measured by a simple HSQC experiment without proton decoupling in the indirect dimension as shown in figure 3.14. In this way it was possible to determine the intra methyl CCR rates of 22 methyl groups. The signal to noise of such an experiment run for around 1 h, was in the range of 50 to 100.

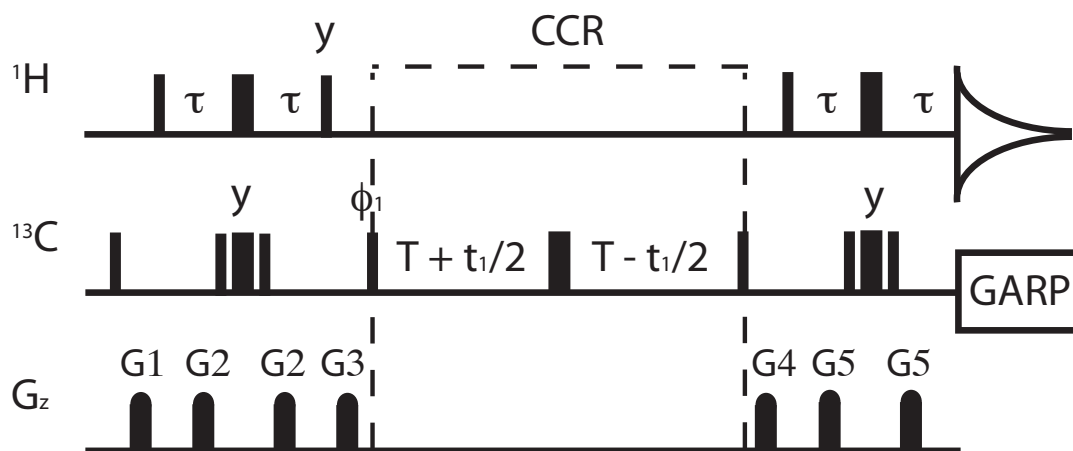


**Figure 3.14:** Pulse scheme for the intra methyl CH - intra methyl CH CCR rate measurement. Two-dimensional  $^{13}\text{C}$  -  $^1\text{H}$  transfer scheme, where the  $\{ \}$  brackets mark the undetected nuclei involved in the cross-correlation relaxation process. Narrow and wide pulses correspond to flip angles of  $90^\circ$  and  $180^\circ$ , respectively. Unless indicated otherwise, all radio-frequency pulses are applied with phase x. Quadrature detection in the  $^{13}\text{C}$  dimension is achieved by incrementing  $\phi_1$  in the usual States-TPPI manner. The delay  $T$  is set to 27.8 ms. The relaxation delay is 1.0 s. Phase cycling:  $\phi_1 = x, -x$ ;  $\phi_{\text{receiver}} = x, -x$ . All gradients are sine shaped, with a duration of  $G_{1,2,3,4,5} = 1000, 500, 500, 1000, 500$  ms. The measurements were run with  $(t_1 = 1024) \times (t_2 = 256)$  complex points on a 700 MHz spectrometer equipped with a TCI cryo-probe head and with  $(t_1 = 2048) \times (t_2 = 256)$  complex points on a 700 MHz spectrometer equipped with a I cryo-probe head.

### The Inter Methyl RACT Experiment

With the measured gains in sensitivity for the  $C\alpha H\alpha - C\alpha H\alpha$  CCR experiment by using a RACT-transfer amplitude modulated CCR rate measurement, this concept was then applied for a second inter methyl CCR experiment.

The experiment is a 2-dimensional  $^{13}\text{C}, ^1\text{H}$  experiment with two RACT transfer steps. After starting with an INEPT transfer from the methyl protons to the carbons, the chemical shift of the carbons of the first residue is probed during  $t_1$ . Next the first RACT step transfers the magnetization from  $H_y^1 C_z^1$  (point a) to  $H_y^1 H_z^2$  (point a) by the cross correlated relaxation between the  $C^1 H^1$  and  $H^1 H^2$  dipole-dipole interactions. Finally, the second RACT step refocuses the magnetization on the second residue from  $H_z^1 H_y^2$  (point c) to  $H_y^2 C_z^2$  (point d) by evolution of the cross correlated relaxation between the  $C^2 H^2$  and  $H^1 H^2$  dipole-dipole interactions.



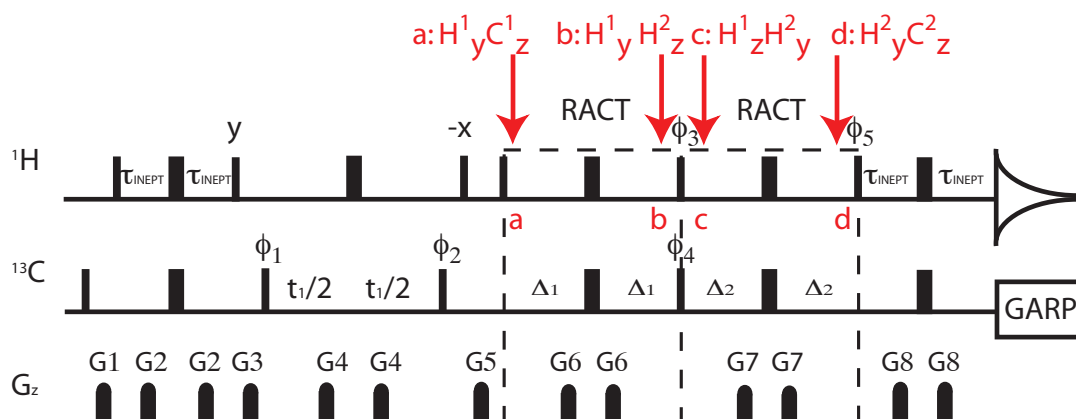


**Figure 3.15:** Pulse scheme for the RACT transfer amplitude modulated inter methyl CH - inter methyl CH CCR rate measurement. Two-dimensional  $^{13}\text{C} - \{^1\text{H}\} \rightarrow ^1\text{H} - ^{13}\text{C}$  transfer scheme, where the  $\{\}$  brackets mark the undetected nuclei involved in the cross-correlation relaxation process. Narrow and wide pulses correspond to flip angles of  $90^\circ$  and  $180^\circ$ , respectively. Unless indicated otherwise, all radio-frequency pulses are applied with phase x. Quadrature detection in the  $^{13}\text{C}$  dimension is achieved by incrementing  $\phi_1$  in the usual States-TPPI manner. The relaxation delay is set to 1.0 s and the INEPT transfer delay is  $\tau_{\text{INEPT}} = 1.7$ . The delays for the first transfer  $\Delta_1$  and for the second transfer  $\Delta_2$  are set to  $n/{}^1J_{\text{CH}}$  and  $m/{}^1J_{\text{CH}}$  (with  $n$  and  $m$  are integer number) Phase cycling:  $\phi_1 = x, -x$ ;  $\phi_2 = 2(x), 2(-x)$ ;  $\phi_3 = 16(x), 16(-x)$ ;  $\phi_4 = 8(x), 8(-x)$ ;  $\phi_5 = 4(y), 4(-y)$ ;  $\phi_{\text{receiver}} = -x, x, x, -x$ . All gradients are sine shaped, with a duration of  $G_{1,2,3,4,5,6} = 1000, 1000, 800, 1000, 1000, 1000 \mu\text{s}$ . The measurement was run with  $(t_1 = 1024) \times (t_2 = 120)$  complex points. The measurement was conducted on a 900 MHz spectrometer equipped with a TCI cryo-probe head.

The development of the methyl experiment was conducted together with Dr. T. Michael Sabo, who also performed the evaluation of the spectra.

### 3.5.2 Results and Discussion

The NOE transfer in the inter methyl experiment is not efficient enough to achieve inter methyl cross peaks with sufficient sensitivity. Even in an experiment run for 5 days, the cross peaks of the possible transfers were still in the noise level. The experimentally measured intra methyl CCR rates of 22 residues can not deliver any information about correlated motions by themselves, but could be used for the determination of motional amplitudes of the C-C bond prior to the methyl group.

In the spectrum of the RACT transfer amplitude modulated inter methyl experiment two cross peaks between methyl groups were identified. The signal to noise ratio of these peaks are 5 and 2.5. However they are only between the two methyl groups of the same residue, Valine 17, and therefore can't offer any information about long range correlated motions. Nevertheless they show that the general idea of the experiment works, even if the two methyl groups of the valine are much closer to each other than most of the methyl groups from separate side chains.

### 3.6 Summary and Outlook

The understanding of the dynamical aspects of the structure of a protein is essential for the understanding of its functional processes. There are several well established NMR methods to determine motional amplitudes on an atomic resolution for several different time windows. Nevertheless other aspects of the protein dynamics are less well investigated. Recent structural ensembles predict strong correlated motional modes for the transfer from one structural binding conformer to a second one. Therefore experimental methods to validate such predictions and measure experimentally correlated motions would be of great interest. For NMR spectroscopy cross-correlated relaxation rates are the most useful parameter to measure correlated motions between atom groups, since their size depends directly on the angle between two internuclear vectors. Especially experiments for the measurement of CCR rates between nuclei from different sites of the protein could offer extremely valuable information about global protein dynamics.

Using NH - NH and  $NH - C_\alpha H_\alpha$  cross-correlated relaxation rates in the backbone of the protein ubiquitin, the prediction of such rates by several structural ensembles were validated. By this approach it was possible to show that only ensembles with a precise description of the orientation of the involved nuclei can reproduce the experimental CCR rates. This finding points out how important residual dipolar couplings for the correct description of dynamics in the creation process of structural ensembles, not only for the determination of the dynamical amplitudes, but also for the precise determination of the orientation of the internuclear vector involved.

Even if in principal it is possible to detect the whole correlated motion only by intraresidual  $NH - C_\alpha H_\alpha$  CCR rates and the NH - NH CCR rates between sequential residues, this is not a reliable way to determine long range correlated motions due to the error propagation from measurements of each residue. Therefore the measurement of CCR rates between atom groups in separated parts of the protein would be of special interest.

For the measurement of cross-correlated relaxation rates between distant sites of the protein, three experimental approaches based on transfers by cross-relaxation, residual dipolar couplings and cross-correlated relaxation have been investigated. For each of the approaches pulse sequences have been developed, tested and optimized.

Unfortunately the goal to measure CCR rates between distant atom pairs with a sufficient sensitivity for a reliable determination of correlated protein dynamics has yet to be successful. Nevertheless some of the developed experiments show promising results. The principal problem of all these long range experiments is the low sensitivity due to the need of two through space transfer steps for the magnetization, using quite weak dipole - dipole interactions. Our experiments show that the most promising transfer approach is based on the cross-correlated relaxation RACT process. The approaches which use the transfer efficiency for the detection of the CCR rates show a sensitivity enhancement of a factor of two to four compared with similar implementations which use a separate block for the detection of the CCR rates. Even if it seems to be the best way to overcome the sensitivity issues, this kind of experiment has additional problems. The most important downside of the transfer efficiency based experiments lies in the more complex interpretation of the measured transferred magnetizations. The only way to extract the pure CCR rate without the contribution of transverse autorelaxation is the measurement of the changing intensity by varying the transfer time delays and fitting the theoretical dependencies of the two kinds of relaxation to these curves. This requirement makes a series of experiments necessary, while the sensitivity of the longer transfer delays become much weaker.

If in the future, the general technical based detection sensitivity increases, the developed experiments can come into a signal to noise range which makes a reliable calculation of the CCR rates possible.

Another alternative for the methyl measurements is to use a alternately labeled protein sample. Until now a sample was used which is fully deuterated at the side chains only the methyl hydrogens of valine, leucine and isoleucine are protonated. This scheme reduces the number of potential proton - proton dipolar interactions which are the main contributors to the transverse relaxation rate. Nevertheless, the prochiral intraresidual proton-proton dipolar interactions still contribute strongly to the relaxation and limit the accessible sensitivity of the experiment. Therefore a new sample should be expressed accordingly to Gans et al. [115]. Using specifically methyl-labeled acetolactate or 2-hydroxy-2- $^{13}\text{C}$  methyl-3-oxo-4- $^2\text{H}_3$ butanoic acid a stereospecific isotopic labeling for the methyl groups of valine and leucine residues will be possible, which should reduce the transverse relaxation significantly and raise the sensitivity. In this way, perhaps it will be possible to overcome the sensitivity problems for the developed methyl experiments.



## Chapter 4

# Quantitative NOE Buildups as an Indicator for Protein Dynamic

### 4.1 Introduction

The measurement of the Nuclear Overhauser Effect (NOE) is one of the most important medium range NMR parameters (normally up to around 5 Å) for the determination of the secondary and tertiary structure of proteins. In addition to containing structural informations NOEs which result from cross relaxation provide insight into protein dynamics. Under the simplest assumption of isotropic molecular tumbling of the protein the cross-relaxation rates do not depend on the orientation of the internuclear vector to an external frame or another vector as the residual dipolar couplings described in chapter 2 or the cross-correlated relaxation rates in chapter 3, but on the distance between two nuclei. Due to the efficient through space magnetization transfer mechanism of the NOE it is relatively easy to obtain NOEs between separated sites of a protein. Therefore similar to the cross-correlated relaxation rates in chapter 2, NOEs between aliphatic protons of two side chains could deliver valuable information about the dynamical aspects of the  $\beta$ -strands or side chains within the hydrophobic core.

Recently it has been shown how quantitative NOEs can be used for the separation of the internal dynamics of the protein into fast dynamics ( $\tau_{int} \ll \tau_c$ ) and slow dynamics ( $\tau_{int} \gg \tau_c$ ) relative to the overall correlation time of the protein [64]. Nevertheless these quantitative NOEs were only measured between the amide protons of the backbone and can therefore deliver only restricted information about the global dynamics of the protein. The following study was performed with the goal to measure quantitative NOEs over the whole structure of the fully protonated protein ubiquitin, which is especially for the methyl groups with their low chemical shift dispersion a challenging task.

## 4.2 Theory

NOEs in a multi spin system need to be described with a full matrix approach which cannot be solved analytically. The main feature of such an approach, namely spin diffusion is however reproduced considering only three-spins. Therefore in the following, this theory is recapitulated following Vogeli et al. [64]:

The NOE based transfer depends on the longitudinal relaxation properties of the involved nuclei. In the following a system with three dipolar coupled  $\frac{1}{2}$  spins I, K and S is assumed. The direct cross-relaxation transfer is occurring from spin I to spin S, while the influence of spin K stands for the further magnetization transports to the surrounding proton network, the spin diffusion. Especially in a fully protonated protein the proton networks are of course much larger, what probably lead to strong spin diffusional effects.

The Solomon equation [62] for such a three spin system is given as

$$\frac{d}{dt} \begin{pmatrix} \Delta I_z(t) \\ \Delta K_z(t) \\ \Delta S_z(t) \end{pmatrix} = - \begin{pmatrix} \rho_I & \sigma_{IK} & \sigma_{IS} \\ \sigma_{IK} & \rho_K & \sigma_{KS} \\ \sigma_{IS} & \sigma_{KS} & \rho_S \end{pmatrix} \begin{pmatrix} \Delta I_z(0) \\ \Delta K_z(0) \\ \Delta S_z(0) \end{pmatrix} \quad (4.1)$$

with  $\rho_X$  being the auto-relaxation rate of nucleus X and  $\sigma_{XY}$  being the cross-relaxation rate between the nuclei X and Y. If the initial magnetization is on spin I and there is only one dipolar coupling between I and S ( $\sigma_{IK} = \sigma_{KS} = 0$ ) the changes of the magnetization for I and S are

$$\frac{\Delta I_z(t)}{\Delta I_z(0)} = \frac{1}{2} \left[ \left(1 - \frac{\rho_I - \rho_S}{\lambda_+ - \lambda_-}\right) e^{-\lambda_- t} - \left(1 + \frac{\rho_I - \rho_S}{\lambda_+ - \lambda_-}\right) e^{-\lambda_+ t} \right] \quad (4.2)$$

$$\frac{\Delta S_z(t)}{\Delta I_z(0)} = - \frac{\sigma_{IS}}{\lambda_+ - \lambda_-} [e^{-\lambda_- t} - e^{-\lambda_+ t}] \quad (4.3)$$

with

$$\lambda_{\pm} = \frac{\rho_I + \rho_S}{2} \pm \sqrt{\left(\frac{\rho_I - \rho_S}{2}\right)^2 \pm \sigma_{IS}^2} \quad (4.4)$$

The homonuclear cross-relaxation rate between to nuclei X and Y is given by

$$\sigma_{XY} = \left(\frac{\mu_0}{4\pi}\right)^2 \frac{\gamma_X^2 \gamma_Y^2 \hbar^2}{40\pi^2} \frac{1}{(r_{XY}^{rigid})^6} [J(0) - 6J(2\omega)]. \quad (4.5)$$

Here  $\gamma_X$  and  $\gamma_Y$  are the gyromagnetic ratios of X and Y,  $\mu_0$  is the permeability in vacuum,  $\hbar$

is the Planck's constant,  $r_{XY}^{rigid}$  is the internuclear distance in a hypothetically rigid structure and  $J(0)$  and  $J(2\omega)$  are the spectral densities for the difference ( $\omega_X - \omega_Y$ ) and the sum ( $\omega_X + \omega_Y$ ) of the Larmor frequencies of the nuclei under the assumption that they are equal for both nuclei. The spectral density  $J$  can be described simplified under the assumption of isotropic molecular tumbling as

$$J(\omega) = S_{XY,fast}^2 \frac{\tau_c}{1 + (\tau_c \omega)^2} + ((r_{XY}^{rigid})^6 \langle \frac{1}{r_{XY}^6} \rangle - S_{XY,fast}^2) \frac{\tau_{tot}}{1 + (\tau_{tot} \omega)^2} \quad (4.6)$$

with

$$\frac{1}{\tau_{tot}} = \frac{1}{\tau_c} + \frac{1}{\tau_{int}} \quad (4.7)$$

Here  $\frac{1}{\tau_c}$  is the rotational correlation time of the molecule (typically in the range of some ns for small proteins),  $\frac{1}{\tau_{int}}$  is the rotational correlation time for internal motion and  $\frac{1}{\tau_{tot}}$  is the total correlation time of the molecule. The angled brackets  $\langle \rangle$  denotes a dynamical averaging and  $S_{XY,fast}^2$  is an order parameter which describes fast internal motion ( $\tau_{int} \ll \tau_c$ ) and is defined as followed:

$$S_{XY,fast}^2 \equiv (r_{XY}^{rigid})^6 \frac{4\pi}{5} \sum_{q=-2}^2 \langle \frac{Y_{2q}(\theta_{XY}^{mol}, \phi_{XY}^{mol})}{r_{XY}^3} \rangle^2 \quad (4.8)$$

An order parameter over all time scales can be defined as the ratio of the experimentally measured cross relaxation rates divided by the cross relaxation rate calculated from a rigid protein structure.

$$S_{XY}^2 \equiv \frac{\sigma_{XY}^{exp}}{\sigma_{XY}^{rigid}} \quad (4.9)$$

For macromolecules at high magnetic fields it can be assumed that the spectral density  $J$  is negligible for all frequencies beside zero. Under this assumption and using equation 4.5 the order parameter can be written as

$$S_{XY}^2 = S_{XY,fast}^2 + ((r_{XY}^{rigid})^6 \langle \frac{1}{r_{XY}^6} \rangle - S_{XY,fast}^2) \frac{1}{1 + \frac{\tau_c}{\tau_{int}}} \quad (4.10)$$

For faster internal dynamics than the molecular tumbling ( $\tau_{int} \ll \tau_c$ ) equation 4.10 reduces to

$$S_{XY}^2 = S_{XY,fast}^2, \quad (4.11)$$

while for internal dynamics much slower than the rotational correlation time ( $\tau_{int} \gg \tau_c$ ) it results in

$$S_{XY}^2 = (r_{XY}^{rigid})^6 \langle \frac{1}{r_{XY}^6} \rangle. \quad (4.12)$$

More precise without the assumption of negligible spectral density  $J(2\omega)$  the order parameter is given as

$$S_{XY}^2 = S_{XY,fast}^2 + ((r_{XY}^{rigid})^6 \langle \frac{1}{r_{XY}^6} \rangle - S_{XY,fast}^2) \frac{1}{1 + \frac{\tau_c}{\tau_{int}}} - 6 \cdot [S_{XY,fast}^2 + ((r_{XY}^{rigid})^6 \langle \frac{1}{r_{XY}^6} \rangle - S_{XY,fast}^2) \frac{1 + (\tau_c \cdot 2\omega)^2}{(1 + \frac{\tau_c}{\tau_{int}})(1 + (\frac{1}{\tau_c} + \frac{1}{\tau_{int}}) \cdot 2\omega)^2}] \quad (4.13)$$

This equation is reduced for fast internal dynamics ( $\tau_{int} \ll \tau_c$ ) to

$$S_{XY}^2 = S_{XY,fast}^2 + ((r_{XY}^{rigid})^6 \langle \frac{1}{r_{XY}^6} \rangle - S_{XY,fast}^2) \frac{1}{1 + \frac{\tau_c}{\tau_{int}}} - 6 \cdot [S_{XY,fast}^2 \frac{\tau_c}{1 + (\tau_c \omega)^2} + ((r_{XY}^{rigid})^6 \langle \frac{1}{r_{XY}^6} \rangle - S_{XY,fast}^2) \frac{1 + (\tau_c \cdot 2\omega)^2}{(1 + \frac{\tau_c}{\tau_{int}})(1 + (\tau_{int} \cdot 2\omega)^2)}] \quad (4.14)$$

and for slow internal dynamics ( $\tau_{int} \gg \tau_c$ ) to

$$S_{XY}^2 = S_{XY,fast}^2 + ((r_{XY}^{rigid})^6 \langle \frac{1}{r_{XY}^6} \rangle - S_{XY,fast}^2) \frac{1}{1 + \frac{\tau_c}{\tau_{int}}} - 6 \cdot [S_{XY,fast}^2 \frac{\tau_c}{1 + (\tau_c \omega)^2} + ((r_{XY}^{rigid})^6 \langle \frac{1}{r_{XY}^6} \rangle - S_{XY,fast}^2)]. \quad (4.15)$$

The spectral frequency  $\omega$  of the nuclei is field dependent. Therefore, NOESY measurements at several different magnetic field strengths can be conducted to extract the NOE-based order parameter using equations 4.14 and 4.15.

Furthermore, according to equations 4.5 and 4.6 the cross-relaxation rate is given as

$$\sigma_{XY} = (\frac{\mu_0}{4\pi})^2 \frac{\gamma_X^2 \gamma_Y^2 \hbar^2}{40\pi^2} \frac{1}{(r_{XY}^{rigid})^6} \cdot (S_{XY,fast}^2 \tau_c + ((r_{XY}^{rigid})^6 \langle \frac{1}{r_{XY}^6} \rangle - S_{XY,fast}^2) \tau_{tot} - 6(S_{XY,fast}^2 \frac{\tau_c}{1 + (\tau_c 2\omega)^2} + ((r_{XY}^{rigid})^6 \langle \frac{1}{r_{XY}^6} \rangle - S_{XY,fast}^2) \frac{\tau_{tot}}{1 + (\tau_{tot} 2\omega)^2})) \quad (4.16)$$

The following example should illustrate the field dependency of the NOE transfer:

To calculate the expected cross-relaxation rate for different field strengths,  $S_{XY,fast}^2$  is assumed to be 0.9, what is a typical value for NH amide Lipari-Szabo order parameter  $S_{LS}^2$



which are calculated based on  $R_1$ ,  $R_2$  and hetero-NOEs and are therefore covering the motion faster than  $\tau_c$ . The factor  $(r_{XY}^{rigid})^6 \langle \frac{1}{r_{XY}^6} \rangle = S_{XY,slow}^2$  can be determined as the ratio of a RDC-based order parameter (covering all motion faster than some ms) and a Lipari-Szabo order parameter (covering all motion faster than some  $\tau_c$ ). A value of 0.8 is assumed as a typical RDC-based order parameter. Therefore the  $(r_{XY}^{rigid})^6 \langle \frac{1}{r_{XY}^6} \rangle = S_{RDC}^2 / S_{LS}^2 = 0.89$ .  $\tau_c$  is ca. 4 ns for ubiquitin, as  $\tau_{int}$  a value of 1 ns is assumed. Therefore,  $\tau_c$  is 0.8 ns according to equation 4.7. As the average distance of the two protons  $3 \text{ \AA}$  are assumed. Introduced into equation the cross-relaxation rate is

$$\begin{aligned} \sigma_{XY} = & \left(\frac{\mu_0}{4\pi}\right)^2 \frac{\gamma_X^2 \gamma_Y^2 \hbar^2}{40\pi^2} \frac{1}{(3\text{\AA})^6} \cdot (0.9 \cdot 4ns + (0.89 - 0.9)0.8ns \\ & - 6(0.9 \frac{4ns}{1 + (4ns \cdot 2\omega)^2} + (0.89 - 0.9) \frac{0.8ns}{1 + (0.8ns \cdot 2\omega)^2})) \end{aligned} \quad (4.17)$$

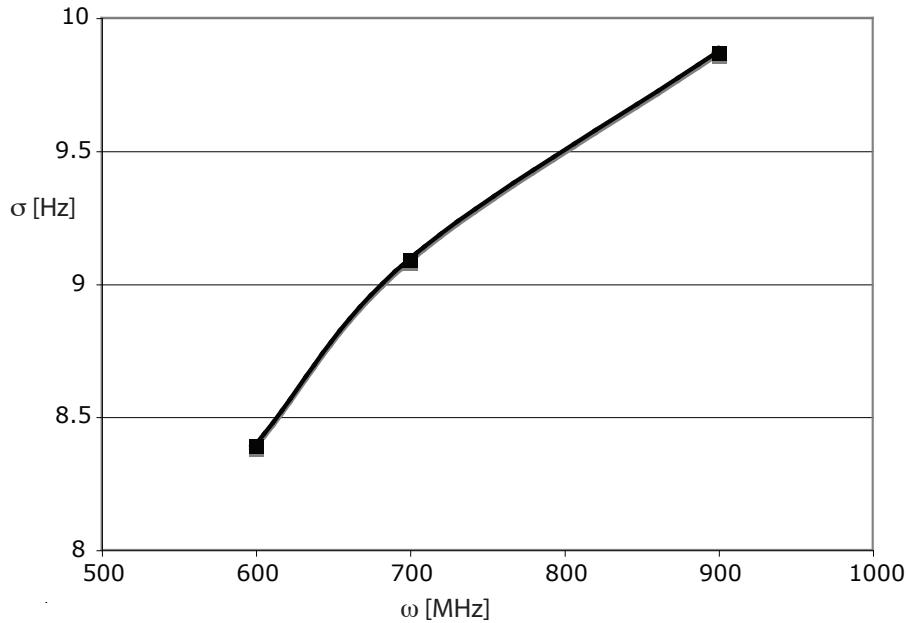


**Figure 4.1:** The graph shows the field dependency of the cross-relaxation rates according to equation 4.17 with  $S_{XY,fast}^2 = 0.9$ ,  $(r_{XY}^{rigid})^6 \langle \frac{1}{r_{XY}^6} \rangle = 0.89$ ,  $\tau_c = 4 \text{ ns}$ ,  $\tau_{int} = 1 \text{ ns}$  and  $r_{XY}^{rigid} = 3 \text{ \AA}$ .

The cross-relaxation rates calculated based on this equation for  $\omega = 600 \text{ MHz}$ ,  $700 \text{ MHz}$  and  $900 \text{ MHz}$  (for these frequencies measurements have been conducted) are shown in figure 4.1.

## 4.3 Material and Methods

### The Sample

The wild-type unlabeled human ubiquitin expressed according to a previous protocol by Johnson et al. [90] was kindly provided by Dr. Stefan Becker and Karin Giller. 10 mg ubiquitin were dissolved in 330  $\mu\text{L}$  50 mM sodium phosphate buffer with 100 mM NaCl at pH = 6.5, together with  $\text{NaN}_3$  0.1 % (w/v).

### NMR Spectroscopy

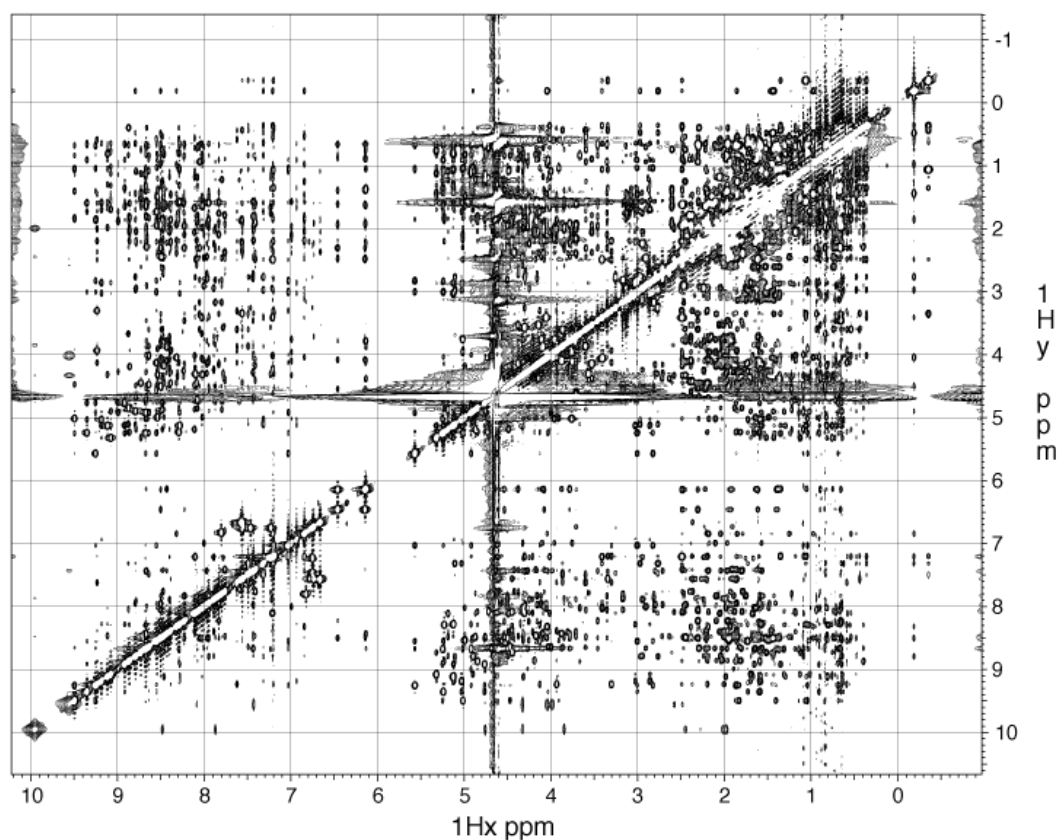


**Figure 4.2:** Representative  $^1\text{H}, ^1\text{H}$  NOESY spectrum of ubiquitin recorded on a Bruker 900 MHz spectrometer with CP-TXI cryo probe head. The mixing time was 100 ms.

The measurement of the NOE was conducted using a standard  $^1\text{H}, ^1\text{H}$  NOESY pulse sequence. The measurements were conducted at three field strengths, on a Bruker 900 MHz with a CP-TXI cryo probe head, a Bruker 700 MHz with a TCI cryo probe head and a

Bruker 600 MHz with a CP-QCI cryo probe head, with various values for the mixing delay as noted in table 4.1. The experiments were measured with  $300(t_1) \times 2048(t_2)$  complex points.

**Table 4.1:** The measured NOESY experiments listed according their field strengths and mixing times

Field strength	Mixing Time ( $\tau_{mix}$ )
600 MHz	10ms
600 MHz	15ms
600 MHz	25ms
600 MHz	50ms
600 MHz	75ms
600 MHz	100ms
600 MHz	150ms
600 MHz	200ms
600 MHz	250ms
600 MHz	300ms
600 MHz	350ms
700 MHz	10ms
700 MHz	50ms
700 MHz	75ms
700 MHz	100ms
700 MHz	150ms
700 MHz	200ms
700 MHz	250ms
700 MHz	300ms
700 MHz	350ms
900 MHz	10ms
900 MHz	25ms
900 MHz	50ms
900 MHz	75ms
900 MHz	100ms
900 MHz	150ms
900 MHz	200ms
900 MHz	250ms

For the assignment of the  $^1H$ ,  $^1H$  cross peaks  $^{15}N$ ,  $^1H$  HSQC,  $^{13}C$ ,  $^1H$  HSQC and  $^1H$ ,  $^1H$  TOCSY were conducted on a Bruker 700 MHz spectrometer with TCI cryo probe head. For the  $^1H$ ,  $^1H$  TOCSY the clean TOCSY mixing [116] was used with the MLEV16 sequence (80 ms). This spectrum is shown in figure 4.3.

The spectra were measured at a temperature of 308 K. To ensure comparability of the NOESY spectra, before each measurement a calibration with a separate temperature probe was conducted to match the temperature of 308 K across different spectrometers.

All spectra were processed with the program NMRPipe (F. Delaglio [106]). For the assignment and the determination of the peak intensities the program CARA (R. Keller and K. Wuthrich [107]) was used.

## 4.4 Results and Discussion

The assignment of the NOESY spectra was begun based on the backbone chemical shift assignment of ubiquitin by Cornilescu et al. [109]. Nevertheless the assignment had to be adjusted due to small chemical shift changes by different sample conditions, e.g. the temperature, buffer etc.. The assignment was conducted as followed:

1) Using the  $^{15}N$ ,  $^1H$  HSQC,  $^{13}C$ ,  $^1H$  HSQC to adjust larger variations due to the differences in temperatures. These spectra can be used to adjust the amide protons and some  $H_\alpha$  which are well separated, but fail for side chain aliphatic protons due to a insufficient dispersion of signals.

2) The  $^1H$ ,  $^1H$  TOCSY spectrum was used to identify, the backbone amides, the  $H_\alpha$  and some of the side chain protons. One assignment is shown as an example in figure 4.4.

3) Hereafter the fine adjustment of the peaks and evaluation of these peaks paying special attention to peak overlap was conducted using the  $^1H$ ,  $^1H$  NOESY spectra. With these spectra the identification of the amide protons and  $H_\alpha$  by correlation with preceding and subsequent residues was conducted. Due to the usually strong NOE between the amide proton of a residue and the  $H_\alpha$  of the preceding residue, it was possible to follow the continuous connectivity through the protein backbone (shown in figure 4.4 for the residues from 42 to 45).

4) Afterwards the side chains had to be assigned using the  $^1H$ ,  $^1H$  NOESY spectra. Especially for the methyl groups with their low chemical shift dispersion (an expanded view of the methyl and methylene region in an example spectrum is shown in figure 4.5), side chain

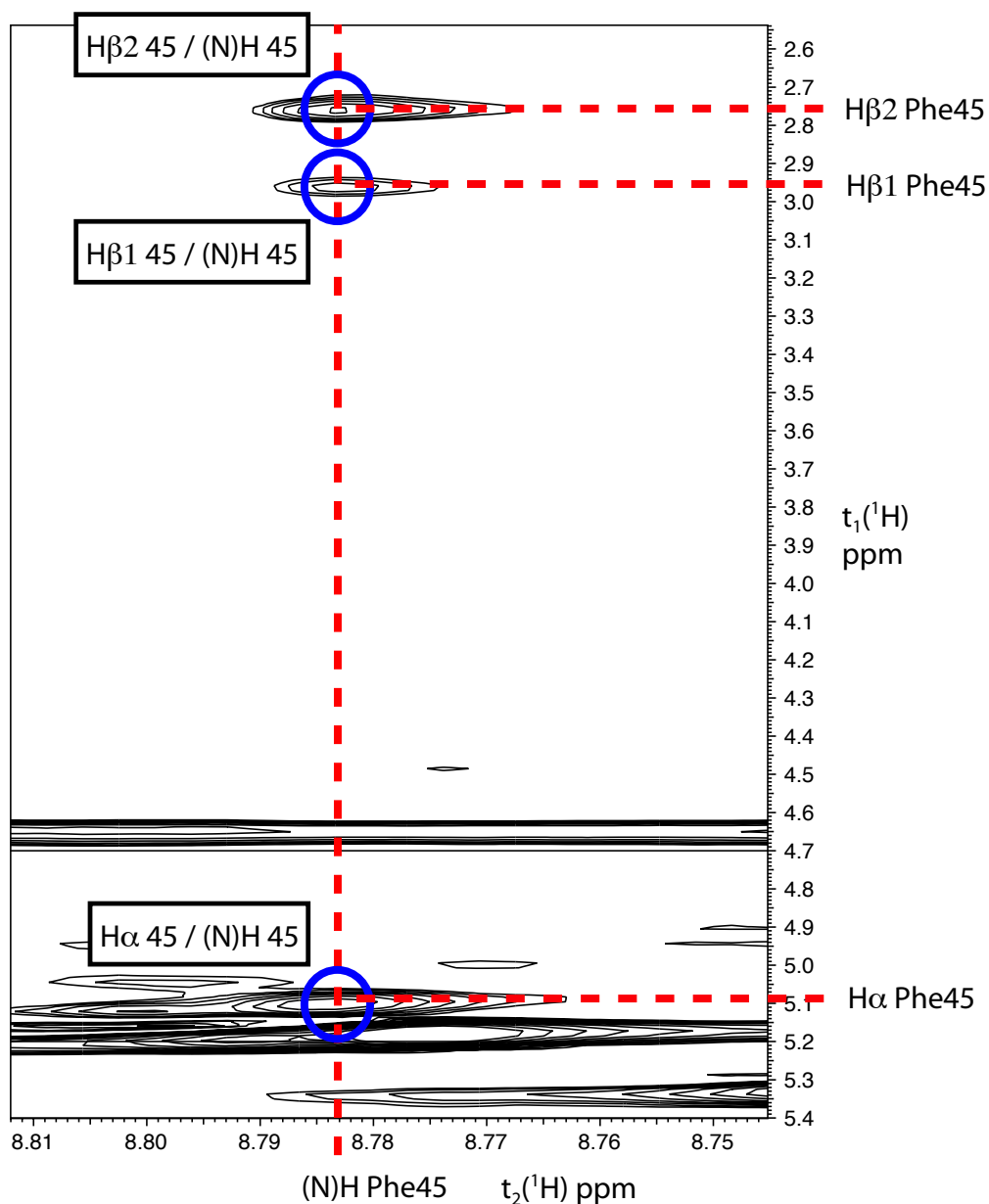


**Figure 4.3:** An expanded view in the TOCSY spectrum measured at a Bruker 700 MHz spectrometer with a TCI cryo probe head. The red lines show the connectivities in the spin system of the residue Phe45 from the amide proton in the direct  $t_2$  dimension to the  $H\alpha$ ,  $H\beta_1$ ,  $H\beta_2$  in the indirect  $t_1$  dimension. The three cross peaks are indicated by blue circles.

assignment was a very difficult task. Proton pairs within a sufficient distance for a NOE transfer were determined from the structure by Cornilescu et al. [109]. Normally for NOE transfers a maximal range of 5 Å is assumed, but to compensate for potential structural deviations, the analysis was conducted for all proton pairs within a distance of 7 Å.

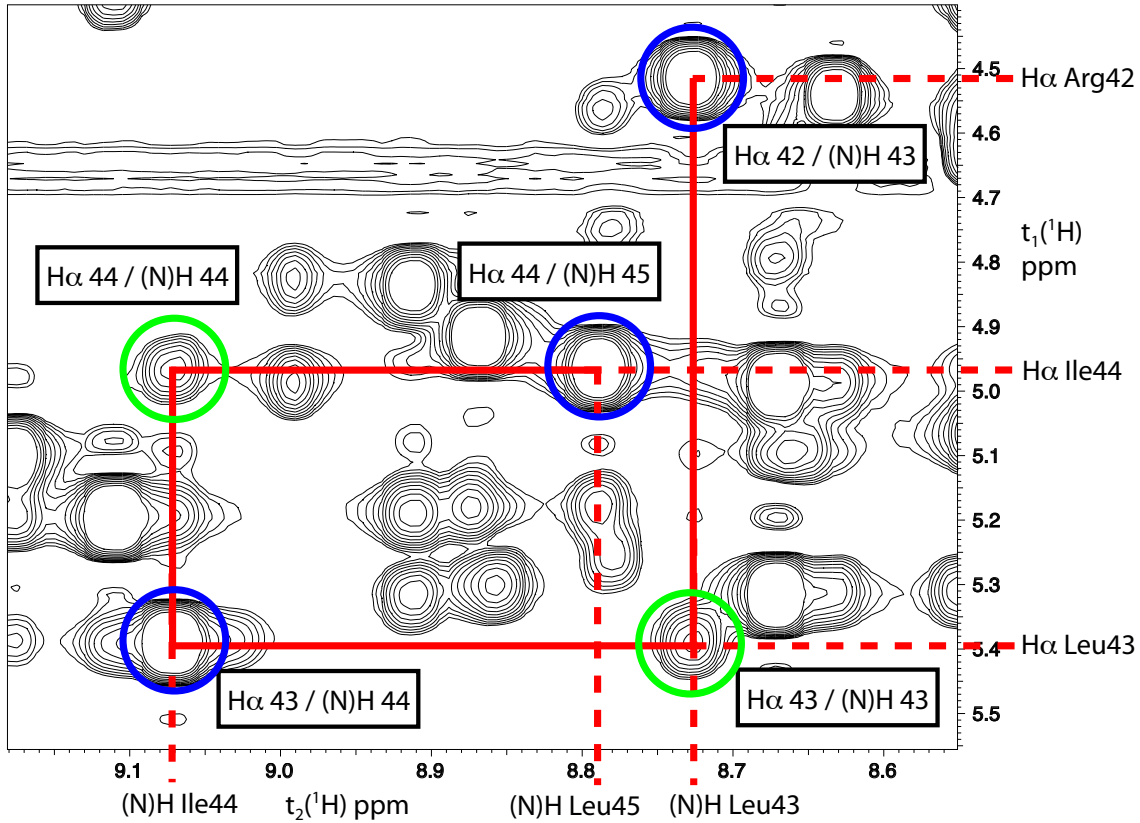


**Figure 4.4:** An expanded view in the NOESY spectrum measured at a Bruker 700 MHz spectrometer with a TCI cryo probe head with a mixing time  $\tau_{mix} = 150$  ms. The red lines as well as the blue and green circles indicate the assignment strategy for the backbone protons from the residues 42 to 45. The strong cross peaks between the (N)H -  $H_{\alpha}$  of sequential residues (marked with blue circles) and the weaker intra residual (N)H -  $H_{\alpha}$  cross peaks (marked with green circles) connect the residues through the protein backbone.

Even if there are more than 7000 ubiquitin proton pairs within a potential NOE transfer range of  $5 \text{ \AA}$ , only a small fraction of them can be assigned unambiguously and are separated well enough from other peaks to use them reliably for cross relaxation determination. After the assignment and evaluation of the NOESY spectra, 1170 cross peaks have been found as feasible for a determination of the cross relaxation rates. The chemical shifts of these peaks are noted in table 6.2 of the appendix.

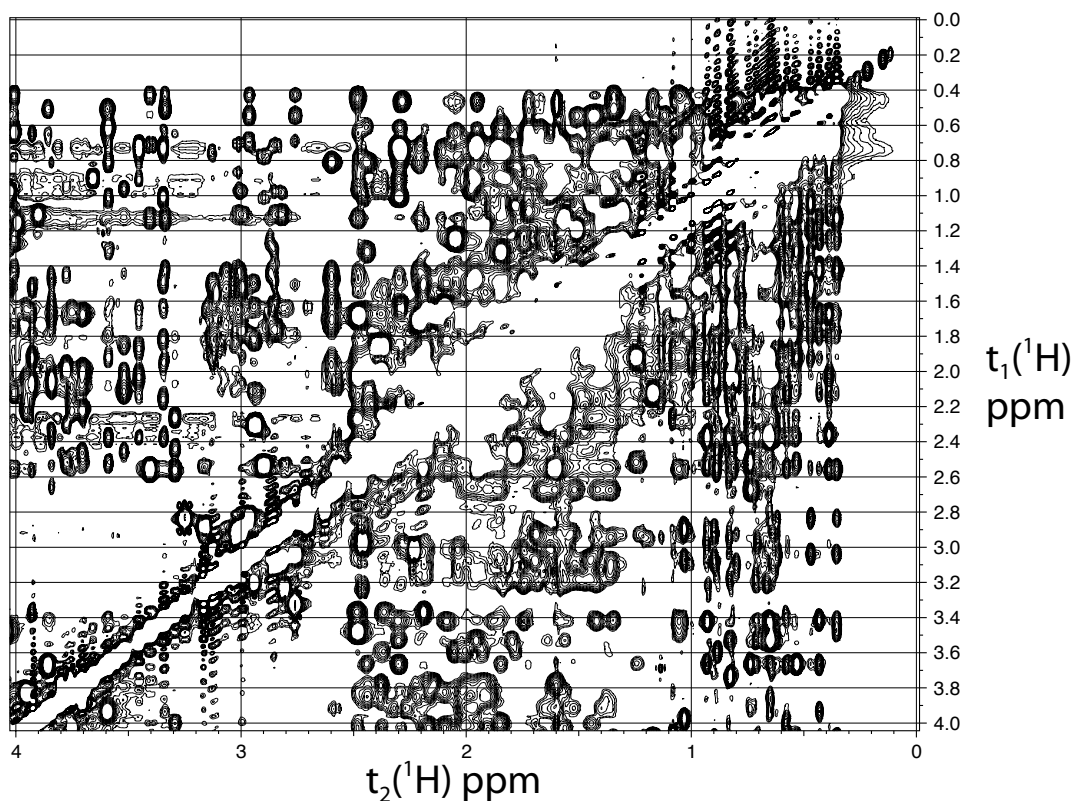


**Figure 4.5:** An expanded view in the NOESY spectrum measured at a Bruker 700 MHz spectrometer with a TCI cryo probe head with a mixing time  $\tau_{mix} = 150$  ms. 50 methyl protons aside from many methylene protons resonates in the chemical shift range from 0 to 2 ppm causing severe overlap.

Unfortunately the automatic intensity calculation of the NOE cross peaks shows some problems with the determination of the baselines of the spectra. Therefore many of the build up curves show positive or negative offsets in the intensities. For an exemplary cross peak the intensities were extracted manually to avoid offsets by these background problems and the cross-relaxation rates were determined fitting equation 4.4 to these intensities and to the automatically determined intensities. The intensities and the fitted build up curves for both approaches are shown in figure 4.6. Since a manual intensity extraction for all cross peaks would be extremely time-consuming, different programs as Atnos Candid [117, 118] or Sparky [119] should be tested if they are able to conduct the automatic integration without the background problems.

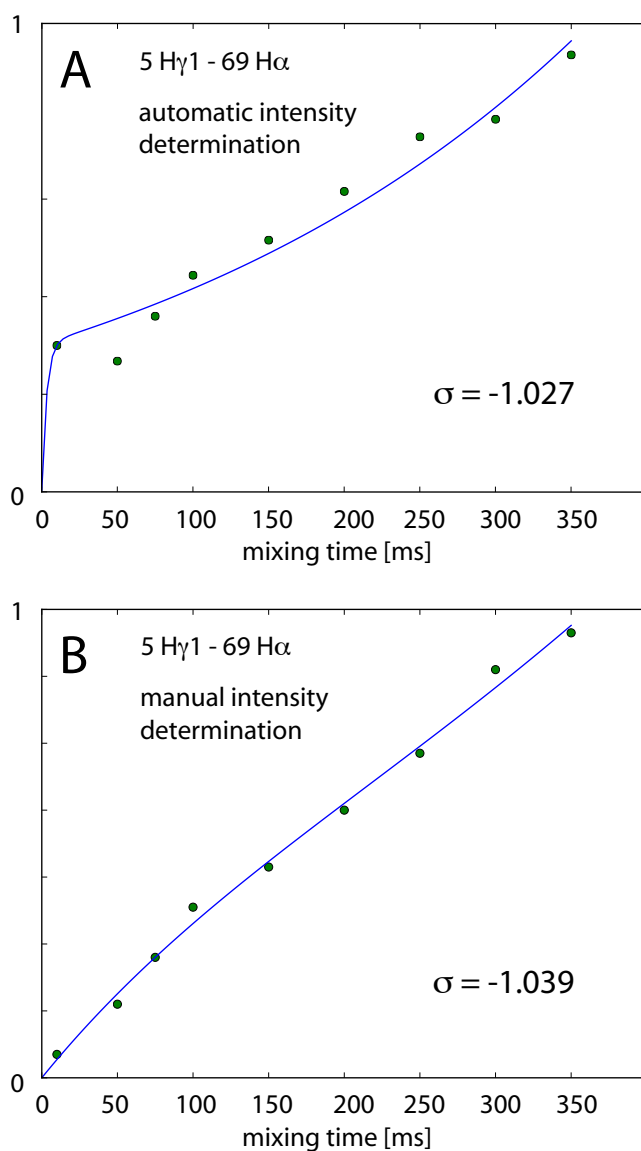


**Figure 4.6:** NOE build up curves from the NOESY spectra measured at a Bruker 700 MHz spectrometer with TCI cryo probe head for the proton pair Val 5  $H\gamma$ 1 - Ile 61  $H\alpha$ . The build up curves (blue curves) according to equation 4.4 were fitted to the intensities to determine the cross-relaxation rates  $\sigma$ . The intensities in graph A were extracted automatically using the program CARA [107], while the intensities in graph B were extracted manually.

## 4.5 Summary and Outlook

Beside residual dipolar couplings (RDCs) and cross-correlated relaxation (CCR) rates, cross-relaxation rates measured from the Nuclear Overhauser Effect (NOE) can be used as an indicator for the determination of dynamical aspects of proteins. In contrast to the sizes of RDCs and CCR rates which depend on angle dependencies of the internuclear vector to the static magnetic field of the spectrometer or a second internuclear vector, the size



of cross-relaxation rates depend only on the distance of the two involved nuclei under the assumption of isotropic molecular tumbling. These distance informations are widely used in solution NMR spectroscopy for the structure determination process. But the use of the dynamical informations of cross-relaxation rates is very limited until now. Nevertheless it has been shown that it is even possible to separate protein dynamics into motion faster or slower than the rotational correlation time [64]. Until now this was applied only to the backbone amide protons of the protein ubiquitin what restricts the dynamical informations these cross-relaxation rates can deliver. Therefore the goal of this study was it to measure the cross-relaxation rates for the fully protonated protein ubiquitin to gain more access to dynamical informations also for the tertiary structure of the protein.

Twenty-eight  $^1H, ^1H$  NOESY spectra of the fully protonated protein ubiquitin were measured for several mixing times and three field strengths.  $^{15}N, ^1H$  HSQC,  $^{13}C, ^1H$  HSQC and  $^1H, ^1H$  TOCSY experiments as well as the calculation of potential NOE transfers based on a static protein structure were used to assign the NOE cross peaks. Each peak was evaluated if it is reliable assigned and well enough separated to other peaks for the determination of cross-relaxation rates. From ubiquitin with its more than 7000 proton pairs in a sufficiently close distance for a NOE transfer, 1170 cross peaks could be identified. To extract reliably the cross-relaxation rates from these peaks, just a problem with the automatic calculation of the peak intensities still has to be solved.

As a next step it should be tested if different programs as Atnos Candid [117, 118] or Sparky [119] are able to determine the correct absolute intensities of the cross peaks without the present baseline problems. If these problems can be solved, the cross-relaxation rates will be determined from the intensities and can afterwards used for the direct calculation of order parameter as a description of the motional amplitudes. Alternatively, the determined cross-relaxation rates could be probably used as restrains in the creation process of new structure ensembles, which could describe the protein dynamics even more precise.



## Chapter 5

# Investigations of Membrane Proteins in Hydrophobic Environments for Solution NMR

### 5.1 Introduction

From the proteins encoded in a typical genome 20-30 % are transmembrane proteins [66]. Many of them have essential roles for the functionality of the cell in e.g. transmembrane transport or signalling processes. Transmembrane proteins span through the whole lipid environment reaching partially into the extramembrane space. Two intramembrane motifs are commonly found in transmembrane proteins: either one or more hydrophobic  $\alpha$ -helices or a  $\beta$ -barrel consisting of a cylindrical  $\beta$ -sheet.

Although a major part of all proteins are transmembrane proteins, the number of solved membrane protein structures is very limited. Less than 300 transmembrane protein structures are registered in the Protein Data Bank. In order to correctly fold transmembrane proteins, a hydrophobic environment is necessary to cover the intramembrane regions of the protein. For the structure determination of transmembrane proteins via solution NMR or x-ray crystallography detergents such as 1,2-dihexanoyl-sn-glycero-3-phosphatidylcholine (DHPC), lauryldimethylamine-N-oxide (LDAO) or dodecylphosphatidylcholine (DPC) are normally needed to form a micelle around the hydrophobic part of the protein [67, 68, 69, 70, 71]. While the x-ray crystallography of membrane proteins are plagued by problems in the crystallization process caused by the detergents, is the structure determination of membrane proteins by solution NMR complicated by the faster relaxation due to the increased effective size of the protein by the surrounding micelle. These micelles differ strongly from a physiological lipid bilayer, due to the strong curvature at their surface and the different lateral pressure on the detergent-protein interface [72, 73]. In addition, it was shown

that some membrane proteins are inactive in micelles [74, 75]. Therefore the physiological relevance of structures determined under such conditions have been questioned. These problems can be potentially addressed by the use of small bicelles as a hydrophobic environment. Such bicelles consist of a lipid bilayer with a flat surface, e.g. 1,2-dimyristoyl-sn-glycero-3-phosphatidylcholine (DMPC) or 1,2-dilauroyl-sn-glycero-3-phosphatidylcholine (DLPC), surrounded at the edges by detergents [76, 77, 78]. In previous studies concerning the implementation of small bicelles as a hydrophobic environment for biomacromolecules, investigation focused on the interactions between the bicelle and macromolecular peptides [79, 80, 81]. Here an intact integral transmembrane protein was examined in the context of a bilayer environment.

In this study small DMPC:DHPC bicelles with a lipid:detergent ratio of 1:2 were investigated for its use as an environment for the structure determination of membrane proteins. As a model protein, the integral outer membrane protein OmpX from *Escheria coli* was used [82]. This protein is quite efficient to express and has only 150 residues. Also as a  $\beta$ -barrel protein, good dispersion of the backbone signals should be observed in the spectra of OmpX. The protein-bicelle complex was investigated due to its size and composition. The backbone assignment of OmpX in the bicelles was conducted by double- and triple resonance experiments. Afterwards intermolecular NOEs and data from a paramagnetic relaxation enhancement (PRE) experiment were used to investigate the interface between the protein and the lipid-detergent environment in detail. This project was conducted together with Dr. Donghan Lee.

## 5.2 Material and Methods

### The Sample

The 1,2-dihexanoyl-sn-glycero-3-phosphatidylcholine (DHPC) and 1,2-dimyristoyl-sn-glycero-3-phosphatidylcholine (DMPC) were purchased from Avanti Polar Lipids (Alabaster, AL), while the Gadolinium-diethylene triamine pentaacetic acid (Gd DTPA) was obtained from Schering AG (Berlin, Germany).

$^{15}N$ ,  $^{13}C$ , ( $\approx 85\%$ )  $^2H$  OmpX expressed, purified and refolded in DHPC micelles according to Fernandez et al. [120] was kindly provided by Dr. Stefan Becker and Ann-Kathrin Brückner. The protein concentration in the samples were ca. 3 mM, with a DHPC concentration of 300 mM in a 50 mM sodium phosphate buffer with 100 mM NaCl at pH = 6.8, 0.1 % (w/v) together with  $NaN_3$ . The DHPC concentration was verified by an 1D spectrum compared to a 100 mM DHPC reference sample.

For the bicelle sample DMPC was added up to a concentration of 150 mM. The solving process of the DMPC was accelerated by cycles of cooling the sample in a ice bath, vortexing it and heating it to 42 °C. The cooling lowers the viscosity of the solution to improve the mixing by the vortexing, while the successive heating improves the dissolving of the lipid molecules. This cycle was repeated until the DMPC has been dissolved and the sample was homogenous. The correct DHPC:DMPC molar ratio was adjusted by the measurement of the intensities of the DHPC and DMPC methyl groups from an 1D spectrum.

## The NMR Experiments

The relaxation rates were determined using the TRACT pulse sequence by Lee et al. [121]. The relaxation delays incremented in 2 ms steps between 0 and 100 ms. Furthermore for the investigation of the bicelle composition several  $^1H$  and  $^{31}P$  spectra as well as a 2-dimensional  $^1H$ ,  $^1H$  TOCSY were measured. For the  $^1H$ ,  $^1H$  TOCSY the clean TOCSY mixing [116] was used with the MLEV16 sequence (80 ms). It was recorded with  $t_1 = 256$  x  $t_2 = 512$  complex points. While the  $^1H$  spectra of DHPC and DMPC in aqueous solutions were measured at a Bruker 400 MHz with a TCI room temperature probe head at a temperature of 293 K, all other experiments were conducted at a Bruker 600 MHz spectrometer with a QXI room temperature probe head at a temperature of 303 K.

For the backbone assignment TROSY, TROSY-HNCA [122] and  $^{15}N$  resolved  $^1H$ ,  $^1H$ -NOESY experiments were conducted at a Bruker 900 MHz spectrometer with a CP-TCI cryo probe head at a temperature of 318 K. The TROSY was recorded with  $t_1 = 58$  x  $t_2 = 1024$  complex points, the TROSY-HNCA with  $t_1 = 64$  x  $t_2 = 64$  x  $t_3 = 1024$  complex points and the  $^1H$ ,  $^1H$ -NOESY with  $t_1 = 70$  x  $t_2 = 100$  x  $t_3 = 1024$  complex points.  $^{15}N$  resolved  $^1H$ ,  $^1H$ -NOESY experiments were conducted with mixing times of 50 ms and 150 ms.

Paramagnetic relaxation enhancement (PRE) was applied to OmpX in bicelles similar to Hilty et al. [123]. Gadolinium-diethylene triamine pentaacetic acid (Gd DTPA) was titrated into the OmpX in bicelle sample over a Gd DTPA concentration of 0 to 100 mM and after each step a TROSY experiment was measured. The measurements were conducted on a Bruker 700 MHz spectrometer with a TXI cryo probe head at a temperature of 318 K with  $t_1 = 128$  x  $t_2 = 1024$  complex points.

For the processing the program NMRPipe [106] and for the assignment the program CARA (R. Keller and K. Wuthrich [107]) were used.

### 5.3 Results and Discussion

This project consisted of three parts: first the membrane protein - bicelle complex was studied due to its size and composition. Next the protein backbone resonances of OmpX in bicelle were assigned by two- and three-dimensional NMR experiments. Finally the interface between the protein and the lipid-detergent molecules was investigated.

#### 5.3.1 The Bicelle Composition

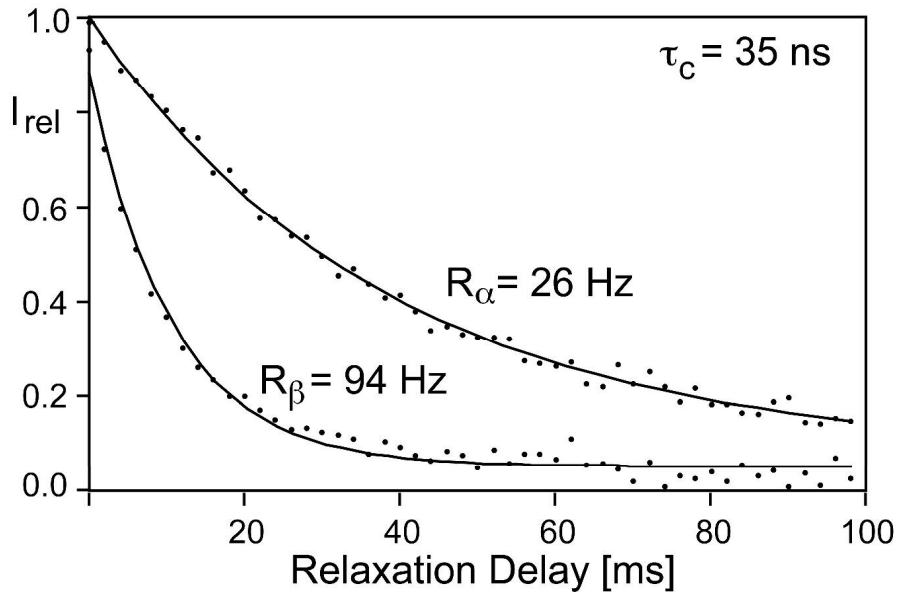


**Figure 5.1:** The decay curves of the  $^{15}\text{N}$  intensities of OmpX in bicelles from the 1D TRACT experiment. The relative intensities were determined by integration over the chemical shift range from 6.5 to 10.5 ppm. The upper curve corresponds to the  $^{15}\text{N}$   $\alpha$  spin state, while the lower one corresponds to the  $\beta$  spin state. From these rates, the overall rotational correlation time of the OmpX - bicelle complex can be estimated as 35 ns.

The size of the OmpX in the DMPC:DHPC bicelles was investigated using the TRACT NMR experiment [121]. Measuring 1D spectra for relaxation delays from 0 to 100 ms the intensity decay curves for the  $^{15}\text{N}$   $\alpha$  spin state and the  $\beta$  spin state of the OmpX amides can be determined. These two curves are shown in figure 5.1. From the difference of the two relaxation rates ( $R_\alpha = 26$  Hz and  $R_\beta = 94$  Hz) the overall rotational correlation time of the OmpX-bicelle complex can be estimated as 35 ns leading to a molecular weight of the OmpX bicelle complex of around 90 kDa. In contrast, the OmpX-micelle complex has an estimated molecular weight of 60 kDa. From this it can be concluded that the bicelle environment of a OmpX protein consists of ca. 45 DMPC- and 90 DHPC-molecules.

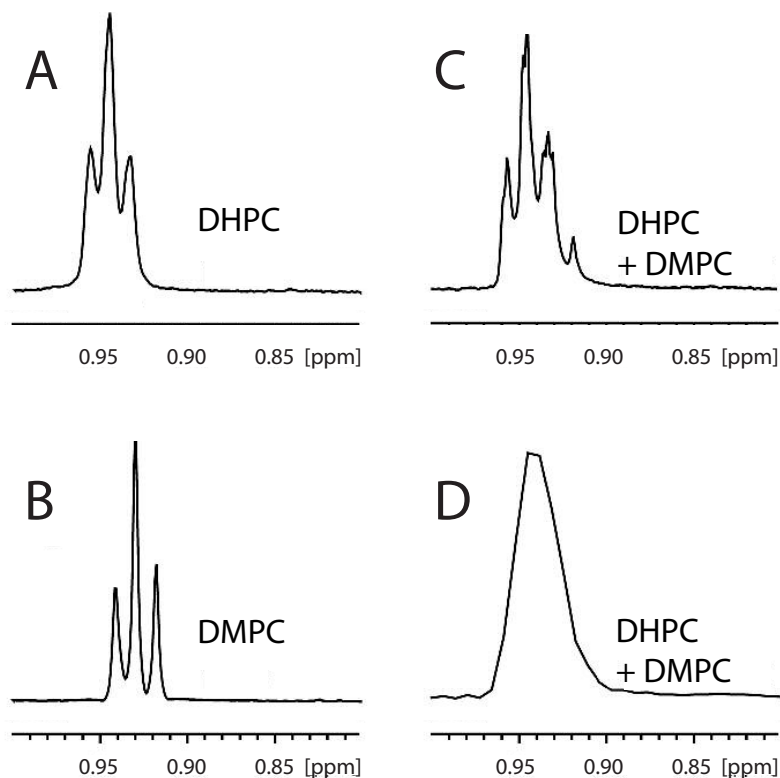


**Figure 5.2:** 1D  $^1H$  spectra of the  $\omega$  methyl groups of DHPC (A) and DMPC (B) in methanol at a temperature of 293 K. The concentration of DHPC were 6 mM and of DMPC were 2 mM. The DHPC and DMPC solutions were mixed (C and D). The spectra A, B and C were recorded with a very long  $t_{1max} = 967$  ms, what leads to an extremely good resolution, while spectrum D is recorded with  $t_{1max} = 121$  ms, what is in a realistic range for the direct dimension of typical multidimensional experiments (as used in all other experiments). This shows that the differences in the chemical shifts of DHPC and DMPC in methanol are very small and prove that the DHPC and DMPC molecules are in very similar structural environment (in contrast to the spectra of the molecules in aqueous solution in figure 5.3). The triplet structure in the high resolution spectra of pure DMPC (A) or DHPC (B) originates from the coupling with the two protons of the preceding methylene group. The multiplet structure in spectrum C is an overlay of the two overlapping triplets of DHPC and DMPC.

Dynamic Light Scattering was used to check that for the concentrations and conditions used in the NMR experiments no significant aggregation occurred.

Four  $^1H$  spectra (as shown in figure 5.2) were measured for DHPC and DMPC and the mixture of DHPC and DMPC in methanol. The chemical shift changes for the methyl groups of DHPC and DMPC are very small and not well resolved with a typical resolution

as long as they are in methanol. This suggests that the DHPC and DMPC molecules either do not aggregate in weak polar solutions or form complexes without substantial structural differences for DHPC and DMPC.

By contrast the  $^1H$  spectra of DHPC or a mixture of DHPC and DMPC in an aqueous solution show clearly two sets of chemical shifts for the methylene and methyl protons (figure 5.3). These spectra reveal that in a strong polar solution like water the amphiphilic DHPC and DMPC molecules form a complex with clearly two different environments for the lipid and detergents. In addition it can be observed that there is no significant change of the lipid and detergent chemical shifts by the addition of the membrane protein OmpX. The lipid-detergent separation in the different environments is also confirmed by the measurement of 1D  $^{31}P$  spectra (shown in figure 5.4) of DHPC and DMPC in methanol (A) and in an aqueous solution. This assignment was later on used for the adjustment of the correct DHPC:DMPC ration and for the study of the interactions between OmpX and the lipid-detergent bicelle.

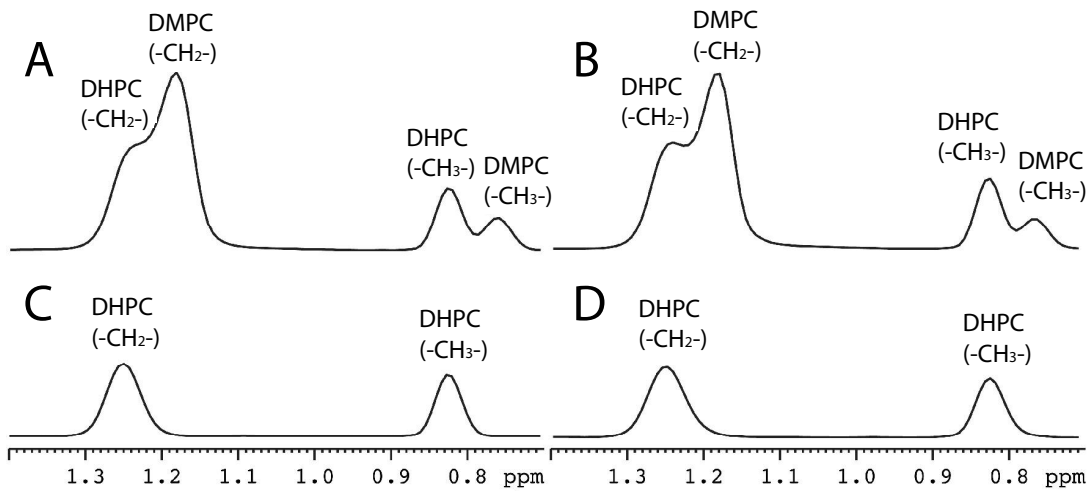


**Figure 5.3:** 1D  $^1H$  spectra of DHPC (C and D) and of a mixture of DHPC and DMPC with a molar ratio of 2:1 in an aqueous buffer solution (50 mM sodium phosphate buffer with 100 mM NaCl at pH = 6.8, 0.1 % (w/v) together with  $NaN_3$ ) at a temperature of 303 K. Spectra A and C are without and spectra B and D containing the membrane protein OmpX.



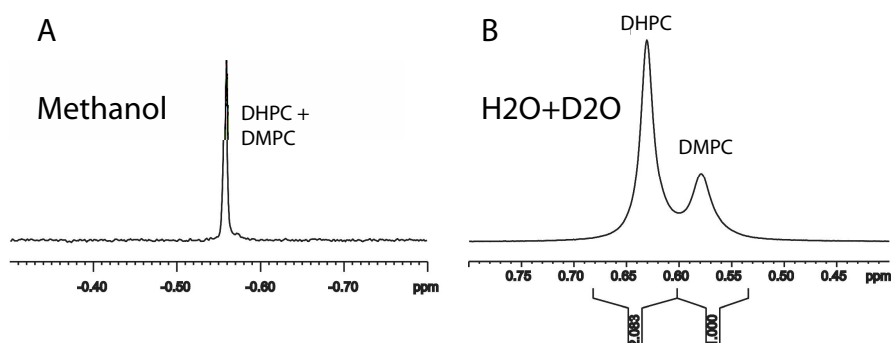


**Figure 5.4:** 1D  $^{31}\text{P}$  spectra of DHPC and DMPC in a molar ratio of 2:1 in methanol (A) and in an aqueous buffer solution (50 mM sodium phosphate buffer with 100 mM NaCl at pH = 6.8, 0.1 % (w/v) together with  $\text{NaN}_3$ ) containing OmpX measured at a temperature of 303 K.

The assignment of the four peaks in the mixture of the DHPC and DMPC molecules in figure 5.3 was confirmed by the measurement of a 2-dimensional  $^1\text{H}$ ,  $^1\text{H}$  TOCSY (figure 5.5). It shows that the lipids and detergents are experiencing two unique structural environments in the bicelle.

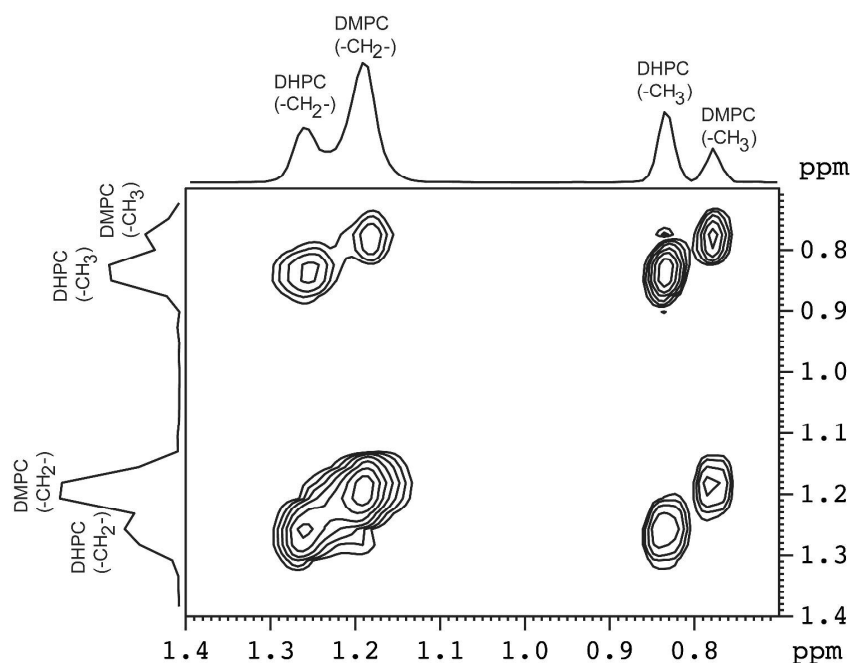


**Figure 5.5:** Spectrum of the 2-dimensional  $^1\text{H}$ ,  $^1\text{H}$  TOCSY [116] of small bicelles of DHPC and DMPC at a molar ratio of 2:1 containing the membrane protein OmpX. It was measured at a temperature of 303 K.

These results are in good agreement with earlier studies of similar bicelles with  $^{31}\text{P}$  NMR, DLS, Fluorescence spectroscopy and electron microscopy [77]. This subsection was published in Lee et al. [124].

### 5.3.2 The Protein Structure of OmpX in Bicelles

Some years ago the protein structure of OmpX in micelles was solved by solution NMR by Fernandez et al [68, 133]. Based on this assignment the structure of OmpX in bicelles was determined using TROSY, TROSY-HNCA [122] and  $^{15}\text{N}$  resolved  $^1\text{H},^1\text{H}$ -NOESY experiments. Especially the long-range NOEs in the  $^{15}\text{N}$  resolved  $^1\text{H},^1\text{H}$ -NOESY spectrum delivered valuable informations for the assignment of the  $\beta$ -sheet motif. Using these experiment it was possible to assign ca. 95 % of the residues.

Interestingly the TROSY spectra of OmpX in micelle and in bicelle (figure 5.6) showed significant changes in their chemical shifts (figure 5.7), which indicates structural differences of OmpX in these two environments, but could also be caused by the different "solvent". Since the lipid bilayer system of the bicelle is closer to a membrane as detergent micelles, it is interesting to find out whether and how much the structure of OmpX is changed between micelle and bicelle.

Additional NMR parameters delivered inconclusive results regarding significant structural changes: The  $^{15}\text{N}$  resolved  $^1\text{H},^1\text{H}$ -NOESYs of OmpX in bicelles show only one potential interstrand NOE (between residues Arg 50 and Asn 58) for the extra membrane region between  $\beta$ -strands 3 and 4 and no interstrand NOEs between  $\beta$ -strands 5 and 6, while the intrastrand NOEs and the interstrand NOEs in the membrane region are conserved. This could point perhaps to a partial opening of these extra membrane  $\beta$ -strands, while the  $\beta$ -barrel motif is conserved in the rest of OmpX in micelles to bicelles. Contrary to the missing inter  $\beta$ -strand NOEs, a chemical shift index (CSI) analysis [125, 126] of the backbone nuclei predicts for the extra membrane residues no systematic change from a  $\beta$ -strand form to an unstructured form.

Residual dipolar couplings (RDCs) of the amide groups in the protein backbone would have been of great value to verify these indications for this structural change. To measure RDCs of the protein it has be aligned by an internal or external source. Most of the commonly used alignment media are not feasible for this task, because the high concentration of solved detergent interferes with the build up of the global ordering of the anisotropic media. Approaches with three alignment media were unsuccessfully conducted:

In a first approach, the molar DMPC:DHPC ratio of the bicelles including the membrane proteins was raised from 1:2 to 3:1. Such large bicelles are self-aligning under specific conditions in the static magnetic field of the spectrometer [31] and the membrane proteins

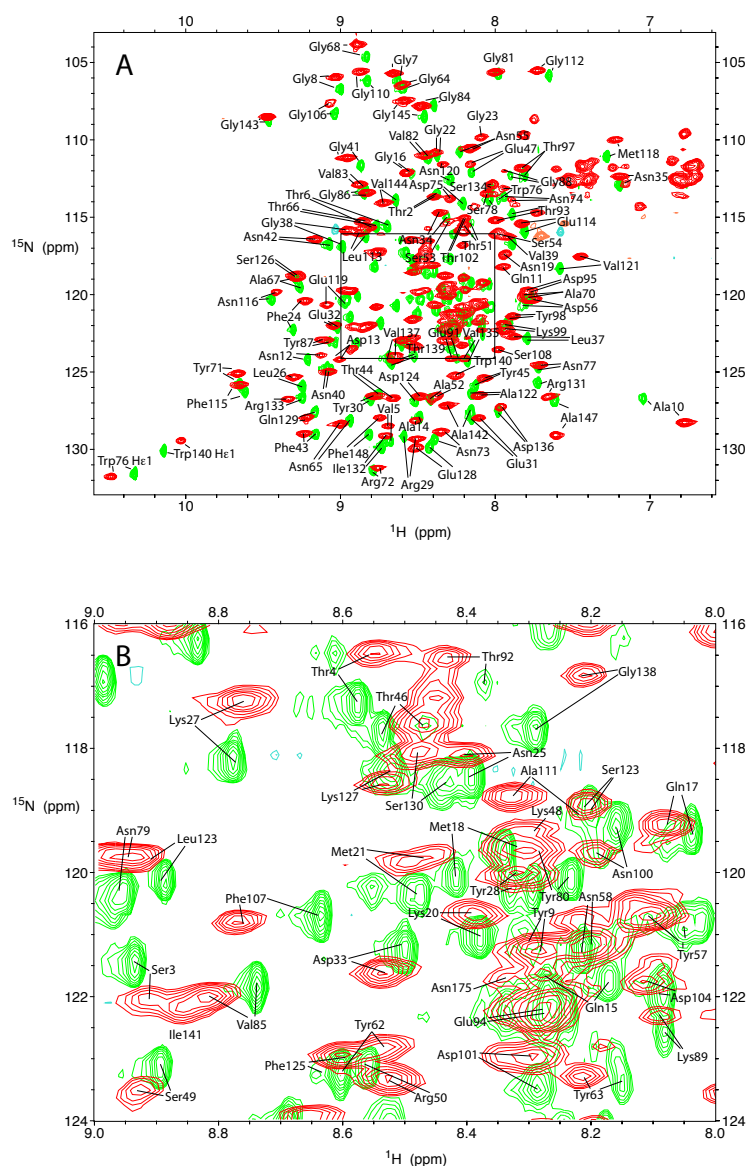


**Figure 5.6:** Figure A shows a assigned superposition of the TROSY spectra from OmpX in micelles (green peaks) and OmpX in bicelles (red peaks). They were recorded at a Bruker 900 MHz with a CP-TCI probe head at a temperature of 318 K. Figure B shows an expanded view of the center region of the TROSY (marked in figure A as a black square) to increase the lucidity of the assignment. This figures were created using the program Sparky [119].

which reside in the bicelles show large dipolar couplings. Since these large RDCs lead to a very fast relaxation no usable spectra were measurable. To reduce the size of the RDCs the sample was transferred into a high-resolution magic angle spinning (HR-MAS) sample rotor, but due to the strong reduction of the sample volume no adequate spectrum for RDC determination could be achieved.

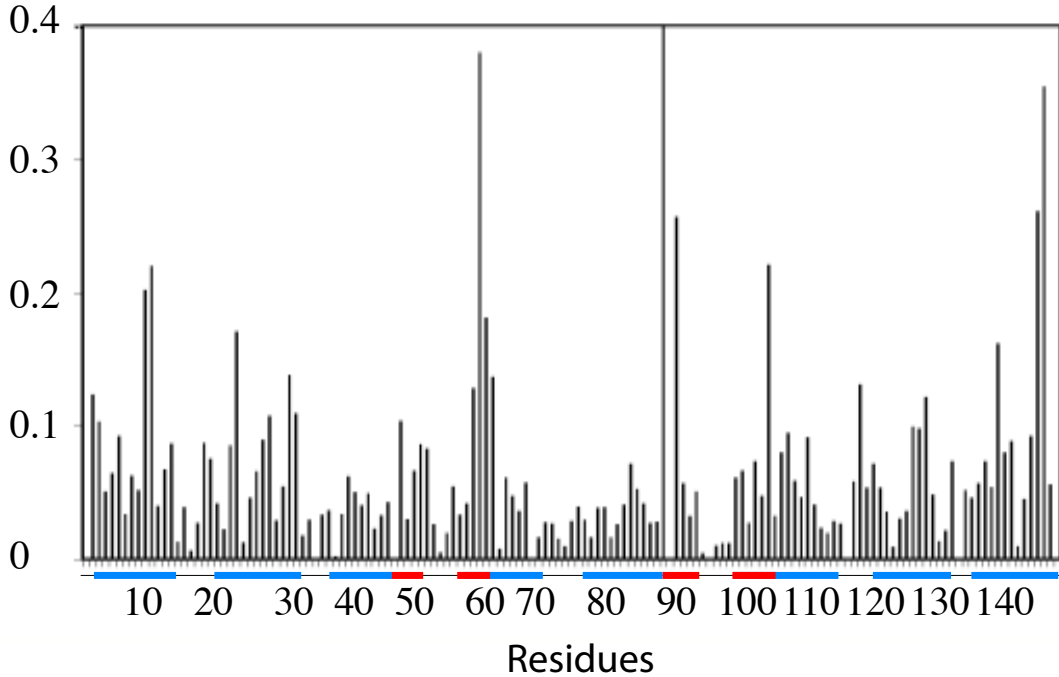


**Figure 5.7:** Chemical shift differences of the residues in the TROSY spectra of OmpX in micelles and bicelles. The chemical shift differences  $\Delta\delta = \sqrt{((\Delta^1H)^2) + (0.2 \cdot \Delta^{15}N)^2}$  with  $\Delta^1H = {}^1H(\text{bicelles}) - {}^1H(\text{micelles})$  and  $\Delta^{15}N = {}^{15}N(\text{bicelles}) - {}^{15}N(\text{micelles})$ . The blue bars indicate the residues in  $\beta$ -sheet (according to the x-ray structure by Vogt & Schulz (pdb code: 1QJ8) [82]) in the membrane covered region, while the red bars indicate residues in  $\beta$ -sheet in the extra membrane region.

In a second attempt, polyacrylamide gels were used as alignment media. The gels consisted of 2-acrylamido-2-methyl-1-propanesulfonic acid and *N,N*-dimethylacrylamide, bis-methylen acrylamide and ammonium persulfate in a molar ratio of 1:1:0.03:0.008. The polymerization ran for 11 minutes in a water bath at a temperature of 75 °C. All chemicals were purchased from Sigma-Aldrich. The procedure to create these gels was conducted analog to the description in [127]. After addition of the bicelle solution to the dried gel, the gel swells, but after short time a white precipitate was observed inside the gel. It was proposed that either the detergent molecules interacted with the gel, what reduced the detergent concentration in solution and led to a precipitation of the lipids, or the lipids directly get bound by the gel. The precipitate led to a very heterogeneous environment which prohibited all high-resolution measurements.

In a third approach, DNA-nanotubes (purchased from Rasayan Inc., Encinitas, CA, USA) were attempted as an alignment medium for the membrane proteins in bicelles [128, 129]. The purchased DNA-nanotubes were dissolved in a potassium phosphate buffer. The alignment of this solution was checked measuring a 1D deuterium spectrum. In an anisotropic alignment medium the quadrupole of the deuterium leads to a splitting of the deuterium

peak in the spectrum. While the DNA-nanotubes in the potassium phosphate buffer showed clearly an alignment, after the addition of detergents no alignment could be observed anymore. The DNA-powder was checked using 1D  $^1H$ , 1D  $^{31}P$ , 2D  $^1H, ^1H$ -TOCSY and 2D  $^1H, ^1H$ -NOESY experiments. Several impurities were found, which could perhaps responsible for the instability of the DNA-nanotube structures regarding detergents. Therefore, further investigations have to show if these indications really denote such a change in the secondary structure of the protein.

### 5.3.3 The Membrane Protein - Bicelle Interface

After the assignment of the backbone of OmpX in bicelles, the  $^{15}N$  resolved  $^1H, ^1H$ -NOESY spectra provided additional valuable informations of the protein - bicelle interface.

Intermolecular NOEs show direct contacts between the amide groups of each specific residue of OmpX and the methyl and methylene groups of the DHPC and DMPC molecules as well as their head groups. Representative examples of the  $^{15}N$  resolved  $^1H, ^1H$ -NOESY spectra are shown in figure 5.8. As expected no intermolecular NOEs from the lipids and detergents to residues in the loops and turns of the protein are observed, while the intermolecular NOEs cover a region of around 2.7 nm centered around the middle of the  $\beta$ -barrel.

Additionally, a titration of the water solvable paramagnetic component Gadolinium-diethylene triamine pentaacetic acid (Gd DTPA) was added to the sample of OmpX in bicelles to measure the paramagnetic relaxation enhancement (PRE) [131, 132] similar to Hilty et al. [123]. The paramagnetic Gd DTPA dissolved in the solution causes an increased relaxation for protein residues. Therefore a fast decrease of signal intensity with the addition of GD DTPA indicates that the corresponding residue is located in the solution exposed extra membrane region of the protein and not protected by the lipid bilayer of the bicelle. The protein regions covered by the hydrophobic part of the lipid-detergent complex (shown in figure 5.9) determined by the PRE measurement is in very good agreement with the inter-molecular NOE data. The regions of OmpX covered by the hydrophobic environment determined in this way are very similar for the measurement in micelles and bicelles [133].

The  $^{15}N$  resolved  $^1H, ^1H$ -NOESY spectra showed no intermolecular NOEs between OmpX and the aliphatic groups of the detergent DHPC, while almost all residues of the  $\beta$ -barrel showed intermolecular NOEs from the sidechains of the lipid DMPC (as shown for some representative residues in figure 5.8). This proves that the membrane protein is incorporated in the lipid bilayer and does not have contacts to the detergents covering the rim of the bicelle. Most of the intermolecular NOEs originated from the methylene groups and only few from the methyl groups of the DMPC sidechains. The residues with NOEs from methyl groups of the DMPC are roughly located around the center of the  $\beta$ -barrel (as shown in figure 5.10). That these contacts are not forming a regular ring around the center of the hydrophobic region of the protein could suggest that not only the protein is influenced by

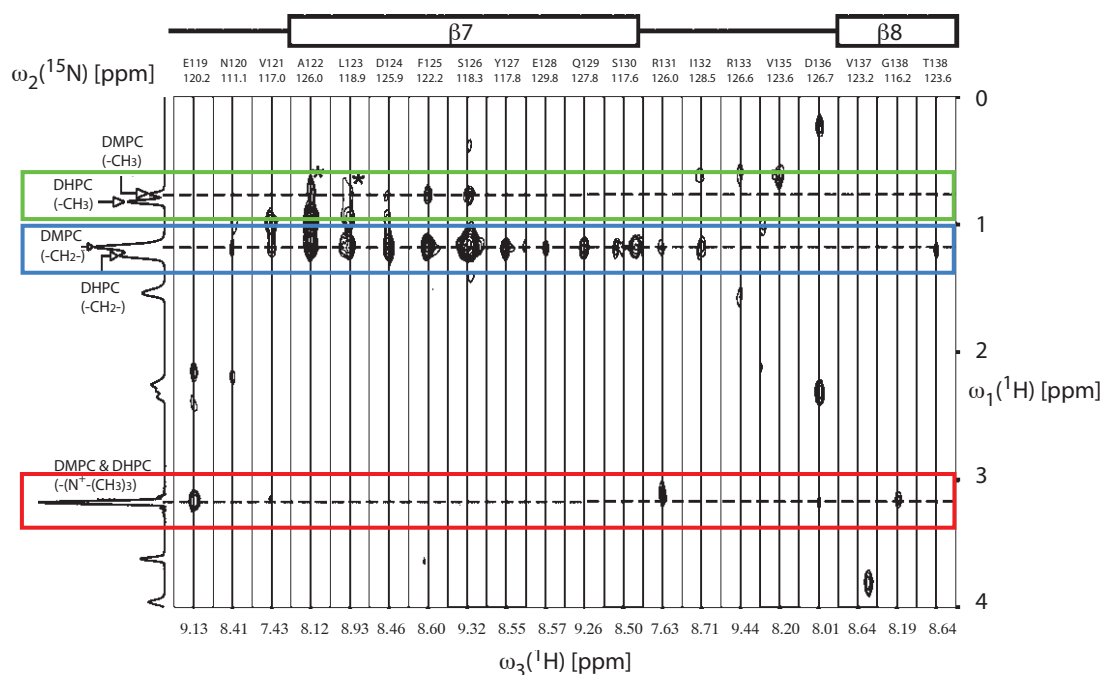


**Figure 5.8:** Representative  $\omega_1(^1H)/\omega_3(^1H)$  strips of the residues 119 - 139 from the  $^{15}N$  resolved  $^1H, ^1H$ -NOESY experiment with  $\tau_{mix} = 150$  ms. The residue numbers and their  $^{15}N$  chemical shift are indicated on top of the strips. On top of that a graphical representation indicates the secondary structure elements of this protein segment. On the left side of the spectrum the 1-D  $^1H$  spectrum of the DMPC/DHPC bicelle is shown. The horizontal dashed lines indicate the position of signals which arise from NOE transfer from the hydrophobic chain ( $-CH_2-$  (blue box) and  $-CH_3$  (green box)) of DMPC and the nitrogen-bound methyls ( $-N^+ - (CH_3)_3$  (red box)) of the choline groups to the amide protons of the residues. The peaks on the strips of A122 and L123 marked with an asterisk arise from NOEs from residual methyl protons from OmpX side chains. This figure was created based on a figure kindly provided by Dr. D. Lee.

the lipid bilayer, but it also could be that the order of the lipids is distorted by the interactions with the protein. Additional experiments about this question are planned. For example, the thickness of the lipid bilayer of the bicelles can be varied using lipids with longer or shorter hydrophobic chains. Additional studies of NOEs and relaxation rates in these different bicelles could deliver interesting informations about the interaction between lipids and the membrane protein.

The distribution of methylene and methyl contacts to the protein indicates to a model of the protein - bicelle complex in which the lipid molecules surrounds the protein  $\beta$ -barrel parallel. Such a model is in good agreement with previous studies on protein-free bicelles [78, 134]. In contrast, in micelles the intermolecular NOEs to the residues of the  $\beta$ -barrel are

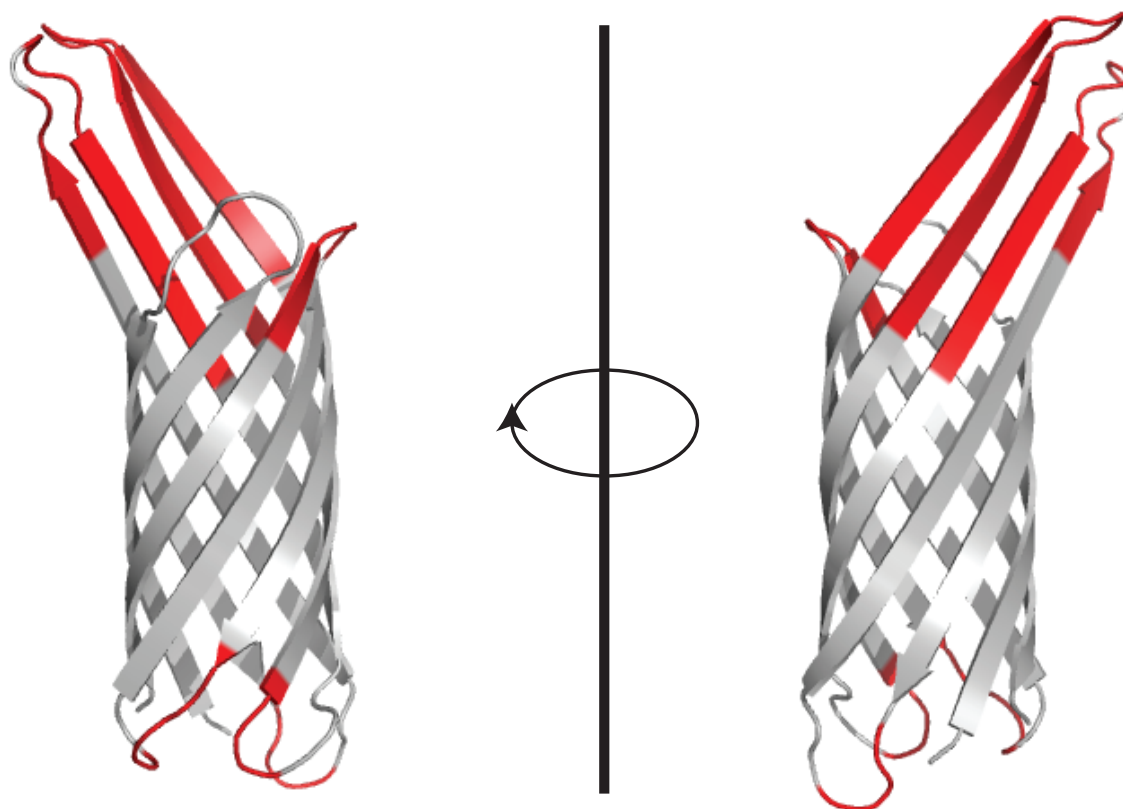


**Figure 5.9:** Drawing of the OmpX structure by Vogt & Schulz (pdb code: 1QJ8) [82]). Solvent exposed residues of the extra membrane region of the protein which show a paramagnetic relaxation enhancement higher than  $6 \text{ mM}^{-1}\text{s}^{-1}$  during the Gd DTPA titration are colored red. This figure was generated using the program PyMOL [130].

dominated by transfers from the methyl groups of the DHPC molecules [133]. This suggests a model where the DHPC molecules stand mainly perpendicular around the  $\beta$ -barrel.

In addition to the intermolecular NOEs from the aliphatic groups of DMPC the  $^{15}\text{N}$  resolved  $^1\text{H}, ^1\text{H}$ -NOESY spectra also showed transfers from the choline head groups of DMPC or DHPC. In contrast to the measurements on OmpX in micelles [133] the number of head group contacts is highly increased; 8 contacts in bicelles compared to 2 contacts in micelles. This can be explained by the tighter packed head groups in a bicelle compared to the more loose packing in a micelle with its strong curvature. Since stronger interactions between the polar head groups of the micelle or bicelle environment and the residues on the edge of the intra and extra membrane regions could also influence the structure and functionality of the membrane protein, this could be another relevant difference between micelles and bicelles as an environment for the investigation of membrane proteins.

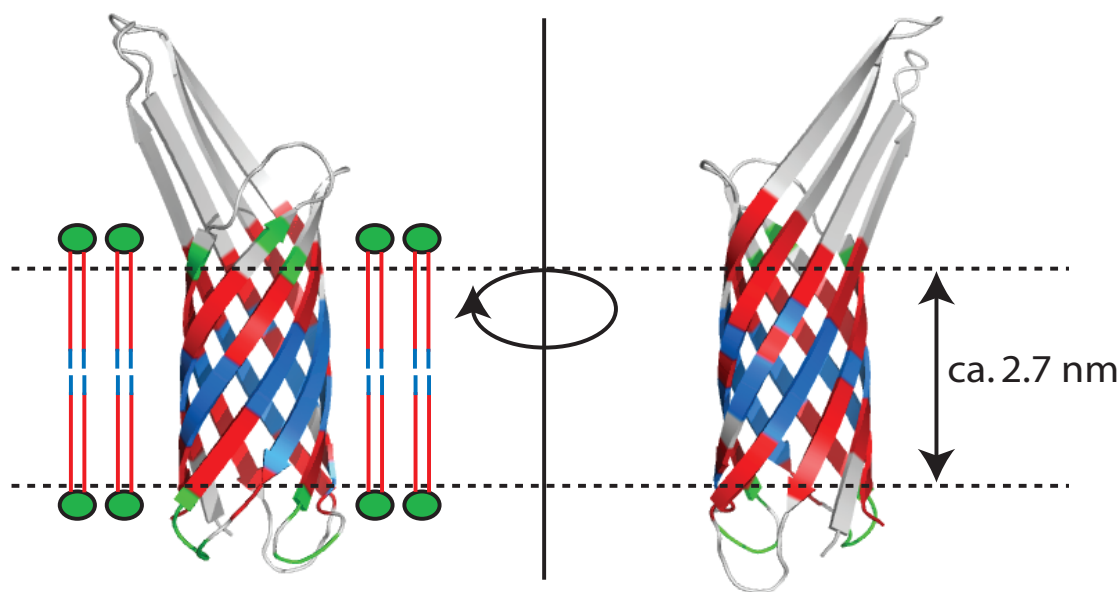


**Figure 5.10:** Structure of OmpX (pdb code: 1QJ8 [82]) with color coding of residues which show intermolecular NOEs to DMPC or DHPC molecules. Blue colored residues show NOEs between the residue and both methyl and methylene groups of the hydrophobic tails of DMPC, while red colored residues show NOEs only to methylene groups of DMPC. Residues which show NOEs to the methyl groups of the polar choline headgroup are colored green. For grey residues no intermolecular NOEs were observed. The dotted lines in figure A indicates the boundaries of the central hydrophobic region of the bicelle due to these intermolecular NOEs. The distance between the boundaries is around 2.7 nm. This figure was generated using the program PyMOL [130].

The results in this subsection were published in Lee et al. [124].

## 5.4 Summary and Outlook

Transmembrane proteins are involved in many essential cellular processes as transmembrane transports and cell signaling. Despite the large amount of membrane proteins the number of experimentally determined structures of membrane proteins is very limited. The reason for this is based in the need of a hydrophobic environment for the correct folding of the membrane protein. Since the hydrophobic environment highly increases the size of the total membrane protein complex, this makes it difficult to investigate membrane proteins with solution NMR spectroscopical methods. The most common method is the use of small detergents, which form a micelle around the hydrophobic region of the membrane protein. Nevertheless such micelles show strong differences to the lipid bilayer of a natural membrane



due to their strong curvature and different lateral pressure. Such problems can be solved by the use of small bicelles as a hydrophobic environment which offer the membrane protein a lipid bilayer as an environment while its rim is covered by the detergents.

In the first part of this study the composition of the small bicelles consisting of DMPC and DHPC with a molar ratio of 1 to 2 were investigated. Using the TRACT experiment the overall rotational correlation time of the protein - bicelle complex were estimated as 35 ns and the molecular weight as 60 kDa. 1D- and 2D-NMR experiments were used to show that the DHPC and DMPC molecules are in clearly different and separated structural environments while forming bicelles in aqueous solutions.

In the second part TROSY, TROSY-HNCA [122] and  $^{15}\text{N}$  resolved  $^1\text{H}, ^1\text{H}$ -NOESY experiments were used to assign the resonances of the protein backbone of OmpX in bicelles and to identify possible structural differences to the OmpX protein structure in micelles. The TROSY spectra of OmpX in micelles and bicelles showed significant differences. The  $^{15}\text{N}$  resolved  $^1\text{H}, ^1\text{H}$ -NOESY also showed a high reduction of inter strand NOEs in the extra membrane region between  $\beta$ -strands 3 and 4 and between the  $\beta$ -strands 5 and 6 compared to OmpX in micelles, what could point to partial dissolution of the extra membrane  $\beta$ -strands. In contrast to this, the chemical shift index analysis does not predict a change from  $\beta$ -strand form to unstructured form by the comparison of the structure of OmpX in bicelle and micelle. Due to problems with the aligning of the protein - bicelle complex, it was not possible to achieve a validation of these indications by the measurement of residual dipolar couplings. Therefore the question about the size of the structural differences of OmpX in micelles and bicelles can not yet be finally decided.

In the third part, the interface between the protein OmpX and the lipid-detergent complex was investigated. The intermolecular NOEs in the  $^{15}\text{N}$  resolved  $^1\text{H}, ^1\text{H}$ -NOESY spectra offered direct insights into the contacts between the membrane protein and the lipid-detergent complex. The intermolecular NOEs indicated a 2.7 nm region along the  $\beta$ -barrel which is covered by the hydrophobic side chains of the lipids. To validate this finding a titration with the paramagnetic component Gadolinium-diethylene triamine pentaacetic acid to OmpX in bicelles was conducted to measure the paramagnetic relaxation enhancement (PRE) effect. By measuring the decrease in the residue specific signal intensities after addition of Gd DTPA it is possible to determine the solvent accessibility of the residues. The results of the PRE support the determination of the region of OmpX covered by the hydrophobic part of the lipid-detergent complex via intermolecular NOEs.

The intramolecular NOEs to the  $\beta$ -barrel of the protein originate exclusively from the aliphatic groups of the DMPC lipids, not from the DHPC detergents. This proves that the membrane protein is located in the lipid bilayer and does not contact the DHPC covered rim of the bicelle.

The intramolecular NOEs from the lipid methyl groups are located at a ring roughly around the center of the  $\beta$ -barrel. The deformation of this ring of contacts from the center of the  $\beta$ -barrel could indicate that the membrane protein is not only stabilized by the hydrophobic interactions with the lipid bilayer, but also induces a distortion to the lipid side chains. Additional experiments have to be conducted to investigate this potential distortion effect. The distribution of the methylene and methyl contacts along the  $\beta$ -barrel indicates that in bicelles the lipid are orientated parallel to the  $\beta$ -barrel, what stands in contrast to previous similar studies about OmpX in micelles which showed that the detergents in a micelle are mainly oriented perpendicular to the axis of the  $\beta$ -barrel.

In addition, the  $^{15}\text{N}$  resolved  $^1\text{H},^1\text{H}$ -NOESY spectra showed much more intermolecular NOEs from the choline head groups of DMPC or DHPC molecules to the protein compared to the corresponding measurements of OmpX in micelles. A possible reason for this could be the tighter packing of the head groups in bicelles than in micelles. The polar interactions of the head groups of the lipids to the protein could be an additional cause for structural or functional differences of membrane proteins in bicelles and micelles.

In the future several more projects were proposed to investigate the structural differences of OmpX in bicelle and micelle and the interaction of membrane protein and lipid-detergent complex in more detail:

It would be very interesting to validate the indication that the extra membrane  $\beta$ -strands of OmpX in bicelles could be destabilized compared to its structure in micelles. A way for that would be the measurement of residual dipolar couplings. Even if the first approaches to measure RDCs in detergent-tolerant alignment media failed, perhaps changes in the approaches could lead to a successful measurement. For example, the size of the self-aligning bicelles and therefore the strength of the alignment could be reduced by increasing the DHPC:DMPC molar ratio of 1:3. Another attempt could be conducted using polyacrylamide gels with different functional groups to avoid the precipitation of the lipid molecules. In addition, a fresh sample of DNA-nanotubes without the before observed impurities could also be stable enough to use it as alignment medium in the presence of detergents.

The lateral pressure in the lipid bilayer of the bicelles could be investigated by comparisons of bicelles consisting of different lipids. Possible lipids could be 1,2-dilauroyl-sn-glycero-3-phosphatidylcholine (DLPC) or 1,2-dipalmitoyl-sn-glycero-3-phosphatidylcholine (DPPC), which have side chains with two  $\text{CH}_2$  groups less, respectively, more than DMPC. The different lengths of these lipids should have an effect on the coverage of the hydrophobic region of the  $\beta$ -barrel and could also give interesting insights about the potential distortion effect of the membrane protein on its lipid environment.

## Chapter 6

# Appendix

### Table of Abbreviations

CCR	cross-correlated relaxation
DHPC	1,2-dihexanoyl-sn-glycero-3-phosphocholin
DIDC	direct interpretation of dipolar couplings
DLPC	1,2-dilauroyl-sn-glycero-3-phosphocholin
DMPC	1,2-dimysteroyl-sn-glycero-3-phosphocholin
DPPC	1,2-dipalmitoyl-sn-glycero-3-phosphocholin
EXCSY	exchange spectroscopy
HR-MAS	high-resolution magic angle spinning
NMR	nuclear magnetic resonance
NOE	nuclear Overhauser effect
NOESY	nuclear Overhauser effect spectroscopy
pdb	protein data bank
ppm	parts per million
RACT	relaxation-allowed coherence transfer
RDC	residual dipolar coupling
SCRM	self-consistent RDC-based model free
TOCSY	total correlation spectroscopy
TRACT	TROSY for rotational correlation times
TROSY	transverse relaxation optimized spectroscopy

**Table 6.1:** Experimentally determined CCR rates of NH -  $C\alpha H\alpha$  pairs in the protein backbone of ubiquitin

Residue	CCR [Hz]	Error [Hz]
3	-9.7	1.6
4	-15.7	1.5
5	-14.5	2.2
6	-13.7	1.7
7	-11.7	1.2
8	-2.8	2.5
9	-9.9	5.5
11	-6.7	1.1
12	-13.1	3.4
13	-17.4	7.0
14	-14.4	1.6
15	-14.4	1.3
17	-13.1	1.2
18	-14.8	1.4
20	-7.5	0.6
21	-4.9	0.8
22	-10.1	1.5
23	-1.8	1.8
25	-6.0	0.9
27	-2.9	0.8
28	-3.9	0.9
29	-5.5	0.8
30	-4.6	1.0
31	-1.3	1.1
32	-2.1	0.7
33	-6.8	0.7
34	-13.1	1.0
36	-10.4	0.9
39	-4.8	0.7
40	-12.0	0.8
41	-11.4	1.1
42	-13.3	2.6
43	-14.9	2.1
44	-15.0	2.3
45	-12.6	1.4

**Table 6.1:** – continued from last page

Residue	CCR [Hz]	Error [Hz]
46	-3.7	7.0
48	-13.5	1.0
50	-7.9	1.7
51	-13.6	2.4
54	-14.2	1.1
55	-12.3	1.7
56	-0.2	1.3
57	-1.6	0.9
58	-2.9	0.8
59	-12.1	0.7
60	-2.0	1.1
61	-9.4	1.2
62	-12.4	1.2
63	2.1	1.4
65	-5.6	0.7
66	-9.3	2.0
67	-14.9	2.3
68	-15.0	2.0
70	-14.4	2.1

## Pulseprograms

### Pulseprogram for the Measurement of NH - $C\alpha H\alpha$ CCR Rates in the Backbone

```
# 1 "/opt/topspin21/exp/stan/nmr/lists/pp/user/hahn-ccr2.d1"
```

```
;p11 : power for 1H hard pulse
;p12 : power for 180 13C p4
;p13 : power for 15N hard pulse
;p17 : power for 90 13C p3
;p111 : power for 1H DIPSI decoupling
;p112 : power for 13C SEDUCE decoupling
;p113 : power for 15N WALTZ decoupling
;sp12 : power for C0 decoupling pulse (p12)
;p1 : 90 degree hard pulse 1H
;p2 : 180 degree 1H
;p3 : 90 degree hard pulse 13C
;p4 : 180deg 13C: Sqrt(3)/(OmegaHz[C0-Ca]*2)
;p5 : 90 degree hard pulse 15N
;p6 : 180 degree 15N
;p12 : 180 13C0 off-resonance pulse seduce1
;pcpd1 : 90 degree cpd-pulse 1H (DIPSI, 80us)
;pcpd2 : 90 degree seduce1 (SEDUCE, 700us)
;pcpd3 : 90 degree cpd-pulse 15N (WALTZ, 160us)
;p20 : 1000u (cleaning Gradient)
;p21 : 700u (Gradient in first INEPT)
;p22 : 1000u (Gradient for 1st z-filter)
;p23 : 800u (Gradient for 2nd z-filter)
;p24 : 800u (Gradient for 3rd z-filter)
;p25 : 1000u (Gradient for 4th z-filter)
;p26 : 800u (Gradient in WATERGATE)
;gpz0 : 80 %
;gpz1 : 25 %
;gpz2 : -70 %
;gpz3 : 25 %
;gpz4 : 28 %
;gpz5 : 60 %
;gpz6 : 75 %
```

```

;d1      : relaxation delay
;d2      : 1H-15N inept delay (2.3ms)
;d4      : delay for in-phase coh. (5.5ms)
;d5      : for 3-9-19, d5=1/d, d to next null (Hz)
;d12     : 1/2 constant-time 15N (11ms)
;d13     : 1/2Jcacb ct 13C (14.42m)
;d29     : calculated during runtime

# 1 "/opt/topspin21/exp/stan/nmr/lists/pp/user/Avance_dl.incl" 1
# 56 "/opt/topspin21/exp/stan/nmr/lists/pp/user/hahn-ccr2.dl" 2

define delay INEPT_1
define delay INEPT_W
define delay bigT

"p2=2*p1"
"p6=2*p5"

"in0=inf1/2"
"in10=inf2/2"
"in11=in10"

"d0=0.0u"
"d3=d5/2-p5/2"
"d6=d12*2-d4"
;"d10=in10/2-p3*2/3.14159-8u"
"d29=d12-d0"
"d10=0.0u"
"bigT=d13-16u"
"d11=d13-16u"
"INEPT_1=d2-p21-200u"
"INEPT_W=d2-(p26+200u+p1*2.3846+d5*2.5)"

"l2 = 1"
"l3 = td1/2"
"l13 = td2/2"

;aqseq 312

```

```

# 1 "mc_line 96 file  ;(continued in next line)
/opt/topspin21/exp/stan/nmr/lists/pp/user/hahn-ccr2.dl ;(continued in next line)
dc-measurement inserted automatically"
    dccorr
# 96 "/opt/topspin21/exp/stan/nmr/lists/pp/user/hahn-ccr2.dl"
1  10u ze
2  10u
3  10u
   10u
4  10u
   10u
   10u
   10u
5  10u
   10u
6  20u
10 10m do:f3
    20u setnmr3^0 setnmr0^34^32^33 ctrlgrad 7
    d1
    "d29=d12-d0"
    10u p11:f1
    10u p12:f2
    10u p13:f3
    20u setnmr3|0 setnmr0|34|32|33 ctrlgrad 0
    (p5 ph20):f3
    10u p20:gp0 190u
    10m
;-----First INEPT
    (p1 ph20):f1
    10u p21:gp1 190u
    INEPT_1
    (refalign (p2 ph20):f1 center (p6 ph20):f3)
    10u p21:gp1 190u
    INEPT_1
    (p1 ph21):f1
;-----Z-Filter
    10u p22:gp2 190u
    10u p111:f1
    10u p112:f2
    10u cpds2:f2

```



```

;-----15N evolution plus J(NC) evolution
  (p5 ph1):f3
  (refalign (d12 d0):f3 lalign (d4 5u cpds1):f1)
  (refalign (p6 ph20):f3 center (4u do 4u pl2 p4 ph20 4u pl12 4u cpds2):f2)
  d29
  (p5 ph20):f3
;-----Z-Filter
  10u p23:gp3 190u
  4u do:f2
  4u pl2:f2
  4u do:f1
;-----CCR evolution block
if "l2 %2 == 1" goto 31
  (center (p5 ph5):f3 (p3 ph4):f2)
goto 32
31 (center (p5 ph3):f3 (p3 ph2):f2)
32 4u pl12:f2
  4u cpds2:f2
  d10
  bigT
  4u do:f2
  4u pl2:f2
  (center (p6 ph20):f3 (p4 ph20):f2)
  4u pl12:f2
  4u cpds2:f2
  d11
  4u do:f2
  4u pl2:f2
  (center (p5 ph20):f3 (p3 ph20):f2)
;-----Z-Filter
  10u cpds1:f1
  10u pl12:f2
  10u cpds2:f2
  10u p24:gp4 190u
;-----Second INEPT
  (p5 ph20):f3
  (refalign (d12 p6 ph20 d12):f3 ;(continued in next line)
  center (4u do 4u pl2 p4 ph20 4u pl12 4u cpds2):f2 lalign (d6 5u do):f1)
  (p5 ph20):f3
  10u do:f2

```

```

10u pl2:f2
;-----Z-Filter
10u p25:gp5 190u
10u pl1:f1
;-----Third INEPT
(p1 ph20):f1
10u p26:gp6 190u
INEPT_W
(p1*0.2308 ph21 d5 p1*0.6923 ph21 d5 p1*1.4615 ph21):f1
(d3 p6 ph20 d3):f3
(p1*1.4615 ph23 d5 p1*0.6923 ph23 d5 p1*0.2308 ph23):f1
10u p26:gp6 190u
INEPT_W pl13:f3 setnmr3^0 setnmr0^34^32^33 ctrlgrad 7
;-----Acquisition
go=2 ph31 cpd3:f3
1m do:f3 wr #0 if #0 zd
10u iu2
lo to 2 times 2
10u ip1
lo to 3 times 2
10u id0
lo to 4 times 13
10u rd0
10u rp1
10u ip2
10u ip4
lo to 5 times 2
10u id10
10u dd11
lo to 6 times 113
10u do:f1
10u do:f3
10u do:f2
10u setnmr3^0 setnmr0^34^32^33 ctrlgrad 7
exit

ph1 =0 2
ph2 =0 0 2 2
ph3 =0 0 0 0 2 2 2 2
ph4 =1 1 3 3

```

```

ph5 =1 1 1 1 3 3 3 3
ph31=0 2 2 0 2 0 0 2
ph20=0
ph21=1
ph22=2
ph23=3

```

### Pulseprogram for the Measurement of NH - NH CCR Rates between $\beta$ -Strands

```
# 1 "/opt/topspin/exp/stan/nmr/lists/pp/user/test.dl"
```

```

;p11 : power for 1H
;p12 : power for 13C
;p13 : power for 15N
;p113 : power for 15N waltz16 decoupling
;p1 : 90 degree hard pulse 1H
;p3 : 90 degree hard pulse 13C
;p4 : 180 degree hard 13C pulse (225d for 5/600)
;p5 : 90 degree hard pulse 15N
;pcpd3 : 90 deg cpd-pulse15N(waltz16,160u)
;d1 : relaxation delay
;d2 : INEPT delay (~2.7m)
;d5 : delay for 3-9-19=1/(Hz between nulls)
;in0 : 1/(2 SW) (Hz)
;p21 : 500u (Gradient in first INEPT)
;p22 : 500u (Gradient for z-filter)
;p23 : 1m (Gradient for second INEPT)
;gpz1 : 19%
;gpz2 : 30%
;gpz3 : 65%

```

```
# 1 "/opt/topspin/exp/stan/nmr/lists/pp/user/Avance_kw.incl" 1
```

```
# 35 "/opt/topspin/exp/stan/nmr/lists/pp/user/test.dl" 2
```

```

define delay INEPT_W
define delay INEPT_D
define delay INEPT_1
define delay INEPT_2
"p2=2*p1"

```

"p6=2\*p5"

"in0=inf1/4"

"in30=in0"

"in10=inf1/4"

"in31=in10"

"d0=d8/4"

"d30=d8/4-p11-10u-p1"

"d10=d8/4"

"d31=d8/4-p11-10u-p1"

"INEPT\_D=d2-p21-210u-p11-10u"

"INEPT\_W=d2-(p23+210u+p11+10u)"

"INEPT\_1=d2-p22-210u-2\*p11-20u"

"INEPT\_2=d2-p24-210u-p11-10u"

"d11=p11"

aqseq 312

```
# 1 "mc_line 70 file ;(continued in next line)
/opt/topspin/exp/stan/nmr/lists/pp/user/test.dl ;(continued in next line)
expanding definition part of mc command before ze"
; dimension 3 aq-mode (F2) States-TPPI (F1) States-TPPI F2->F1
define delay MCWRK
define delay MCREST
define loopcounter ST1CNT
"ST1CNT = td2 / (2)"
define loopcounter ST2CNT
"ST2CNT = td1 / (2)"
"MCWRK = 0.250000*1m"
"MCREST = 1m - 1m"
    dccorr
# 70 "/opt/topspin/exp/stan/nmr/lists/pp/user/test.dl"
1 10u ze
# 1 "mc_line 70 file ;(continued in next line)
/opt/topspin/exp/stan/nmr/lists/pp/user/test.dl ;(continued in next line)
expanding definition of mc command after ze"
# 71 "/opt/topspin/exp/stan/nmr/lists/pp/user/test.dl"
# 1 "mc_line 71 file ;(continued in next line)
/opt/topspin/exp/stan/nmr/lists/pp/user/test.dl ;(continued in next line)
```

```

expanding start label for mc command"
2 MCWRK do:f3
LBLSTS2, MCWRK * 2
LBLF2, MCWRK
  MCREST
# 72 "/opt/topspin/exp/stan/nmr/lists/pp/user/test.d1"
  d1 pl1:f1
  20u pl3:f3
  20u setnmr3|0 setnmr0|34|32|33 ctrlgrad 0
  10u
  (p5 ph20):f3
  10u p20:gp0 200u
  1m
;-----First INEPT
  (p11:sp1 ph26:r):f1
  10u
  (p1 ph20):f1
  10u p21:gp1 200u
  INEPT_D
  (p11:sp2 ph26:r):f1
  10u
  (center(p2 ph20):f1 (p6 ph20):f3)
  10u
  (p11:sp2 ph26:r):f1
  10u p21:gp1 200u
  INEPT_D
;-----First 15N evolution plus RDC evolution
  (p5 ph1):f3
  d0
  (p6 ph20):f3
  d30
  (p11:sp2 ph26:r):f1
  10u
  (p2 ph20):f1
  10u
  (p11:sp2 ph26:r):f1
  d30
  (p6 ph20):f3
  d0
  (p5 ph3):f3

```

```

;-----Second INEPT
  2u
  (p2 ph20):f1
  10u p23:gp3 200u
  INEPT_W
  (p11:sp2 ph26:r):f1
  10u
  (center (p2 ph20):f1 (p6 ph20):f3)
  10u
  (p11:sp2 ph26:r):f1
  10u p23:gp3 200u
  INEPT_W
  (p2 ph20):f1
  2u
;-----Third INEPT
  (p1 ph21):f1
  10u
  (p11:sp1 ph27:r):f1
  10u p22:gp2 200u
  INEPT_1
  (p11:sp2 ph26:r):f1
  10u
  (center(p2 ph20):f1 (p6 ph20):f3)
  10u
  (p11:sp2 ph26:r):f1
  10u p22:gp2 200u
  INEPT_1
  10u
  d11
;-----Second 15N evolution plus RDC evolution
  (p5 ph20):f3
  d10
  (p6 ph20):f3
  d31
  (p11:sp2 ph26:r):f1
  10u
  (p2 ph20):f1
  10u
  (p11:sp2 ph26:r):f1
  d31

```

```

(p6 ph20):f3
d10
(p5 ph2):f3
;-----Fourth INEPT
10u p24:gp4 200u
INEPT_2
(p11:sp2 ph26:r):f1
10u
(center (p2 ph20):f1 (p6 ph20):f3)
10u
(p11:sp2 ph26:r):f1
10u p24:gp4 200u
INEPT_2 pl13:f3 setnmr3^0 setnmr0^34^32^33 ctrlgrad 7
;-----Acquisition
go=2 ph31 cpd3:f3
# 1 "mc_line 161 file ;(continued in next line)
/opt/topspin/exp/stan/nmr/lists/pp/user/test.dl ;(continued in next line)
expanding mc command in line"
MCWRK do:f3 wr #0 if #0 zd ip1
lo to LBLSTS2 times 2
MCWRK dd0 MCWRK id30
lo to LBLF2 times ST2CNT
MCWRK
# 164 "/opt/topspin/exp/stan/nmr/lists/pp/user/test.dl"
10u do:f1
10u do:f2
10u do:f3
10u setnmr3^0 setnmr0^34^32^33 ctrlgrad 7
exit

ph1 =0 2
ph2 =0 0 2 2
ph3 =0 0 0 0 2 2 2 2
ph31=2 0 0 2 0 2 2 0
ph20=0
ph21=1
ph22=2
ph23=3
ph26=2
ph27=3

```

**Pulseprogram for the Measurement of  $C\alpha^1H\alpha^1 - C\alpha^2H\alpha^2$   
CCR Rates between  $\beta$ -Strands**

```
# 1 "/opt/topspin/exp/stan/nmr/lists/pp/user/ca_hc2_ccr.kw"
```

```
;p11 : power for 1H
;p13 : power for 15N
;p12 : power for 13C hard
;p112 : power for 13C GARP decoupling
;p1 : 90 degree hard pulse 1H
;p3 : 90 degree hard pulse 13C
;p4 : 13C pulse, 225deg for 500/600, 180deg for 750/900
;p5 : 90 degree hard pulse 15N
;d1 : relaxation delay
;d2 : 1H-13C INEPT delay (1.7m)
;d3 : 1/JCH (3.4m) and 0 for ref and ccr
;d4 : n/JCH (~17m)
;in0 : 1/2*SW(in Hz)
;pcpd2 : 90 deg cpd-pulse 13C (~85us)
"p20=1m"
"p21=700u"
"p22=200u"
"p23=300u"
"p24=500u"
"p25=600u"
```

```
# 1 "/opt/topspin/exp/stan/nmr/lists/pp/user/Avance_dl.incl" 1
```

```
# 29 "/opt/topspin/exp/stan/nmr/lists/pp/user/ca_hc2_ccr.kw" 2
```

```
define delay INEPT_1
define delay INEPT_2
define delay INEPT_3
define delay CCRA
define delay CCRB
define delay DELTA1
define delay DELTA2
```



```

"p2=p1*2"
"p4=p3*2"

"in0=inf1/2"
"d0=in0/2-p1-p3*2/3.141592"

"INEPT_1=d2-(p21+210u)"
"INEPT_2=d2-(p26+210u)-8u"
"INEPT_3=d2-(p27+210u)-8u"
"CCRA=(d8+d3)/4"
"CCRB=(d8-d3)/4"
"DELTA1=d4*0.5-(p24+210u)-p11*0.45"
"DELTA2=d4*0.5-d2-(p25+210u)-p11*0.45"

# 1 "mc_line 67 file ;(continued in next line)
/opt/topspin/exp/stan/nmr/lists/pp/user/ca_hc2_ccr.kw ;(continued in next line)
expanding definition part of mc command before ze"
define delay MCWRK
define delay MCREST
define loopcounter ST1CNT
"ST1CNT = td1 / (2)"
"MCWRK = 0.333333*1m"
"MCREST = 1m - 1m"
    dccorr
# 67 "/opt/topspin/exp/stan/nmr/lists/pp/user/ca_hc2_ccr.kw"
1 10u ze
# 1 "mc_line 67 file ;(continued in next line)
/opt/topspin/exp/stan/nmr/lists/pp/user/ca_hc2_ccr.kw ;(continued in next line)
expanding definition of mc command after ze"
# 68 "/opt/topspin/exp/stan/nmr/lists/pp/user/ca_hc2_ccr.kw"
    10u
# 1 "mc_line 69 file ;(continued in next line)
/opt/topspin/exp/stan/nmr/lists/pp/user/ca_hc2_ccr.kw ;(continued in next line)
expanding start label for mc command"
2 MCWRK do:f2
LBLSTS1, MCWRK
LBLF1, MCWRK
    MCREST
# 70 "/opt/topspin/exp/stan/nmr/lists/pp/user/ca_hc2_ccr.kw"
    20u pl9:f1

```

```

10u setnmr3^0 setnmr0^34^32^33 ctrlgrad 7
d1 cw:f1
10u do:f1
20u p11:f1
10u p12:f2
20u p113:f3
20u setnmr3|0 setnmr0|34|32|33 ctrlgrad 0
1m
10u p20:gp0 200u
1m
;-----first INEPT
(p1 ph20):f1
10u p21:gp1 200u
INEPT_1
(center (p2 ph20):f1 (p4 ph21):f2)
10u p21:gp1 200u
INEPT_1
(p1 ph21):f1
10u p22:gp2 200u
; (p1 ph20):f1
10u cpds3:f3
;-----13C evolution
(p3 ph1):f2
4u p114:f2
4u cpds4:f2
(d0 p2 ph20 d0):f1
4u do:f2
4u p12:f2
(p3 ph2):f2
10u do:f3
; (p1 ph22):f1
10u p23:gp3 200u
;-----First RACT step
(p1 ph20):f1
10u p24:gp4 200u
DELTA1
(center (p11:sp11 ph20):f1 (p4 ph21):f2)
10u p24:gp4 200u
DELTA1 p11:f1
(center (p1 ph3):f1 (p3 ph4):f2)

```

```

;-----Second INEPT
  4u pl14:f2
  4u cpds4:f2
  10u p26:gp6 200u
  INEPT_2
  4u do:f2
  4u pl2:f2
  2u
  (center (p2 ph20):f1 (p4 ph21):f2)
  2u
  4u pl14:f2
  4u cpds4:f2
  10u p26:gp6 200u
  INEPT_2
  4u do:f2
  4u pl2:f2
;-----CCR evolution block
  (p1 ph5):f1
  CCRA
  (p4 ph21):f2
  CCRB
  (p2 ph20):f1
  CCRA
  (p4 ph21):f2
  CCRB
  (p1 ph6):f1
;-----Third INEPT
  4u pl14:f2
  4u cpds4:f2
  10u p27:gp7 200u
  INEPT_3
  4u do:f2
  4u pl2:f2
  2u
  (center (p2 ph20):f1 (p4 ph21):f2)
  2u
  4u pl14:f2
  4u cpds4:f2
  10u p27:gp7 200u
  INEPT_3

```

```

4u do:f2
4u pl2:f2
(p1 ph7):f1
;-----Second RACT step
10u p25:gp5 200u
DELTA2
(center (p11:sp11 ph20):f1 (p4 ph21):f2)
10u p25:gp5 200u
DELTA2 pl12:f2 setnmr3^0 setnmr0^34^32^33 ctrlgrad 7
;-----acquisition
go=2 ph31 cpd2:f2
# 1 "mc_line 160 file ;(continued in next line)
/opt/topspin/exp/stan/nmr/lists/pp/user/ca_hc2_ccr.kw ;(continued in next line)
expanding mc command in line"
MCWRK do:f2 wr #0 if #0 zd ip1
lo to LBLSTS1 times 2
MCWRK id0
lo to LBLF1 times ST1CNT
MCWRK
# 161 "/opt/topspin/exp/stan/nmr/lists/pp/user/ca_hc2_ccr.kw"
10u do:f1
10u do:f2
10u do:f3
10u setnmr3^0 setnmr0^34^32^33 ctrlgrad 7
exit

ph1= 0 2
ph2= 0 0 2 2
ph3= 0 0 0 0 0 0 0 0
      2 2 2 2 2 2 2 2
ph4= 1 1 1 1 3 3 3 3
ph5= 0 0 0 0 0 0 0 0
      0 0 0 0 0 0 0 0
      2 2 2 2 2 2 2 2
      2 2 2 2 2 2 2 2
ph6= 0 0 0 0 0 0 0 0
      0 0 0 0 0 0 0 0
      0 0 0 0 0 0 0 0
      0 0 0 0 0 0 0 0
      2 2 2 2 2 2 2 2

```

```

      2 2 2 2 2 2 2 2
      2 2 2 2 2 2 2 2
      2 2 2 2 2 2 2 2
ph7=  0 0 0 0 0 0 0 0
      0 0 0 0 0 0 0 0
      0 0 0 0 0 0 0 0
      0 0 0 0 0 0 0 0
      0 0 0 0 0 0 0 0
      0 0 0 0 0 0 0 0
      0 0 0 0 0 0 0 0
      0 0 0 0 0 0 0 0
      0 0 0 0 0 0 0 0
      2 2 2 2 2 2 2 2
      2 2 2 2 2 2 2 2
      2 2 2 2 2 2 2 2
      2 2 2 2 2 2 2 2
      2 2 2 2 2 2 2 2
      2 2 2 2 2 2 2 2
      2 2 2 2 2 2 2 2
      2 2 2 2 2 2 2 2
ph31=2 0 0 2 2 0 0 2
      2 0 0 2 2 0 0 2
      0 2 2 0 0 2 2 0
      0 2 2 0 0 2 2 0
      0 2 2 0 0 2 2 0
      0 2 2 0 0 2 2 0
      2 0 0 2 2 0 0 2
      2 0 0 2 2 0 0 2
ph20=0
ph21=1
ph22=2
ph23=3

```

**Pulseprogram for the Measurement of  $C\alpha^x H\alpha^x - H\alpha^1 H\alpha^2$   
CCR Rates between  $\beta$ -Strands**

```
# 1 "/opt/topspin/exp/stan/nmr/lists/pp/user/ract_b.kw"
```

```
;p11 : power for 1H
;p13 : power for 15N
;p12 : power for 13C hard
```

```
;pl12 : power for 13C GARP decoupling
;sp12 : power for selective C=O pulse
;p1    : 90 degree hard pulse 1H
;p3    : 90 degree hard pulse 13C
;p4    : 13C pulse, 225deg for 500/600, 180deg for 750/900
;p5    : 90 degree hard pulse 15N
;pcpd2 : 90 deg cpd-pulse 13C (~85us)
;p12   : shaped 180 pulse for CO decoupling (80u)
;spnam12: shape for selective C=O pulse (gauss.128_5)
;p21   : 1m (Gradient in first INEPT)
;p22   : 800u (Gradient in first INEPT)
;p23   : 1m (Gradient for z-filter)
;p26   : 1m (Gradient for second INEPT)
;gpz1  : 19%
;gpz2  : 30%
;gpz3  : 65%
;gpz6  : 15%
;d1    : relaxation delay
;d2    : 1H-13C INEPT delay (1.7m)
;d6    : first CCR mixing
;d7    : second CCR mixing
;in0   : 1/2*SW(in Hz)

# 1 "/opt/topspin/exp/stan/nmr/lists/pp/user/Avance_dl.incl" 1
# 41 "/opt/topspin/exp/stan/nmr/lists/pp/user/ract_b.kw" 2

define delay INEPT_1
define delay INEPT_2
define delay RACT1
define delay RACT2

"p2=p1*2"
"p6=p5*2"
"p4=p3*2"

"in0=inf1/2"
"d0=in0/2-p3*2/3.14159"

"INEPT_1=d2-(p21+210u)"
"INEPT_2=d2-(p26+210u)"
```

```

"RACT1=d6-(p25+210u)-p11*0.45-10u"
"RACT2=d7-(p26+210u)-p11*0.45-10u"

# 1 "mc_line 71 file ;(continued in next line)
/opt/topspin/exp/stan/nmr/lists/pp/user/ract_b.kw ;(continued in next line)
expanding definition part of mc command before ze"
define delay MCWRK
define delay MCREST
define loopcounter ST1CNT
"ST1CNT = td1 / (2)"
"MCWRK = 0.333333*1m"
"MCREST = 1m - 1m"
    dccorr
# 71 "/opt/topspin/exp/stan/nmr/lists/pp/user/ract_b.kw"
1 10u ze
# 1 "mc_line 71 file ;(continued in next line)
/opt/topspin/exp/stan/nmr/lists/pp/user/ract_b.kw ;(continued in next line)
expanding definition of mc command after ze"
# 72 "/opt/topspin/exp/stan/nmr/lists/pp/user/ract_b.kw"
    10u
# 1 "mc_line 73 file ;(continued in next line)
/opt/topspin/exp/stan/nmr/lists/pp/user/ract_b.kw ;(continued in next line)
expanding start label for mc command"
2 MCWRK
LBLSTS1, MCWRK
LBLF1, MCWRK
    MCREST
# 74 "/opt/topspin/exp/stan/nmr/lists/pp/user/ract_b.kw"
    10u do:f2
    20u pl1:f1
    10u setnmr3^0 setnmr0^34^32^33 ctrlgrad 7
    d1 pl2:f2
    20u pl3:f3
    20u setnmr3|0 setnmr0|34|32|33 ctrlgrad 0
    (p3 ph20):f2
    10u p20:gp0 200u
    10m
;-----First INEPT
    (p1 ph20):f1
    10u p21:gp1 200u

```

```

INEPT_1
(center (p2 ph20):f1 (p4 ph20):f2)
10u p21:gp1 200u
INEPT_1
(p1 ph21):f1
10u p22:gp2 200u
;-----13C evolution
(p1 ph20):f1
2u
(refalign(p3 ph1 d0 d0 p3 ph2):f2 center(p2 ph20):f1 center(p6 ph20):f3)
2u
(p1 ph22):f1
10u p23:gp3 200u
;-----First RACT step
(p1 ph20):f1
10u p24:gp4 200u
RACT1
10u
(center (p11:sp11 ph20):f1 (p4 ph20):f2)
10u p24:gp4 200u
RACT1 p11:f1
10u
;-----1Hy2Hz --> 1Hz2Hy and removing diagonal
(center (p1 ph3):f1 (p3 ph4):f2)
;-----Second RACT step
10u p25:gp5 200u
RACT2
10u
(center (p11:sp11 ph20):f1 (p4 ph20):f2)
10u p25:gp5 200u
RACT2 p11:f1
10u
;-----Second INEPT
(p1 ph5):f1
10u p26:gp6 200u
INEPT_2
(center (p2 ph20):f1 (p4 ph20):f2)
10u p26:gp6 200u
INEPT_2 p112:f2 setnmr3^0 setnmr0^34^32^33 ctrlgrad 7
;-----Acquisition

```



```

    go=2 ph31 cpd2:f2
# 1 "mc_line 127 file ;(continued in next line)
/opt/topspin/exp/stan/nmr/lists/pp/user/ract_b.kw ;(continued in next line)
expanding mc command in line"
    MCWRK do:f2 wr #0 if #0 zd ip1
    lo to LBLSTS1 times 2
    MCWRK id0
    lo to LBLF1 times ST1CNT
    MCWRK
# 128 "/opt/topspin/exp/stan/nmr/lists/pp/user/ract_b.kw"
    10u do:f1
    10u do:f2
    10u do:f3
    10u setnmr3^0 setnmr0^34^32^33 ctrlgrad 7
exit

ph1= 0 2
ph2= 0 0 2 2
ph3= 0 0 0 0 0 0 0 0
      0 0 0 0 0 0 0 0
      2 2 2 2 2 2 2 2
      2 2 2 2 2 2 2 2
ph4= 0 0 0 0 0 0 0 0
      2 2 2 2 2 2 2 2
ph5= 1 1 1 1 3 3 3 3
ph31=2 0 0 2

ph20=0
ph21=1
ph22=2
ph23=3

```

**Pulseprogram for the Measurement of inter methyl CH - CH CCR Rates  
in the hydrophobic Core (using NOE Transfers)**

```

# 1 "/opt/topspin/exp/stan/nmr/lists/pp/user/methylccr_new.ms"

;p11 : power for 1H
;p13 : power for 15N
;p12 : power for 13C hard

```

```
;pl12 : power for 13C GARP decoupling
;sp12 : power for selective C=O pulse
;p1    : 90 degree hard pulse 1H
;p3    : 90 degree hard pulse 13C
;p4    : 13C pulse, 225deg for 500/600, 180deg for 750/900
;p5    : 90 degree hard pulse 15N
;pcpd2 : 90 deg cpd-pulse 13C (~85us)
;p12   : shaped 180 pulse for CO decoupling (80u)
;spnam12: shape for selective C=O pulse (gauss.128_5)
;p21   : 500u (Gradient in first INEPT)
;p22   : 800u (Gradient in first INEPT)
;p23   : 1m (Gradient for z-filter)
;p24   : 1m (Gradient for second INEPT)
;gpz1  : 19%
;gpz2  : 30%
;gpz3  : 65%
;gpz4  : 15%
;d1    : relaxation delay
;d2    : 1H to 13C (1.7m)
;d8    : NOE mixing (600m)
;d9    : CCR time (25m)
;d13   : 1m (ref) or 0 (CCR)
;in0   : 1/2*SW(in Hz)
;in10  : 1/2*SW(in Hz)

# 1 "/opt/topspin/exp/stan/nmr/lists/pp/user/Avance_kw.incl" 1
# 44 "/opt/topspin/exp/stan/nmr/lists/pp/user/methylccr_new.ms" 2

define delay INEPT_1
define delay INEPT_2
define delay INEPT_3
define delay INEPT_4

"in0=inf1/2"
"in10=inf2/2"

"p2=p1*2"
"p4=p3*2"
```

```
"d0=in0/2-p3*2/3.1415"
"d10=in10/2-p3*2/3.1415"
"d7=d8-(p24+210u)"
"d6=d8-(p27+210u)"
"d11=(d9+d13)/4"
"d12=(d9-d13)/4"
"INEPT_1=d2-(p21+210u)"
"INEPT_2=d2-(p29+210u)"
"INEPT_3=d2-(p26+210u)"
"INEPT_4=d2-(p28+210u)"
```

```
aqseq 312
```

```
# 1 "mc_line 86 file ;(continued in next line)
/opt/topspin/exp/stan/nmr/lists/pp/user/methylccr_new.ms ;(continued in next line)
expanding definition part of mc command before ze"
; dimension 3 aq-mode (F2) States-TPPI (F1) States-TPPI F2->F1
define delay MCWRK
define delay MCREST
define loopcounter ST1CNT
"ST1CNT = td2 / (2)"
define loopcounter ST2CNT
"ST2CNT = td1 / (2)"
"MCWRK = 0.142857*1m"
"MCREST = 1m - 1m"
    dccorr
# 86 "/opt/topspin/exp/stan/nmr/lists/pp/user/methylccr_new.ms"
1 10u ze
# 1 "mc_line 86 file ;(continued in next line)
/opt/topspin/exp/stan/nmr/lists/pp/user/methylccr_new.ms ;(continued in next line)
expanding definition of mc command after ze"
# 87 "/opt/topspin/exp/stan/nmr/lists/pp/user/methylccr_new.ms"
    10u
# 1 "mc_line 88 file ;(continued in next line)
/opt/topspin/exp/stan/nmr/lists/pp/user/methylccr_new.ms ;(continued in next line)
expanding start label for mc command"
2 MCWRK
LBLSTS2, MCWRK
LBLF2, MCWRK * 3
LBLSTS1, MCWRK
```

LBLF1, MCWRK

MCREST

# 89 "/opt/topspin/exp/stan/nmr/lists/pp/user/methylccr\_new.ms"

10u do:f2

20u pl1:f1

10u setnmr3^0 setnmr0^34^32^33 ctrlgrad 7

d1 pl2:f2

20u ;pl3:f3

20u setnmr3|0 setnmr0|34|32|33 ctrlgrad 0

(p3 ph20):f2

10u p20:gp0 200u

1m

;-----First INEPT

(p1 ph20):f1

10u p21:gp1 200u

INEPT\_1

(center (p2 ph20):f1 (p4 ph20):f2)

10u p21:gp1 200u

INEPT\_1

(p1 ph21):f1

10u p22:gp2 200u

;-----13C evolution

(refalign (p3 ph1 d0 d0 p3 ph20):f2 center (p2 ph20):f1)

;-----first NOE step

10u p24:gp4 200u

d7

;-----Second INEPT

(p1 ph20):f1

10u p26:gp6 200u

INEPT\_3

(center (p2 ph20):f1 (p4 ph20):f2)

10u p26:gp6 200u

INEPT\_3

(p1 ph2):f1

10u p23:gp3 200u

;-----CCR evolution block

(p3 ph20):f2

d11

(p2 ph20):f1

d12

```

(p4 ph20):f2
d11
(p2 ph20):f1
d12
(p3 ph21):f2
;-----Third INEPT
10u p25:gp5 200u
(p1 ph3):f1
10u p28:gp8 200u
INEPT_4
(center (p2 ph20):f1 (p4 ph20):f2)
10u p28:gp8 200u
INEPT_4
(p1 ph20):f1
;-----Second NOE step
10u p27:gp7 200u
d6
(refalign (p3 ph20 d10 d10 p3 ph4):f2 center (p2 ph20):f1)
10u p30:gp10 200u
(p1 ph20):f1
;-----Fourth INEPT
10u p29:gp9 200u
INEPT_2
(center (p2 ph20):f1 (p4 ph20):f2)
10u p29:gp9 200u
INEPT_2 pl12:f2 setnmr3^0 setnmr0^34^32^33 ctrlgrad 7
;-----Acquisition
go=2 ph31 cpd2:f2
# 1 "mc_line 154 file ;(continued in next line)
/opt/topspin/exp/stan/nmr/lists/pp/user/methylccr_new.ms ;(continued in next line)
expanding mc command in line"
MCWRK do:f2 wr #0 if #0 zd ip1
lo to LBLSTS2 times 2
MCWRK id0
lo to LBLF2 times ST2CNT
MCWRK rp1 MCWRK rd0 MCWRK dp4
lo to LBLSTS1 times 2
MCWRK id10
lo to LBLF1 times ST1CNT
MCWRK

```

```
# 157 "/opt/topspin/exp/stan/nmr/lists/pp/user/methylccr_new.ms"
 10u do:f1
 10u do:f2
 10u do:f3
 10u setnmr3^0 setnmr0^34^32^33 ctrlgrad 7
exit
```

```
ph1 =0 2
ph2 =1 1 1 1 1 1 1 1
      3 3 3 3 3 3 3 3
ph3 =1 1 1 1 3 3 3 3
ph4 =0 0 2 2
ph31=2 0 0 2 0 2 2 0
      0 2 2 0 2 0 0 2
ph20=0
ph21=1
ph22=2
ph23=3
```

### Pulseprogram for the Measurement of inter methyl CH - CH CCR Rates in the hydrophobic Core (using RACT Transfers)

```
;p11 : power for 1H
;p13 : power for 15N
;p12 : power for 13C hard
;p112 : power for 13C GARP decoupling
;sp12 : power for selective C=O pulse
;p1 : 90 degree hard pulse 1H
;p3 : 90 degree hard pulse 13C
;p4 : 13C pulse, 225deg for 500/600, 180deg for 750/900
;p5 : 90 degree hard pulse 15N
;pcpd2 : 90 deg cpd-pulse 13C (~85us)
;p12 : shaped 180 pulse for CO decoupling (80u)
;spnam12: shape for selective C=O pulse (gauss.128_5)
;p21 : 1m (Gradient in first INEPT)
;p22 : 800u (Gradient in first INEPT)
;p23 : 1m (Gradient for z-filter)
;p26 : 1m (Gradient for second INEPT)
;gpz1 : 19%
;gpz2 : 30%
```

```

;gpz3 : 65%
;gpz6 : 15%
;d1    : relaxation delay
;d2    : 1H-13C INEPT delay (1.7m)
;d6    : CCR mixing
;in0   : 1/2*SW(in Hz)

```

```
#include <Avance_dl.incl>
```

```

define delay INEPT_1
define delay INEPT_2
define delay RACT1
define delay RACT2
#define GRADIENT0 10u p20:gp0 200u
#define GRADIENT1 10u p21:gp1 200u
#define GRADIENT2 10u p22:gp2 200u
#define GRADIENT3 10u p23:gp3 200u
#define GRADIENT4 10u p24:gp4 200u
#define GRADIENT5 10u p25:gp5 200u
#define GRADIENT6 10u p26:gp6 200u

```

```
"p2=p1*2"
```

```
"p6=p5*2"
```

```
"p4=p3*2"
```

```
"in0=inf1/2"
```

```
"d0=in0/2-p3*2/3.14159"
```

```
"INEPT_1=d2-(p21+210u)"
```

```
"INEPT_2=d2-(p26+210u)"
```

```
"RACT1=d6-(p25+210u)-p11*0.45-10u"
```

```
"RACT2=d6-(p26+210u)-p11*0.45-10u"
```

```

1 10u ze
   10u
2 1m
   10u do:f2
   20u pl1:f1
   10u LOCKH_OFF

```

```

d1 p12:f2
20u p13:f3
20u LOCKH_ON
(p3 ph20):f2
GRADIEN0
10m
;-----First INEPT
(p1 ph20):f1
GRADIEN1
INEPT_1
(center (p2 ph20):f1 (p4 ph20):f2)
GRADIEN1
INEPT_1
(p1 ph21):f1
GRADIEN2
;-----13C evolution
(p1 ph20):f1
2u
(refalign(p3 ph1 d0 d0 p3 ph2):f2 center(p2 ph20):f1 center(p6 ph20):f3)
2u
(p1 ph22):f1
GRADIEN3
;-----First RACT step
(p1 ph20):f1
GRADIEN4
RACT1
10u
(center (p2 ph20):f1 (p4 ph20):f2)
GRADIEN4
RACT1 p11:f1
10u
;-----1Hy2Hz --> 1Hz2Hy and removing diagonal
(center (p1 ph3):f1 (p3 ph4):f2)
;-----Second RACT step
GRADIEN5
RACT2
10u
(center (p2 ph20):f1 (p4 ph20):f2)
GRADIEN5
RACT2 p11:f1

```



```

10u
;-----Second INEPT
  (p1 ph5):f1
  GRADIENT6
  INEPT_2
  (center (p2 ph20):f1 (p4 ph20):f2)
  GRADIENT6
  INEPT_2 p112:f2 LOCKH_OFF
;-----Acquisition
go=2 ph31 cpd2:f2
1m do:f2 mc #0 to 2 F1PH(ip1, id0)
10u do:f1
10u do:f2
10u do:f3
10u LOCKH_OFF
exit

ph1= 0 2
ph2= 0 0 2 2
ph3= 0 0 0 0 0 0 0 0
      0 0 0 0 0 0 0 0
      2 2 2 2 2 2 2 2
      2 2 2 2 2 2 2 2
ph4= 0 0 0 0 0 0 0 0
      2 2 2 2 2 2 2 2
ph5= 1 1 1 1 3 3 3 3
ph31=2 0 0 2
ph20=0
ph21=1
ph22=2
ph23=3

```

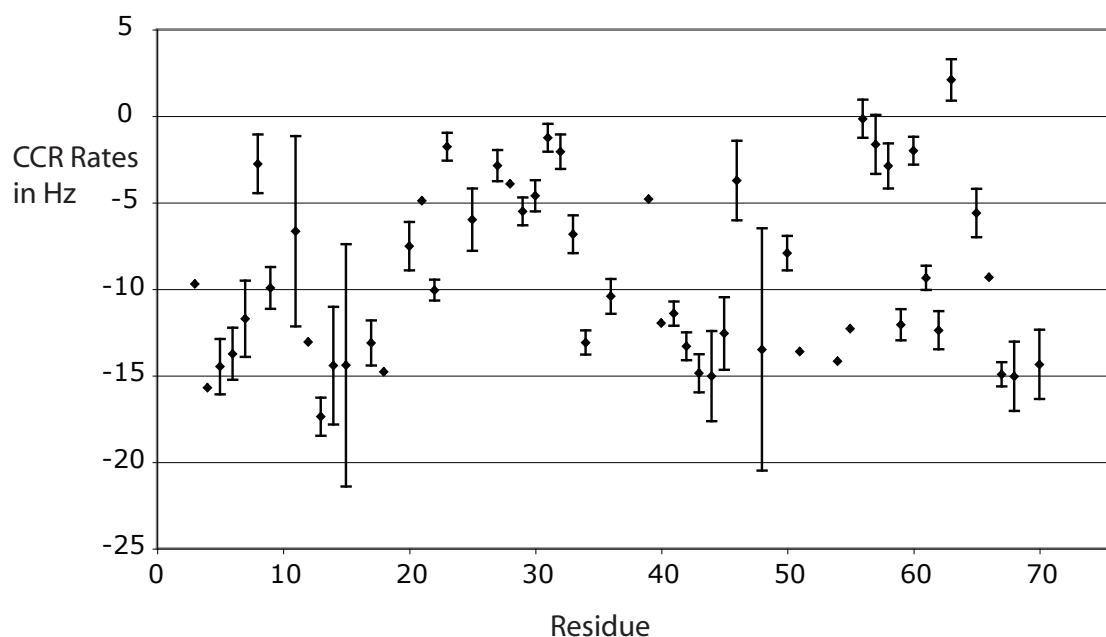


**Figure 6.1:** The graph shows the experimentally measured CCR rates and corresponding experimental errors of NH -  $C\alpha H\alpha$  pairs in the protein backbone of ubiquitin.

**Table 6.2:** For each NOE peak the two involved atoms are listed as well as their chemical shifts. The chemical shifts of the atoms are given in ppm.

Atom(1)	Atom(2)	cs(1)	cs(2)	Atom(1)	Atom(2)	cs(1)	cs(2)	Atom(1)	Atom(2)	cs(1)	cs(2)
R72 HG2	R72 HA	1.499	4.246	R72 HB3	R72 H	1.725	8.534	R72 HA	R72 HG2	4.246	1.499
R72 HA	L73 H	4.246	8.235	L71 HD2	L71 HA	0.818	4.986	L71 HD2	R72 H	0.818	8.534
L71 HB2	L71 HA	1.480	4.986	L71 HB2	L71 H	1.480	8.011	L71 HB3	L71 HD1	1.623	0.923
L71 HB3	L71 H	1.623	8.011	L71 HA	L71 HD2	4.986	0.818	L71 HA	L71 HB2	4.986	1.480
L71 HA	Q41 HA	4.986	4.169	L71 HA	L71 H	4.986	8.011	L71 HA	R42 H	4.986	8.457
L71 HA	R72 H	4.986	8.534	V70 HG2	H68 HB2	0.794	3.031	V70 HG2	V70 H	0.794	9.116
V70 HB	V70 HG1	1.983	0.891	V70 HB	V70 HA	1.983	4.312	V70 HB	L71 H	1.983	8.011
V70 HB	V70 H	1.983	9.116	V70 HA	V70 HG2	4.312	0.794	V70 HA	L71 H	4.312	8.011
V70 HA	V70 H	4.312	9.116	L69 HD2	L69 HG	0.808	1.288	L69 HD2	L69 HA	0.808	5.120
L69 HG	V70 H	1.288	9.116	L69 HB2	L69 HB3	1.567	1.052	L69 HB2	T7 HA	1.567	4.911
L69 HB2	L69 HA	1.567	5.120	L69 HB2	V70 H	1.567	9.116	L69 HB2	L69 H	1.567	8.271
L69 HB3	L69 HB2	1.052	1.567	L69 HB3	L69 HA	1.052	5.120	L69 HB3	L69 H	1.052	8.271
L69 HA	L69 HD1	5.120	0.921	L69 HA	L69 HD2	5.120	0.808	L69 HA	L69 HB3	5.120	1.052
L69 HA	L69 HG	5.120	1.288	L69 HA	L69 HB2	5.120	1.567	L69 HA	L43 HA	5.120	5.317
L69 HA	L69 H	5.120	8.271	L69 HA	V70 H	5.120	9.116	H68 HB2	V70 HG2	3.031	0.794
H68 HB2	L69 H	3.031	8.271	H68 HB2	I44 H	3.031	9.078	H68 HB2	H68 H	3.031	9.179
H68 HB3	I44 HB	2.850	1.692	H68 HB3	H68 HA	2.850	5.115	H68 HB3	L69 H	2.850	8.271
H68 HB3	I44 H	2.850	9.078	H68 HB3	H68 H	2.850	9.179	H68 HA	H68 HB3	5.115	2.850
H68 HA	H68 HB2	5.115	3.031	H68 HA	K6 H	5.115	8.914	L67 HD2	F45 HB3	0.614	2.965
L67 HD1	L67 HB2	0.648	1.583	L67 HD1	L67 HA	0.648	5.026	L67 HD1	L67 H	0.648	9.348
L67 HG	I3 HD1	1.722	0.544	L67 HG	S65 HB3	1.722	3.594	L67 HG	F4 HD1	1.722	7.022
L67 HG	F45 HD1	1.722	7.310	L67 HG	S65 H	1.722	7.615	L67 HG	L67 H	1.722	9.348
L67 HB2	L67 HD1	1.583	0.648	L67 HB2	L67 HA	1.583	5.026	L67 HB2	F45 HD1	1.583	7.310
L67 HB2	H68 H	1.583	9.179	L67 HB2	L67 H	1.583	9.348	L67 HA	L67 HD2	5.026	0.614

Table 6.2: – continued from last page

Atom(1)	Atom(2)	cs(1)	cs(2)	Atom(1)	Atom(2)	cs(1)	cs(2)	Atom(1)	Atom(2)	cs(1)	cs(2)
L67 HA	L67 HD1	5.026	0.648	L67 HA	L67 HB2	5.026	1.583	L67 HA	L67 HG	5.026	1.722
L67 HA	H68 H	5.026	9.179	L67 HA	L67 H	5.026	9.348	T66 HG2	F4 HB2	0.903	2.828
T66 HG2	F4 HB3	0.903	2.998	T66 HG2	T66 HB	0.903	4.025	T66 HG2	T66 HA	0.903	5.237
T66 HG2	F4 HD1	0.903	7.022	T66 HG2	K6 H	0.903	8.914	T66 HG2	L67 H	0.903	9.348
T66 HB	T66 HG2	4.025	0.903	T66 HB	T66 HA	4.025	5.237	T66 HA	T66 HG2	5.237	0.903
T66 HA	L67 HG	5.237	1.722	T66 HA	F4 HB2	5.237	2.828	T66 HA	F4 HB3	5.237	2.998
T66 HA	T66 HB	5.237	4.025	T66 HA	F4 HD1	5.237	7.022	T66 HA	F4 H	5.237	8.548
T66 HA	L67 H	5.237	9.348	S65 HB2	I61 HG2	3.860	0.434	S65 HB2	I61 HA	3.860	3.338
S65 HB2	S65 HB3	3.860	3.594	S65 HB2	T66 H	3.860	8.628	S65 HB2	F45 HD1	3.860	7.310
S65 HB2	Q62 H	3.860	7.560	S65 HB2	F45 HE1	3.860	7.485	S65 HB3	I61 HG2	3.594	0.434
S65 HB3	S65 HB2	3.594	3.860	S65 HB3	F45 HE1	3.594	7.485	S65 HB3	S65 H	3.594	7.615
S65 HB3	T66 H	3.594	8.628	E64 HA	E64 HG2	3.294	2.188	E64 HA	E64 HB3	3.294	2.366
E64 HA	E64 HB2	3.294	2.484	E64 HA	I3 HA	3.294	4.125	E64 HA	F4 HD1	3.294	7.022
E64 HA	F4 HE1	3.294	7.195	E64 HA	S65 H	3.294	7.615	E64 HA	F4 H	3.294	8.548
E64 HA	E64 H	3.294	9.231	K63 HE2	K63 HG2	2.994	1.450	K63 HE2	K63 HD2	2.994	1.695
K63 HE2	K63 H	2.994	8.382	K63 HD2	K63 HE2	1.695	2.994	K63 HG2	K63 HE2	1.450	2.994
K63 HG2	K63 HA	1.450	3.928	K63 HG2	K63 H	1.450	8.382	K63 HG2	Q2 H	1.450	8.855
K63 HB2	K63 HA	1.854	3.928	K63 HB2	K63 H	1.854	8.382	K63 HB3	K63 HA	1.997	3.928
K63 HB3	K63 H	1.997	8.382	K63 HB3	E64 H	1.997	9.231	K63 HA	K63 HG2	3.928	1.450
K63 HA	K63 HB2	3.928	1.854	K63 HA	K63 HB3	3.928	1.997	K63 HA	Q2 H	3.928	8.855
K63 HA	E64 H	3.928	9.231	Q62 HE22	Q62 HE21	6.745	7.224	Q62 HE21	Q62 HE22	7.224	6.745
Q62 HA	Q62 H	4.441	7.560	Q62 HA	K63 H	4.441	8.382	I61 HD1	I61 HG12	0.355	-0.364
I61 HD1	L50 HD2	0.355	-0.194	I61 HD1	F45 HB2	0.355	2.760	I61 HD1	F45 HB3	0.355	2.965
I61 HD1	I61 HA	0.355	3.338	I61 HD1	Y59 HB2	0.355	3.406	I61 HD1	L56 HA	0.355	3.999
I61 HD1	I61 H	0.355	7.196	I61 HD1	F45 HD1	0.355	7.310	I61 HG2	I61 HG12	0.434	-0.364
I61 HG2	I61 HB	0.434	1.349	I61 HG2	I61 HA	0.434	3.338	I61 HG2	S65 HB3	0.434	3.594
I61 HG2	S65 HB2	0.434	3.860	I61 HG2	Q62 H	0.434	7.560	I61 HG2	S65 H	0.434	7.615
I61 HG2	I61 HG12	0.434	-0.364	I61 HG2	I61 HB	0.434	1.349	I61 HG2	I61 HA	0.434	3.338
I61 HG2	S65 HB3	0.434	3.594	I61 HG2	S65 HB2	0.434	3.860	I61 HG2	S65 H	0.434	7.615
I61 HG2	Q62 H	0.434	7.560	I61 HB	I61 HD1	1.349	0.355	I61 HB	I61 HG2	1.349	0.434
I61 HB	I61 HG12	1.349	-0.364	I61 HB	L56 HA	1.349	3.999	I61 HB	I61 H	1.349	7.196
I61 HB	Q62 H	1.349	7.560	I61 HA	I61 HG12	3.338	-0.364	I61 HA	I61 HG2	3.338	0.434
I61 HA	I61 HB	3.338	1.349	I61 HA	Q62 H	3.338	7.560	N60 HD22	N60 HB2	6.747	2.767
N60 HD22	N60 HB3	6.747	3.245	N60 HD22	N60 HA	6.747	4.296	N60 HD22	N60 HD21	6.747	7.460
N60 HD21	N60 HB3	7.460	3.245	N60 HD21	N60 HD22	7.460	6.747	N60 HB2	N60 HD22	2.767	6.747
N60 HB2	N60 H	2.767	8.099	N60 HB3	N60 HA	3.245	4.296	N60 HB3	N60 HD22	3.245	6.747
N60 HB3	N60 HD21	3.245	7.460	N60 HB3	N60 H	3.245	8.099	N60 HA	N60 HB3	4.296	3.245
N60 HA	N60 HD22	4.296	6.747	N60 HA	I61 H	4.296	7.196	N60 HA	N60 H	4.296	8.099
Y59 HE1	L50 HD2	6.836	-0.194	Y59 HE1	L50 HD1	6.836	0.470	Y59 HE1	I23 HD1	6.836	0.533
Y59 HE1	L50 HB2	6.836	0.969	Y59 HE1	I23 HG12	6.836	1.245	Y59 HE1	R54 HG2	6.836	1.578
Y59 HE1	E51 HB3	6.836	1.927	Y59 HE1	R54 HB2	6.836	2.039	Y59 HE1	R54 HB3	6.836	2.181
Y59 HE1	D58 HB3	6.836	2.939	Y59 HE1	Y59 HB2	6.836	3.406	Y59 HE1	Y59 HB3	6.836	2.482
Y59 HE1	L50 HA	6.836	4.036	Y59 HE1	E51 H	6.836	8.314	Y59 HE1	T55 H	6.836	8.780
Y59 HB2	L50 HD2	3.406	-0.194	Y59 HB2	I61 HD1	3.406	0.355	Y59 HB2	Y59 HB3	3.406	2.482
Y59 HB2	Y59 HE1	3.406	6.836	Y59 HB2	I61 H	3.406	7.196	Y59 HB2	F45 HD1	3.406	7.310
Y59 HB3	I61 HD1	2.482	0.355	Y59 HB3	L50 HD2	2.482	-0.194	Y59 HB3	Y59 HB2	2.482	3.406
Y59 HB3	L56 HA	2.482	3.999	Y59 HB3	Y59 HE1	2.482	6.836	Y59 HB3	F45 HD1	2.482	7.310
D58 HB2	D58 HB3	2.241	2.939	D58 HB2	D58 HA	2.241	4.242	D58 HB2	D58 H	2.241	7.883
D58 HB3	D58 HB2	2.939	2.241	D58 HB3	D58 HA	2.939	4.242	D58 HB3	Y59 HE1	2.939	6.836
D58 HB3	D58 H	2.939	7.883	D58 HA	D58 HB2	4.242	2.241	D58 HA	D58 H	4.242	7.883
S57 HB2	D58 H	3.705	7.883	S57 HB2	S57 H	3.705	8.395	S57 HB3	S57 H	3.842	8.395
S57 HA	S57 HB2	4.205	3.705	S57 HA	S57 HB3	4.205	3.842	S57 HA	N60 H	4.205	8.099
S57 HA	S57 H	4.205	8.395	L56 HD2	L56 HB2	0.575	1.170	L56 HD2	L56 HB3	0.575	2.047

Table 6.2: – continued from last page

Atom(1)	Atom(2)	cs(1)	cs(2)	Atom(1)	Atom(2)	cs(1)	cs(2)	Atom(1)	Atom(2)	cs(1)	cs(2)
L56 HD2	L56 HA	0.575	3.999	L56 HD2	S57 H	0.575	8.395	L56 HD2	L56 H	0.575	8.106
L56 HB2	I61 HG12	1.170	-0.364	L56 HB2	L56 HD2	1.170	0.575	L56 HB2	L56 HB3	1.170	2.047
L56 HB2	L56 HA	1.170	3.999	L56 HB2	S57 H	1.170	8.395	L56 HB3	V17 HG2	2.047	0.390
L56 HB3	L56 HD2	2.047	0.575	L56 HB3	L56 HD1	2.047	0.702	L56 HB3	L56 HB2	2.047	1.170
L56 HB3	L56 HA	2.047	3.999	L56 HB3	L56 H	2.047	8.106	L56 HB3	S57 H	2.047	8.395
L56 HA	I61 HD1	3.999	0.355	L56 HA	L56 HD2	3.999	0.575	L56 HA	L56 HB2	3.999	1.170
L56 HA	I61 H	3.999	7.196	L56 HA	L56 H	3.999	8.106	T55 HG2	T55 HA	1.080	5.181
T55 HG2	T22 H	1.080	7.793	T55 HG2	D58 H	1.080	7.883	T55 HG2	L56 H	1.080	8.106
T55 HG2	T55 H	1.080	8.780	T55 HB	T55 HG2	4.483	1.080	T55 HB	T55 HA	4.483	5.181
T55 HB	T55 H	4.483	8.780	T55 HA	T55 HG2	5.181	1.080	T55 HA	T22 HG2	5.181	1.215
T55 HA	T55 HB	5.181	4.483	T55 HA	T22 HA	5.181	4.863	T55 HA	D58 H	5.181	7.883
T55 HA	L56 H	5.181	8.106	T55 HA	I23 H	5.181	8.475	T55 HA	T55 H	5.181	8.780
R54 HB2	Y59 HE1	2.039	6.836	R54 HB3	Y59 HE1	2.181	6.836	R54 HB3	R54 H	2.181	7.423
G53 HA2	G53 H	3.930	9.445	D52 HB2	D52 HA	2.575	4.325	D52 HB2	E24 H	2.575	9.567
D52 HA	D52 HB2	4.325	2.575	D52 HA	D52 HA	4.325	4.325	D52 HA	E24 H	4.325	9.567
E51 HG2	E51 H	2.382	8.314	E51 HB3	E51 H	1.927	8.314	E51 HA	E51 HB2	4.443	2.192
E51 HA	E51 H	4.443	8.314	L50 HD2	I61 HD1	-0.194	0.355	L50 HD2	L50 HD1	-0.194	0.470
L50 HD2	L50 HB2	-0.194	0.969	L50 HD2	L50 HG	-0.194	1.424	L50 HD2	Y59 HB3	-0.194	2.482
L50 HD2	F45 HB3	-0.194	2.965	L50 HD2	F45 HB2	-0.194	2.760	L50 HD2	Y59 HB2	-0.194	3.406
L50 HD2	L50 HA	-0.194	4.036	L50 HD2	I44 HA	-0.194	4.892	L50 HD2	Y59 HE1	-0.194	6.836
L50 HD2	Y59 H	-0.194	7.219	L50 HD2	F45 HD1	-0.194	7.310	L50 HD2	E51 H	-0.194	8.314
L50 HD2	L50 H	-0.194	8.499	L50 HD2	F45 H	-0.194	8.789	L50 HD2	I44 H	-0.194	9.078
L50 HB2	L50 HD2	0.969	-0.194	L50 HB2	L50 HD1	0.969	0.470	L50 HB2	L50 HB3	0.969	1.445
L50 HB2	Y59 HE1	0.969	6.836	L50 HB2	L50 H	0.969	8.499	L50 HA	L50 HD2	4.036	-0.194
L50 HA	L50 HB2	4.036	0.969	L50 HA	Y59 HE1	4.036	6.836	L50 HA	E51 H	4.036	8.314
Q49 HB2	Q49 HE22	1.940	6.781	Q49 HB2	Q49 H	1.940	8.545	G47 HA2	G47 H	3.402	8.020
A46 HB	A46 HA	0.826	3.657	A46 HB	F45 HD1	0.826	7.310	A46 HB	A46 H	0.826	8.874
A46 HA	A46 HB	3.657	0.826	A46 HA	G47 H	3.657	8.020	A46 HA	A46 H	3.657	8.874
F45 HD1	I61 HG12	7.310	-0.364	F45 HD1	L50 HD2	7.310	-0.194	F45 HD1	I61 HD1	7.310	0.355
F45 HD1	L50 HD1	7.310	0.470	F45 HD1	L67 HD2	7.310	0.614	F45 HD1	A46 HB	7.310	0.826
F45 HD1	L67 HG	7.310	1.722	F45 HD1	F45 HB2	7.310	2.760	F45 HD1	F45 HB3	7.310	2.965
F45 HD1	Y59 HB2	7.310	3.406	F45 HD1	L67 HA	7.310	5.026	F45 HD1	F45 HA	7.310	5.103
F45 HD1	F45 HE1	7.310	7.485	F45 HD1	T66 H	7.310	8.628	F45 HD1	A46 H	7.310	8.874
F45 HD1	F45 H	7.310	8.789	F45 HD1	H68 H	7.310	9.179	F45 HD1	L67 H	7.310	9.348
F45 HB2	L50 HD2	2.760	-0.194	F45 HB2	I61 HD1	2.760	0.355	F45 HB2	L50 HD1	2.760	0.470
F45 HB2	F45 HB3	2.760	2.965	F45 HB2	F45 HA	2.760	5.103	F45 HB2	F45 HD1	2.760	7.310
F45 HB2	F45 H	2.760	8.789	F45 HB3	L50 HD2	2.965	-0.194	F45 HB3	I61 HD1	2.965	0.355
F45 HB3	L50 HD1	2.965	0.470	F45 HB3	L67 HD2	2.965	0.614	F45 HB3	F45 HB2	2.965	2.760
F45 HB3	L67 HA	2.965	5.026	F45 HB3	F45 HD1	2.965	7.310	F45 HA	L50 HD1	5.103	0.470
F45 HA	F45 HB2	5.103	2.760	F45 HA	F45 HB3	5.103	2.965	F45 HA	F45 HD1	5.103	7.310
F45 HA	F45 H	5.103	8.789	I44 HG2	L50 HD2	0.645	-0.194	I44 HB	I44 HA	1.692	4.892
I44 HB	F45 H	1.692	8.789	I44 HB	I44 H	1.692	9.078	I44 HB	H68 H	1.692	9.179
I44 HA	L50 HD2	4.892	-0.194	I44 HA	L50 HD1	4.892	0.470	I44 HA	I44 HD1	4.892	0.633
I44 HA	I44 HG12	4.892	1.027	I44 HA	L43 HG	4.892	1.426	I44 HA	I44 HB	4.892	1.692
I44 HA	F45 H	4.892	8.789	I44 HA	I44 H	4.892	9.078	L43 HD1	L43 HA	0.752	5.317
L43 HD1	L43 H	0.752	8.728	L43 HG	L43 HA	1.426	5.317	L43 HB2	L50 HD1	1.118	0.470
L43 HB2	L43 HB3	1.118	1.510	L43 HB2	L43 HA	1.118	5.317	L43 HB2	L43 H	1.118	8.728
L43 HB2	I44 H	1.118	9.078	L43 HB3	L43 HB2	1.510	1.118	L43 HB3	L43 HA	1.510	5.317
L43 HB3	L43 H	1.510	8.728	L43 HA	I44 HD1	5.317	0.633	L43 HA	L43 HD2	5.317	0.811
L43 HA	L43 HD1	5.317	0.752	L43 HA	L43 HB2	5.317	1.118	L43 HA	L43 HG	5.317	1.426
L43 HA	L43 HB3	5.317	1.510	L43 HA	L69 HA	5.317	5.120	L43 HA	L43 H	5.317	8.728
L43 HA	I44 H	5.317	9.078	L43 HA	H68 H	5.317	9.179	R42 HA	L43 H	4.439	8.728
R42 HA	L43 H	4.439	8.728	Q41 HE22	I30 HG2	6.454	0.651	Q41 HE22	Q41 HG2	6.454	1.609

Table 6.2: – continued from last page

Atom(1)	Atom(2)	cs(1)	cs(2)	Atom(1)	Atom(2)	cs(1)	cs(2)	Atom(1)	Atom(2)	cs(1)	cs(2)
Q41 HE22	Q41 HB2	6.454	1.922	Q41 HE22	I30 HB	6.454	2.303	Q41 HE22	Q31 HA	6.454	3.780
Q41 HE22	P38 HA	6.454	4.071	Q41 HE22	Q41 HE22	6.454	6.454	Q41 HE22	Q31 H	6.454	8.497
Q41 HE22	I30 H	6.454	8.223	Q41 HE21	Q41 HG2	6.140	1.609	Q41 HE21	Q41 HB2	6.140	1.922
Q41 HE21	I30 HB	6.140	2.303	Q41 HE21	Q31 H	6.140	8.497	Q41 HE21	Q41 HE22	6.140	6.454
Q41 HB2	Q41 HE21	1.922	6.140	Q41 HB2	Q41 HE22	1.922	6.454	Q41 HB2	Q40 H	1.922	7.755
Q41 HA	L71 HA	4.169	4.986	Q41 HA	Q41 H	4.169	7.406	Q41 HA	V70 H	4.169	9.116
Q41 HA	R42 H	4.169	8.457	Q40 HE22	P37 HG2	6.657	2.052	Q40 HE22	Q40 HE21	6.657	7.561
Q40 HE21	Q40 HE22	7.561	6.657	Q40 HB3	P37 HD2	1.786	3.519	Q40 HB3	Q40 H	1.786	7.755
Q40 HA	Q40 HB3	4.417	1.786	Q40 HA	Q41 H	4.417	7.406	Q40 HA	Q40 H	4.417	7.755
D39 HB2	D39 HA	2.626	4.369	D39 HB2	D39 H	2.626	8.468	D39 HB3	D39 HA	2.716	4.369
D39 HB3	D39 H	2.716	8.468	D39 HA	D39 HB2	4.369	2.626	D39 HA	D39 H	4.369	8.468
P38 HD2	Q31 HE22	3.706	6.731	P38 HD2	Q31 HE21	3.706	7.555	P38 HD2	D39 H	3.706	8.468
P38 HD2	P38 HG2	3.706	1.609	P38 HG2	P38 HD2	1.609	3.706	P38 HB3	P38 HA	1.997	4.071
P38 HA	P38 HB2	4.071	2.183	P38 HA	Q41 HE22	4.071	6.454	P38 HA	Q40 H	4.071	7.755
P37 HD2	I36 HG2	3.519	0.886	P37 HD2	P37 HG2	3.519	2.052	P37 HD2	Q40 HB2	3.519	2.367
P37 HD2	I36 HA	3.519	4.373	P37 HG2	Q40 HE22	2.052	6.657	P37 HG2	P37 HD2	2.052	3.519
P37 HB2	P38 HD2	1.926	3.706	I36 HD1	I36 H	0.744	6.126	I36 HG12	I36 HA	1.047	4.373
I36 HG12	I36 H	1.047	6.126	I36 HG2	I36 HB	0.886	1.383	I36 HG2	Q40 HB2	0.886	2.367
I36 HG2	P37 HD2	0.886	3.519	I36 HG2	I36 HA	0.886	4.373	I36 HG2	I36 H	0.886	6.126
I36 HG2	Q40 H	0.886	7.755	I36 HB	I36 HG12	1.383	1.047	I36 HB	I36 HA	1.383	4.373
I36 HB	I36 H	1.383	6.126	I36 HA	I36 HG2	4.373	0.886	I36 HA	I36 HG12	4.373	1.047
I36 HA	P37 HD2	4.373	3.519	I36 HA	I36 H	4.373	6.126	G35 HA2	I36 H	4.101	6.126
G35 HA2	G35 H	4.101	8.427	E34 HB2	E34 HB3	1.635	2.208	E34 HB3	E34 HB2	2.208	1.635
E34 HA	E34 HB2	4.534	1.635	E34 HA	E34 H	4.534	8.665	K33 HE2	K33 HD2	3.076	1.657
K33 HG2	K33 H	1.561	7.430	K33 HB2	I30 HA	1.961	3.453	K33 HB2	K33 H	1.961	7.430
K33 HB3	I30 HA	1.796	3.453	K33 HB3	K33 H	1.796	7.430	K33 HA	K33 HG2	4.261	1.561
K33 HA	K33 HB3	4.261	1.796	K33 HA	E34 H	4.261	8.665	K33 HA	K33 H	4.261	7.430
K33 HA	E34 H	4.261	8.665	D32 HB2	D32 HA	2.703	4.291	D32 HB2	K33 H	2.703	7.430
D32 HB3	K29 HA	2.799	4.154	D32 HB3	K33 H	2.799	7.430	D32 HB3	D32 H	2.799	7.962
D32 HA	D32 HB2	4.291	2.703	D32 HA	D32 HB3	4.291	2.799	D32 HA	D32 H	4.291	7.962
Q31 HE22	Q31 HG2	6.731	2.226	Q31 HE22	Q31 HB2	6.731	2.435	Q31 HE22	Q31 HB3	6.731	1.907
Q31 HE22	P38 HD2	6.731	3.706	Q31 HE21	P38 HD2	7.555	3.706	Q31 HE21	Q31 HA	7.555	3.780
Q31 HE21	Q31 HE22	7.555	6.731	Q31 HG2	Q31 HA	2.226	3.780	Q31 HG2	Q31 HE22	2.226	6.731
Q31 HB2	D32 H	2.435	7.962	Q31 HB3	Q31 HE22	1.907	6.731	Q31 HB3	Q31 HB2	1.907	2.435
Q31 HB3	Q31 HA	1.907	3.780	Q31 HA	Q31 HB3	3.780	1.907	Q31 HA	Q31 HG2	3.780	2.226
Q31 HA	Q31 HB2	3.780	2.435	Q31 HA	I36 H	3.780	6.126	Q31 HA	Q41 HE22	3.780	6.454
Q31 HA	D32 H	3.780	7.962	Q31 HA	E34 H	3.780	8.665	Q31 HA	Q31 H	3.780	8.497
I30 HD1	I30 HB	0.835	2.303	I30 HB	I30 HD1	2.303	0.835	I30 HB	I30 HA	2.303	3.453
I30 HB	Q41 HE21	2.303	6.140	I30 HB	Q41 HE22	2.303	6.454	I30 HB	I30 H	2.303	8.223
I30 HA	I30 HG2	3.453	0.651	I30 HA	I30 HD1	3.453	0.835	I30 HA	K33 HB3	3.453	1.796
I30 HA	K33 HB2	3.453	1.961	I30 HA	I30 HB	3.453	2.303	I30 HA	K33 H	3.453	7.430
I30 HA	I30 H	3.453	8.223	I30 HA	Q31 H	3.453	8.497	I30 HA	E34 H	3.453	8.665
K29 HE2	K29 HB2	2.943	1.744	K29 HD2	K29 HB3	1.422	2.089	K29 HD2	K29 HE2	1.422	2.943
K29 HD2	V26 HA	1.422	3.346	K29 HD2	K29 H	1.422	7.824	K29 HG2	K29 H	1.558	7.824
K29 HB3	V26 HG2	2.089	0.931	K29 HB3	V26 HA	2.089	3.346	K29 HB3	K29 H	2.089	7.824
K29 HB3	I30 H	2.089	8.223	K29 HA	D32 HB2	4.154	2.703	K29 HA	D32 HB3	4.154	2.799
K29 HA	K29 H	4.154	7.824	A28 HB	A28 HA	1.582	4.107	A28 HB	N25 HA	1.582	4.497
A28 HB	A28 H	1.582	7.940	A28 HA	A28 HB	4.107	1.582	A28 HA	A28 H	4.107	7.940
K27 HE2	I23 HG2	2.598	0.738	K27 HE2	K27 HD2	2.598	1.640	K27 HE2	K27 HG2	2.598	1.388
K27 HE2	K27 HB2	2.598	1.521	K27 HE2	Q41 H	2.598	7.406	K27 HE2	L43 H	2.598	8.728
K27 HB3	K27 HG2	1.966	1.388	K27 HA	A28 H	4.529	7.940	V26 HG2	L56 HD2	0.931	0.575
V26 HG2	V26 HG1	0.931	0.674	V26 HG2	V26 HB	0.931	2.301	V26 HG2	D21 HB3	0.931	2.900
V26 HG2	V26 HA	0.931	3.346	V26 HG2	I23 HA	0.931	3.590	V26 HG2	N25 H	0.931	7.866

Table 6.2: – continued from last page

Atom(1)	Atom(2)	cs(1)	cs(2)	Atom(1)	Atom(2)	cs(1)	cs(2)	Atom(1)	Atom(2)	cs(1)	cs(2)
V26 HG2	V26 H	0.931	8.049	V26 HG1	V26 HG2	0.674	0.931	V26 HG1	V26 HA	0.674	3.346
V26 HB	V26 HG2	2.301	0.931	V26 HB	V26 HA	2.301	3.346	V26 HB	I23 HA	2.301	3.590
V26 HB	A28 H	2.301	7.940	V26 HB	K27 H	2.301	8.494	V26 HA	V26 HG1	3.346	0.674
V26 HA	V26 HG2	3.346	0.931	V26 HA	K29 HD2	3.346	1.422	V26 HA	K29 HB2	3.346	1.744
V26 HA	K29 HB3	3.346	2.089	V26 HA	V26 HB	3.346	2.301	V26 HA	K29 H	3.346	7.824
V26 HA	V26 H	3.346	8.049	V26 HA	I30 H	3.346	8.223	N25 HD22	N25 HB2	6.820	2.807
N25 HD22	N25 HD21	6.820	7.796	N25 HD21	N25 HD22	7.796	6.820	N25 HB2	N25 HB3	2.807	3.168
N25 HB2	N25 HD22	2.807	6.820	N25 HB2	N25 H	2.807	7.866	N25 HB2	N25 HD21	2.807	7.796
N25 HB2	V26 H	2.807	8.049	N25 HB3	D21 HB2	3.168	2.462	N25 HB3	N25 H	3.168	7.866
N25 HB3	N25 HD21	3.168	7.796	N25 HB3	V26 H	3.168	8.049	N25 HA	N25 HB3	4.497	3.168
N25 HA	N25 HB2	4.497	2.807	N25 HA	N25 H	4.497	7.866	E24 HG2	E24 H	2.380	9.567
E24 HB2	E24 HA	2.168	3.956	E24 HB2	E24 H	2.168	9.567	E24 HA	E24 H	3.956	9.567
I23 HD1	I23 HG12	0.533	1.245	I23 HD1	I23 HB	0.533	2.443	I23 HD1	I23 HA	0.533	3.590
I23 HD1	Y59 HE1	0.533	6.836	I23 HD1	I23 H	0.533	8.475	I23 HG12	I23 HD1	1.245	0.533
I23 HG12	I23 HB	1.245	2.443	I23 HG12	I23 HA	1.245	3.590	I23 HG12	I23 H	1.245	8.475
I23 HG12	Y59 HE1	1.245	6.836	I23 HG2	I23 HB	0.738	2.443	I23 HG2	K27 HE2	0.738	2.598
I23 HG2	I23 HA	0.738	3.590	I23 HB	I23 HD1	2.443	0.533	I23 HB	I23 HG2	2.443	0.738
I23 HB	I23 HG12	2.443	1.245	I23 HA	I23 HD1	3.590	0.533	I23 HA	I23 HG2	3.590	0.738
I23 HA	V26 HG2	3.590	0.931	I23 HA	I23 HG12	3.590	1.245	I23 HA	V26 HB	3.590	2.301
I23 HA	I23 HB	3.590	2.443	I23 HA	V26 H	3.590	8.049	I23 HA	I23 H	3.590	8.475
T22 HG2	T22 HB	1.215	4.752	T22 HG2	T22 HA	1.215	4.863	T22 HG2	T55 HA	1.215	5.181
T22 HG2	T22 H	1.215	7.793	T22 HB	T22 HG2	4.752	1.215	T22 HB	T22 H	4.752	7.793
T22 HB	I23 H	4.752	8.475	T22 HA	T22 HG2	4.863	1.215	T22 HA	T55 HA	4.863	5.181
T22 HA	T22 H	4.863	7.793	T22 HA	I23 H	4.863	8.475	D21 HB2	D21 HB3	2.462	2.900
D21 HB2	D21 H	2.462	7.996	D21 HB3	D21 HB2	2.900	2.462	D21 HB3	E18 H	2.900	8.661
D21 HB3	D21 H	2.900	7.996	S20 HA	S20 H	4.320	6.987	P19 HD2	E18 HA	3.752	5.011
P19 HB3	S20 H	1.958	6.987	P19 HB2	P19 HA	2.379	4.082	P19 HA	P19 HB2	4.082	2.379
E18 HG2	E18 HB3	2.290	1.563	E18 HG2	E18 HA	2.290	5.011	E18 HG2	E18 H	2.290	8.661
E18 HB2	S20 H	2.098	6.987	E18 HB3	E18 HG2	1.563	2.290	E18 HB3	E18 HB2	1.563	2.098
E18 HB3	S20 H	1.563	6.987	E18 HA	V17 HG2	5.011	0.390	E18 HA	E18 HB2	5.011	2.098
E18 HA	E18 HG2	5.011	2.290	E18 HA	P19 HD2	5.011	3.752	E18 HA	S20 H	5.011	6.987
E18 HA	E18 H	5.011	8.661	V17 HG2	L56 HB3	0.390	2.047	V17 HG2	V17 HB	0.390	2.283
V17 HG2	E18 HA	0.390	5.011	V17 HG2	Q2 HA	0.390	5.225	V17 HG2	I3 H	0.390	8.286
V17 HG2	E18 H	0.390	8.661	V17 HG2	V17 H	0.390	8.868	V17 HB	V17 HG2	2.283	0.390
V17 HB	V17 H	2.283	8.868	E16 HG2	E16 H	2.177	8.070	E16 HB2	E16 H	1.876	8.070
E16 HB3	E16 H	1.793	8.070	E16 HB3	E16 H	1.793	8.070	E16 HA	E16 H	4.842	8.070
L15 HB3	E16 H	1.304	8.070	L15 HA	L15 H	4.712	8.670	L15 HA	L15 HD1	4.712	0.710
T14 HG2	T14 HB	1.083	3.993	T14 HG2	Q2 HE21	1.083	7.564	T14 HG2	Q2 HE22	1.083	6.659
T14 HB	T14 HG2	3.993	1.083	T14 HB	T14 HA	3.993	4.914	T14 HA	T14 HB	4.914	3.993
T14 HA	F4 HA	4.914	5.566	T14 HA	F4 HD1	4.914	7.022	T14 HA	V5 H	4.914	9.248
I13 HD1	I13 HG12	0.676	1.060	I13 HD1	I13 H	0.676	9.490	I13 HG12	V5 H	1.060	9.248
I13 HG12	I13 H	1.060	9.490	I13 HG2	I13 H	0.829	9.490	I13 HB	I13 HG2	1.836	0.829
I13 HB	I13 HA	1.836	4.466	I13 HB	I13 H	1.836	9.490	I13 HA	I13 HG2	4.466	0.829
I13 HA	I13 HB	4.466	1.836	I13 HA	T14 H	4.466	8.634	I13 HA	I13 H	4.466	9.490
T12 HG2	T12 H	1.031	8.535	T12 HB	T12 HG2	3.903	1.031	T12 HB	T12 H	3.903	8.535
T12 HA	T12 HG2	5.009	1.031	T12 HA	I13 HB	5.009	1.836	T12 HA	T12 HB	5.009	3.903
T12 HA	L69 H	5.009	8.271	T12 HA	I13 H	5.009	9.490	K11 HG2	T12 H	1.195	8.535
K11 HB2	K11 HA	1.598	4.310	K11 HB2	K11 H	1.598	7.225	K11 HB3	K11 H	1.749	7.225
K11 HA	K11 H	4.310	7.225	K11 HA	T12 H	4.310	8.535	G10 HA2	G10 H	3.547	7.776
T9 HG2	T9 HA	1.221	4.366	T9 HG2	T9 H	1.221	7.589	T9 HA	T9 HG2	4.366	1.221
L8 HB3	L8 H	1.887	8.991	L8 HA	L8 HD2	4.261	0.931	L8 HA	L8 HB2	4.261	1.731
L8 HA	L8 HB3	4.261	1.887	L8 HA	L8 H	4.261	8.991	T7 HG2	T7 H	1.134	8.672
T7 HG2	L8 H	1.134	8.991	T7 HB	T7 HG2	4.754	1.134	T7 HA	T7 HG2	4.911	1.134

Table 6.2: – continued from last page

Atom(1)	Atom(2)	cs(1)	cs(2)	Atom(1)	Atom(2)	cs(1)	cs(2)	Atom(1)	Atom(2)	cs(1)	cs(2)
T7 HA	L69 H	4.911	8.271	T7 HA	L8 H	4.911	8.991	K6 HG2	K6 HA	1.233	5.244
K6 HG2	K6 H	1.233	8.914	K6 HB2	K6 HA	1.347	5.244	K6 HB2	K6 H	1.347	8.914
K6 HB3	K6 HA	1.647	5.244	K6 HB3	K6 H	1.647	8.914	K6 HA	K6 HG2	5.244	1.233
K6 HA	K6 HB2	5.244	1.347	K6 HA	K6 HB3	5.244	1.647	K6 HA	T7 H	5.244	8.672
K6 HA	K6 H	5.244	8.914	K6 HA	I13 H	5.244	9.490	V5 HG2	F4 HA	0.683	5.566
V5 HG2	V5 H	0.683	9.248	V5 HG1	L69 H	0.643	8.271	V5 HG1	K6 H	0.643	8.914
V5 HB	V5 HA	1.857	4.762	V5 HB	F4 HA	1.857	5.566	V5 HB	K6 H	1.857	8.914
V5 HB	V5 H	1.857	9.248	V5 HA	V5 HG1	4.762	0.643	V5 HA	V5 HG2	4.762	0.683
V5 HA	K6 H	4.762	8.914	V5 HA	L67 H	4.762	9.348	V5 HA	V5 H	4.762	9.248
V5 HA	L67 H	4.762	9.348	F4 HE1	E64 HG2	7.195	2.188	F4 HE1	E64 HB2	7.195	2.484
F4 HE1	E64 HB3	7.195	2.366	F4 HE1	F4 HB3	7.195	2.998	F4 HE1	E64 HA	7.195	3.294
F4 HE1	F4 HA	7.195	5.566	F4 HE1	E64 H	7.195	9.231	F4 HD1	T12 HG2	7.022	1.031
F4 HD1	T14 HG2	7.022	1.083	F4 HD1	L67 HG	7.022	1.722	F4 HD1	F4 HB2	7.022	2.828
F4 HD1	F4 HB3	7.022	2.998	F4 HD1	E64 HA	7.022	3.294	F4 HD1	T14 HA	7.022	4.914
F4 HD1	T66 HA	7.022	5.237	F4 HD1	F4 HA	7.022	5.566	F4 HD1	L15 H	7.022	8.670
F4 HD1	L67 H	7.022	9.348	F4 HD1	V5 H	7.022	9.248	F4 HD1	F4 H	7.022	8.548
F4 HB2	T12 HG2	2.828	1.031	F4 HB2	T66 HA	2.828	5.237	F4 HB2	F4 HA	2.828	5.566
F4 HB2	F4 HD1	2.828	7.022	F4 HB2	F4 H	2.828	8.548	F4 HB2	K6 H	2.828	8.914
F4 HB2	I13 H	2.828	9.490	F4 HB2	L67 H	2.828	9.348	F4 HB2	V5 H	2.828	9.248
F4 HB3	T12 HG2	2.998	1.031	F4 HB3	T66 HA	2.998	5.237	F4 HB3	F4 HA	2.998	5.566
F4 HB3	F4 HD1	2.998	7.022	F4 HB3	F4 H	2.998	8.548	F4 HB3	V5 H	2.998	9.248
F4 HB3	L67 H	2.998	9.348	F4 HA	V5 HG2	5.566	0.683	F4 HA	T12 HG2	5.566	1.031
F4 HA	T14 HG2	5.566	1.083	F4 HA	F4 HB3	5.566	2.998	F4 HA	F4 HB2	5.566	2.828
F4 HA	T14 HA	5.566	4.914	F4 HA	F4 HD1	5.566	7.022	F4 HA	F4 H	5.566	8.548
F4 HA	L15 H	5.566	8.670	F4 HA	V5 H	5.566	9.248	I3 HD1	I3 HB	0.544	1.854
I3 HD1	V26 HA	0.544	3.346	I3 HG2	I3 HA	0.582	4.125	I3 HG2	S65 H	0.582	7.615
I3 HG2	E64 H	0.582	9.231	I3 HG2	F4 H	0.582	8.548	I3 HB	I3 HG12	1.854	0.811
I3 HA	I3 HG2	4.125	0.582	I3 HA	E64 HA	4.125	3.294	I3 HA	S65 H	4.125	7.615
I3 HA	I3 H	4.125	8.286	I3 HA	F4 H	4.125	8.548	I3 HA	E64 H	4.125	9.231
Q2 HE22	T14 HG2	6.659	1.083	Q2 HE22	Q2 HE21	6.659	7.564	Q2 HE21	Q2 HB3	7.564	1.592
Q2 HE21	Q2 HE22	7.564	6.659	Q2 HG2	Q2 HA	1.806	5.225	Q2 HG2	Q2 HE22	1.806	6.659
Q2 HG2	Q2 HE21	1.806	7.564	Q2 HB2	Q2 HA	1.846	5.225	Q2 HB2	Q2 H	1.846	8.855
Q2 HB3	Q2 HA	1.592	5.225	Q2 HB3	Q2 HE22	1.592	6.659	Q2 HB3	Q2 HE21	1.592	7.564
Q2 HB3	Q2 H	1.592	8.855	Q2 HA	V17 HG2	5.225	0.390	Q2 HA	Q2 HB3	5.225	1.592
Q2 HA	Q2 HG2	5.225	1.806	Q2 HA	I3 H	5.225	8.286	Q2 HA	Q2 H	5.225	8.855
E64 H	S65 H	9.231	7.615	K63 H	K63 HG2	8.382	1.450	K63 H	K63 HB2	8.382	1.854
K63 H	E64 HG2	8.382	2.188	K63 H	Q62 HA	8.382	4.441	K63 H	K63 HA	8.382	3.928
I61 H	I61 HG2	7.196	0.434	I61 H	I61 HB	7.196	1.349	I61 H	I61 HA	7.196	3.338
Q62 H	Q62 HA	7.560	4.441	I61 H	I61 HG12	7.196	-0.364	I61 H	I61 HD1	7.196	0.355
I61 H	I61 HG2	7.196	0.434	I61 H	I61 HB	7.196	1.349	I61 H	Y59 HB2	7.196	3.406
I61 H	L56 HA	7.196	3.999	I61 H	S57 HA	7.196	4.205	I61 H	N60 H	7.196	8.099
N60 H	N60 HB2	8.099	2.767	N60 H	N60 HB3	8.099	3.245	N60 H	S57 HA	8.099	4.205
N60 H	N60 HA	8.099	4.296	N60 H	I61 H	8.099	7.196	D58 H	T55 HG2	7.883	1.080
D58 H	D58 HB2	7.883	2.241	D58 H	D58 HB3	7.883	2.939	D58 H	D58 HA	7.883	4.242
D58 H	T55 HA	7.883	5.181	D58 H	Y59 H	7.883	7.219	D58 H	S57 H	7.883	8.395
S57 H	L56 HD2	8.395	0.575	S57 H	L56 HB2	8.395	1.170	S57 H	L56 HB3	8.395	2.047
S57 H	S57 HB2	8.395	3.705	S57 H	S57 HB3	8.395	3.842	S57 H	S57 HA	8.395	4.205
S57 H	D58 H	8.395	7.883	S57 H	L56 H	8.395	8.106	L56 H	L56 HD2	8.106	0.575
L56 H	L56 HG	8.106	1.677	L56 H	L56 HB3	8.106	2.047	L56 H	T55 HB	8.106	4.483
L56 H	L56 HA	8.106	3.999	L56 H	T55 HA	8.106	5.181	L56 H	T55 H	8.106	8.780
T55 H	R54 HB2	8.780	2.039	T55 H	T55 HG2	8.780	1.080	T55 H	T55 HA	8.780	5.181
T55 H	Y59 HE1	8.780	6.836	T55 H	L56 H	8.780	8.106	T55 H	R54 H	8.780	7.423
R54 H	R54 HB2	7.423	2.039	R54 H	R54 HB3	7.423	2.181	R54 H	G53 H	7.423	9.445

Table 6.2: – continued from last page

Atom(1)	Atom(2)	cs(1)	cs(2)	Atom(1)	Atom(2)	cs(1)	cs(2)	Atom(1)	Atom(2)	cs(1)	cs(2)
G53 H	G53 HA2	9.445	3.930	G53 H	R54 H	9.445	7.423	D52 H	D52 HA	8.081	4.325
E51 H	L50 HD2	8.314	-0.194	E51 H	E51 HB3	8.314	1.927	E51 H	E51 HG2	8.314	2.382
E51 H	L50 HA	8.314	4.036	L50 H	L50 HD2	8.499	-0.194	L50 H	L50 HD1	8.499	0.470
L50 H	L50 HB2	8.499	0.969	L50 H	L50 HA	8.499	4.036	L50 H	Q49 HA	8.499	4.493
K48 H	I44 HG2	7.940	0.645	K48 H	K48 HG2	7.940	1.471	K48 H	K48 HB2	7.940	1.965
K48 H	F45 H	7.940	8.789	G47 H	G47 HA2	8.020	3.402	A46 H	A46 HA	8.874	3.657
F45 H	L50 HD2	8.789	-0.194	F45 H	L50 HD1	8.789	0.470	F45 H	I44 HD1	8.789	0.633
F45 H	F45 HB2	8.789	2.760	F45 H	I44 HA	8.789	4.892	F45 H	F45 HA	8.789	5.103
F45 H	G47 H	8.789	8.020	F45 H	F45 HD1	8.789	7.310	F45 H	K48 H	8.789	7.940
I44 H	L50 HD2	9.078	-0.194	I44 H	L50 HD1	9.078	0.470	I44 H	I44 HG12	9.078	1.027
I44 H	L43 HB2	9.078	1.118	I44 H	L43 HG	9.078	1.426	I44 H	L43 HB3	9.078	1.510
I44 H	I44 HB	9.078	1.692	I44 H	Q49 HG2	9.078	2.207	I44 H	H68 HB2	9.078	3.031
I44 H	H68 HB3	9.078	2.850	I44 H	I44 HA	9.078	4.892	I44 H	L43 HA	9.078	5.317
L43 H	L43 HG	8.728	1.426	L43 H	L43 HB3	8.728	1.510	L43 H	K27 HE2	8.728	2.598
L43 H	R42 HA	8.728	4.439	L43 H	L43 HA	8.728	5.317	R42 H	L43 HD2	8.457	0.811
R42 H	Q41 HA	8.457	4.169	Q41 H	P38 HA	7.406	4.071	Q41 H	Q40 HA	7.406	4.417
Q41 H	Q41 HA	7.406	4.169	Q41 H	Q41 HE21	7.406	6.140	Q41 H	Q40 H	7.406	7.755
Q40 H	I36 HG2	7.755	0.886	Q40 H	Q40 HB3	7.755	1.786	Q40 H	Q41 HB2	7.755	1.922
Q40 H	Q40 HB2	7.755	2.367	Q40 H	P38 HA	7.755	4.071	Q40 H	D39 HA	7.755	4.369
Q40 H	Q40 HA	7.755	4.417	Q40 H	Q40 HE21	7.755	7.561	Q40 H	Q41 H	7.755	7.406
Q40 H	D39 H	7.755	8.468	D39 H	D39 HB2	8.468	2.626	D39 H	D39 HB3	8.468	2.716
D39 H	D39 HA	8.468	4.369	D39 H	Q40 H	8.468	7.755	I36 H	I36 HD1	6.126	0.744
I36 H	I36 HG2	6.126	0.886	I36 H	I36 HG12	6.126	1.047	I36 H	I36 HB	6.126	1.383
I36 H	Q31 HA	6.126	3.780	I36 H	I36 HA	6.126	4.373	I36 H	E34 H	6.126	8.665
I36 H	G35 H	6.126	8.427	G35 H	G35 HA2	8.427	4.101	G35 H	I36 H	8.427	6.126
E34 H	I30 HG12	8.665	0.652	E34 H	E34 HB2	8.665	1.635	E34 H	E34 HG2	8.665	2.020
E34 H	E34 HB3	8.665	2.208	E34 H	Q31 HA	8.665	3.780	E34 H	I30 HA	8.665	3.453
E34 H	K33 HA	8.665	4.261	E34 H	E34 HA	8.665	4.534	E34 H	K33 H	8.665	7.430
K33 H	K33 HB3	7.430	1.796	K33 H	D32 HB2	7.430	2.703	K33 H	D32 HB3	7.430	2.799
K33 H	I30 HA	7.430	3.453	K33 H	E34 H	7.430	8.665	K33 H	D32 H	7.430	7.962
D32 H	Q31 HB2	7.962	2.435	D32 H	D32 HB2	7.962	2.703	D32 H	D32 HB3	7.962	2.799
D32 H	Q31 HA	7.962	3.780	D32 H	D32 HA	7.962	4.291	D32 H	K33 H	7.962	7.430
Q31 H	I30 HG12	8.497	0.652	Q31 H	Q41 HE22	8.497	6.454	Q31 H	A28 H	8.497	7.940
Q31 H	I30 H	8.497	8.223	I30 H	I30 HG12	8.223	0.652	I30 H	I30 HG2	8.223	0.651
I30 H	I30 HD1	8.223	0.835	I30 H	K29 HB3	8.223	2.089	I30 H	I30 HB	8.223	2.303
I30 H	V26 HA	8.223	3.346	I30 H	Q41 HE22	8.223	6.454	I30 H	Q31 H	8.223	8.497
I30 H	K29 H	8.223	7.824	K29 H	K29 HD2	7.824	1.422	K29 H	K29 HG2	7.824	1.558
K29 H	K29 HB2	7.824	1.744	K29 H	K29 HB3	7.824	2.089	K29 H	V26 HA	7.824	3.346
K29 H	K29 HA	7.824	4.154	K29 H	I30 H	7.824	8.223	A28 H	A28 HB	7.940	1.582
A28 H	A28 HA	7.940	4.107	K27 H	V26 HB	8.494	2.301	K27 H	K27 HA	8.494	4.529
V26 H	V26 HG2	8.049	0.931	V26 H	V26 HB	8.049	2.301	V26 H	I23 HA	8.049	3.590
V26 H	N25 HB3	8.049	3.168	V26 H	V26 HA	8.049	3.346	N25 H	V26 HB	7.866	2.301
N25 H	N25 HB3	7.866	3.168	E24 H	E24 HB2	9.567	2.168	E24 H	E24 HG2	9.567	2.380
E24 H	D52 HA	9.567	4.325	E24 H	E24 HA	9.567	3.956	E24 H	I23 H	9.567	8.475
I23 H	I23 HG2	8.475	0.738	I23 H	I23 HG12	8.475	1.245	I23 H	I23 HA	8.475	3.590
I23 H	T22 HB	8.475	4.752	I23 H	T55 HA	8.475	5.181	I23 H	T22 HA	8.475	4.863
T22 H	T22 HG2	7.793	1.215	T22 H	T22 HA	7.793	4.863	D21 H	D21 HB3	7.996	2.900
D21 H	S20 H	7.996	6.987	S20 H	E18 HB3	6.987	1.563	S20 H	P19 HB3	6.987	1.958
S20 H	E18 HB2	6.987	2.098	S20 H	E18 HB3	6.987	1.563	S20 H	P19 HB3	6.987	1.958
S20 H	E18 HB2	6.987	2.098	S20 H	P19 HB3	6.987	1.958	S20 H	E18 HB2	6.987	2.098
S20 H	S20 HB3	6.987	4.107	S20 H	S20 HB2	6.987	3.746	S20 H	S20 HA	6.987	4.320
S20 H	D21 H	6.987	7.996	E18 H	E18 HA	8.661	5.011	V17 H	V17 HB	8.868	2.283
V17 H	V17 HG2	8.868	0.390	E16 H	E16 HB3	8.070	1.793	E16 H	E16 HB2	8.070	1.876



**Table 6.2:** – continued from last page

Atom(1)	Atom(2)	cs(1)	cs(2)	Atom(1)	Atom(2)	cs(1)	cs(2)	Atom(1)	Atom(2)	cs(1)	cs(2)
E16 H	E16 HG2	8.070	2.177	E16 H	E16 HA	8.070	4.842	L15 H	F4 HA	8.670	5.566
L15 H	T14 HA	8.670	4.914	T14 H	I13 HA	8.634	4.466	I13 H	I13 HG12	9.490	1.060
I13 H	I13 HG2	9.490	0.829	I13 H	I13 HB	9.490	1.836	I13 H	T12 HB	9.490	3.903
I13 H	K6 HA	9.490	5.244	I13 H	I13 HA	9.490	4.466	I13 H	T12 HA	9.490	5.009
T12 H	T12 HB	8.535	3.903	T12 H	K11 HA	8.535	4.310	T12 H	T12 HA	8.535	5.009
K11 H	K11 HB3	7.225	1.749	K11 H	K11 HB2	7.225	1.598	G10 H	G10 HA2	7.776	3.547
L8 H	T7 HG2	8.991	1.134	L8 H	L8 HD1	8.991	1.004	L8 H	L8 HD2	8.991	0.931
L8 H	L8 HB2	8.991	1.731	L8 H	T7 HA	8.991	4.911	L8 H	L8 HA	8.991	4.261
T7 H	K6 HA	8.672	5.244	T7 H	T7 HG2	8.672	1.134	K6 H	L67 H	8.914	9.348
K6 H	V5 HA	8.914	4.762	K6 H	H68 HA	8.914	5.115	K6 H	K6 HB2	8.914	1.347
K6 H	K6 HB3	8.914	1.647	K6 H	T66 HG2	8.914	0.903	K6 H	V5 HG1	8.914	0.643
V5 H	T12 HG2	9.248	1.031	V5 H	I13 H	9.248	9.490	V5 H	V5 HB	9.248	1.857
V5 H	V5 HG2	9.248	0.683	V5 H	F4 HB2	9.248	2.828	V5 H	F4 HA	9.248	5.566
F4 H	V5 H	8.548	9.248	F4 H	L67 H	8.548	9.348	F4 H	F4 HD1	8.548	7.022
F4 H	F4 HA	8.548	5.566	F4 H	T66 HA	8.548	5.237	F4 H	I3 HA	8.548	4.125
F4 H	E64 HA	8.548	3.294	F4 H	F4 HB2	8.548	2.828	F4 H	I3 HG2	8.548	0.582
I3 H	I3 HA	8.286	4.125	I3 H	Q2 HA	8.286	5.225	I3 H	V17 HG2	8.286	0.390
Q2 H	Q2 HA	8.855	5.225	Q2 H	K63 HA	8.855	3.928	Q2 H	Q2 HB3	8.855	1.592

**Table 6.3:** Identified NOE transfer peak between amide protons of the membrane protein OmpX in bicelles consisting of DMPC and DHPC in a molar ratio of 1:2. For each NOE peak the involved residue pair is listed.

Atom(1)	Atom(2)	Atom(1)	Atom(2)	Atom(1)	Atom(2)	Atom(1)	Atom(2)
Thr 2	Ser 3	Thr 2	Glu 31	Thr 4	Tyr 30	Val 5	Tyr 146
Val 5	Arg 147	Gly 7	Gly 8	Gly 8	Asn 25	Tyr 9	Ala 10
Ala 10	Gln 11	Ala 10	Gly 23	Ala 10	Phe 24	Gln 11	Ser 12
Gln 11	Trp 140	Ser 12	Met 21	Asp 13	Ala 14	Ala 14	Gln 15
Gln 15	Ser 134	Gly 16	Gln 17	Gly 16	Met 18	Gln 17	Met 18
Met 18	Asn 19	Asn 19	Lys 20	Gly 22	Glu 47	Gly 22	Phe 23
Gly 22	Glu 47	Phe 23	Asn 24	Phe 23	Tyr 46	Asn 24	Thr 45
Leu 25	Lys 26	Lys 26	Tyr 27	Tyr 27	Ile 40	Tyr 27	Gly 41
Tyr 27	Ser 42	Tyr 30	Val 39	Tyr 30	Glu 31	Glu 31	Glu 32
Glu 32	Asn 33	Glu 32	Ser 35	Asp 33	Asn 34	Asp 33	Ser 35
Asn 34	Ser 35	Gly 38	Ala 70	Ile 40	Gly 68	Ser 42	Thr 66
Tyr 45	Thr 46	Lys 48	Ser 49	Arg 50	Thr 51	Arg 50	Asn 58
Arg 50	Lys 59	Ser 54	Gly 55	Gly 55	Asp 56	Asp 56	Tyr 57
Gln 61	Tyr 62	Tyr 62	Tyr 63	Tyr 63	Tyr 87	Ile 65	Val 85
Ala 67	Val 83	Ala 67	Gly 84	Gly 68	Gly 81	Ala 70	Tyr 71
Tyr 71	Arg 72	Tyr 71	Ile 79	Tyr 71	Tyr 80	Arg 72	Ile 79
Ile 73	Asn 74	Ile 73	Ala 77	Ile 73	Ile 79	Asn 74	Ala 77

**Table 6.3:** Fortsetzung.

Atom(1)	Atom(2)	Atom(1)	Atom(2)	Atom(1)	Atom(2)	Atom(1)	Atom(2)
Asp 75	Trp 76	Asp 75	Ala 77	Trp 76	Ala 77	Ser 78	Gln 114
Ile 70	Gn 114	Tyr 80	Gly 81	Gly 80	Gly 112	Gly 81	Val 82
Val 82	Gly 110	Val 83	Gly 84	Gly 86	Gly 106	Gly 88	Lys 89
Gly 88	Asp 104	Ile 92	Thr 93	Thr 93	Phe 94	Phe 94	Tyr 95
Ser 103	Asp 104	Phe 107	Arg 131	Gly 112	Leu 113	Leu 113	Gln 114
Leu 113	Phe 125	Gln 114	Phe 115	Phe 115	Asn 116	Phe 115	Leu 123
Asn 116	Leu 123	Pro 117	Met 118	Met 118	Glu 119	Met 118	Asn 120
Met 118	Val 121	Glu 119	Asn 120	Asn 120	Val 121	Ala 122	Leu123
Ala 122	Gly 145	Leu 123	Gly 145	Asp 124	Gly 143	Ser 126	Tyr 127
Ser 126	Ile 141	Ser 126	Ala 142	Glu 128	Trp 140	Ser 130	Arg 131
Ser 130	Val 137	Arg 131	Ile 132	Ile 132	Arg 133	Ile 132	Ser 134
Ile 132	Val 135	Arg 133	Ser 134	Arg 133	Val 135	Ser 134	Val 135
Asp 136	Val 137	Val 137	Gly 138	Trp140	Ile 141	Ile 141	Ala 142
Ala 142	Gly 143	Gly 143	Val 144	Arg 147	Phe 148		

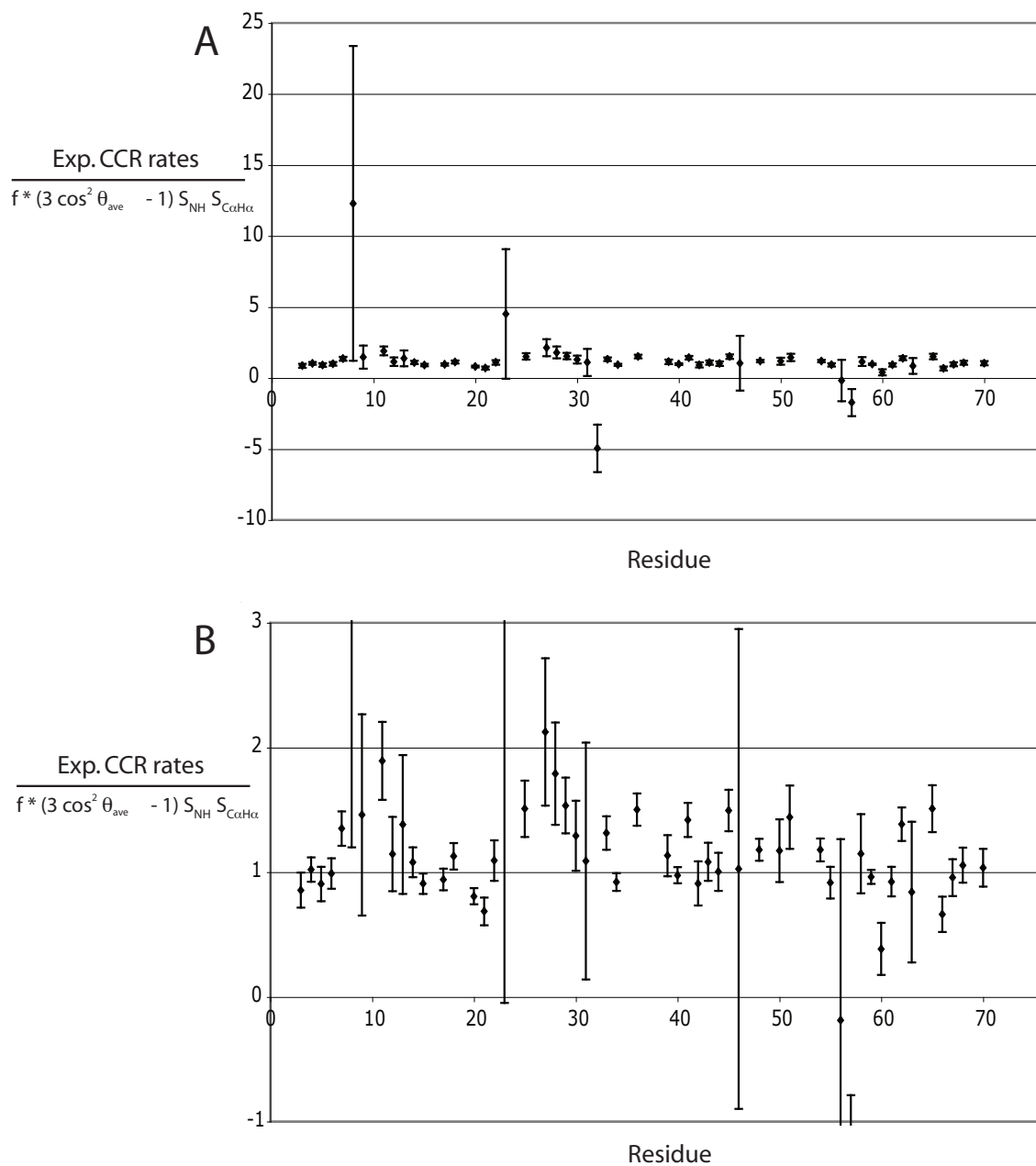


**Figure 6.2:** Graph A shows the quotient of the experimental CCR rates of NH - C $\alpha$ H $\alpha$  pairs in the protein backbone of ubiquitin divided by the theoretical CCR rates back calculated from the average inter vector angles of the ERNST ensemble (pdb code: 2kox) [42]. The prefactor  $f$  equals  $(\frac{\mu_0}{4\pi})^2 \cdot (\frac{\hbar}{2\pi})^2 \cdot \frac{\gamma_N \cdot \gamma_H}{r_{\text{NH}}^3} \cdot \frac{\gamma_C \cdot \gamma_H}{r_{\text{C}\alpha\text{H}\alpha}^3} \cdot \frac{2}{5} \cdot \tau_c$ . A quotient of 1 would indicate the case that all motion of the two internuclear vectors is correlated in a way that the inter vector angle stays constant. Graph B shows a zoom window of graph A which shows the region around a quotient of 1.

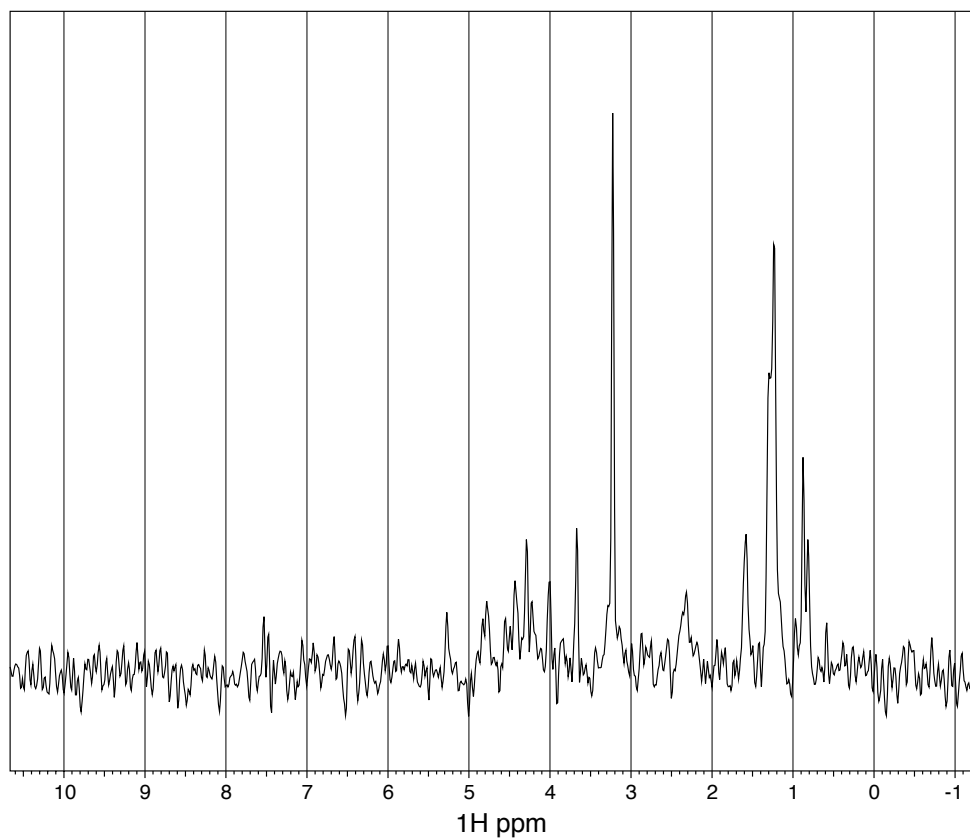


**Figure 6.3:** The 1D -  $^1\text{H}$  spectrum of the membrane protein OmpX in bicelles consisting of DMPC and DHPC in a molar ratio of 3:1. The measurement was conducted at a Bruker 900 MHz Spektrometer using a PH high-resolution magic angle spinning (HR-MAS) probe head. The small sample volume of the HR-MAS spinner and the strong induced residual dipolar couplings lead to a very weak signal to noise ratio.

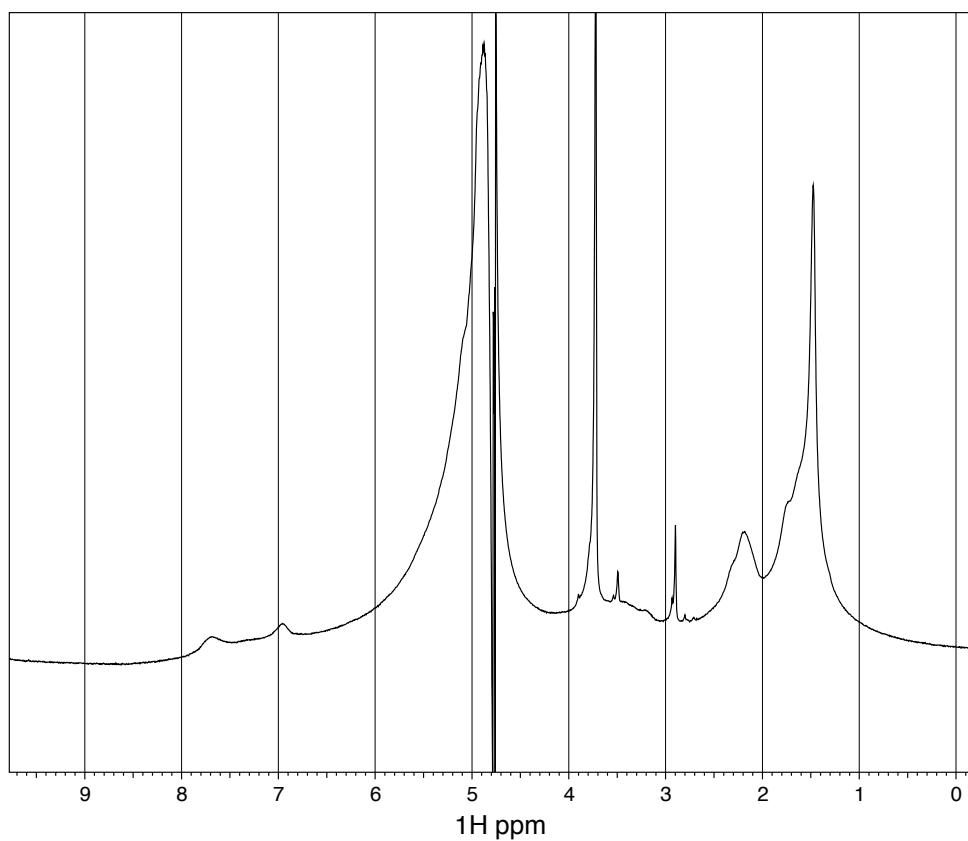


**Figure 6.4:** The 1D -  $^1\text{H}$  spectrum of bicelles consisting of DMPC and DHPC in a molar ratio of 1:2 in a polyacrylamide gel as described in section 4.3.2. The measurement was conducted at a Bruker 400 MHz Spektrometer using a TXI probe head. At the time point of the measurement a large amount of white precipitate with a very heterogeneous distribution was visible in the gel. The heterogeneity across the sample volume causes a strong broadening of the peaks.

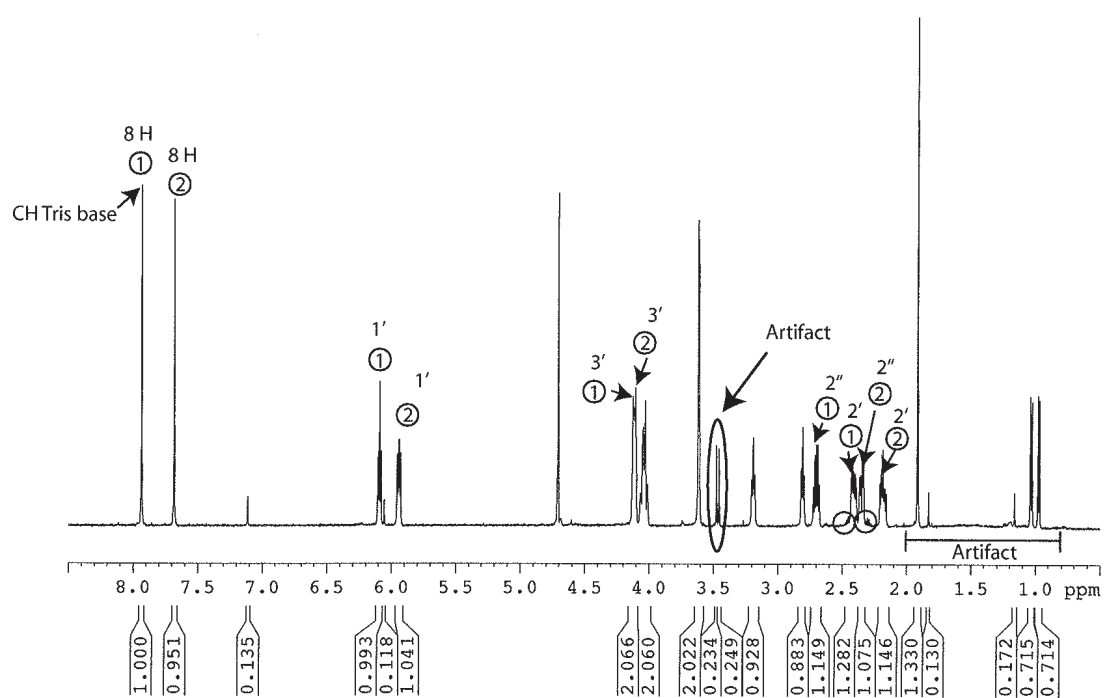


**Figure 6.5:** The 1D -  $^1H$  spectrum of the DNA-nanotubes used as an alignment medium. The measurement was conducted at a Bruker 400 MHz Spektrometer using a TXI probe head. Several signals from impurities, especially in the range of 0 - 2 ppm and at 3.45 ppm, are visible. This spectrum was measured by Dr. Donghan Lee.

# Bibliography

- [1] A. G. Palmer. NMR characterization of the dynamics of biomacromolecules, *Chem. Rev.* **2004**, *104*, 3623–3640.
- [2] D. M. Schneider, M. J. Dellwo, A. J. Wand. Fast internal main-chain dynamics of human ubiquitin, *Biochemistry* **1992**, *31*, 3645–3652.
- [3] Z. G. Li, S. Raychaudhuri, A. J. Wand. Insights into the local residual entropy of proteins provided by NMR relaxation, *Protein Sci.* **1996**, *5*, 2647–2650.
- [4] J. J. Prompers and R. Brüschweiler. Thermodynamic interpretation of NMR relaxation parameters in proteins in the presence of motional correlations, *J. Phys. Chem. B* **2000**, *104*, 11416–11424.
- [5] D. M. Schneider, M. J. Dellwo, A. J. Wand. Fast internal main-chain dynamics of human ubiquitin, *Biochemistry* **1992**, *31*, 3645–3652.
- [6] Z. G. Li, S. Raychaudhuri, A. J. Wand. Insights into the local residual entropy of proteins provided by NMR relaxation, *Protein Sci.* **1996**, *5*, 2647–2650.
- [7] A. L. Lee and A. J. Wand. Microscopic origins of entropy, heat capacity and the glass transition in proteins, *Nature* **2001**, *411*, 501–504.
- [8] J. J. Prompers and R. Brüschweiler. Thermodynamic interpretation of NMR relaxation parameters in proteins in the presence of motional correlations, *J. Phys. Chem. B* **2000**, *104*, 11416–11424.
- [9] C. Dellago and P. G. Bolhuis. Transition path sampling simulations of biological systems, *Top. Curr. Chem.* **2007**, *268*, 291–317.
- [10] D. Hamelberg, J. Mongan, J. A. McCammon. Accelerated molecular dynamics: a promising and efficient simulation method for biomolecules, *J. Chem. Phys.* **2004**, *120*, 11919–11929.
- [11] E. Paci and M. Karplus. Forced unfolding of fibronectin type 3 modules: an analysis by biased molecular dynamics simulations, *J. Mol. Biol.* **1999**, *288*, 441–459.
- [12] B. Roux. The calculation of the potential of mean force using computer simulations, *Comput. Phys. Commun.* **1995**, *91*, 275–282.
- [13] J. Schlitter, M. Engels, P. Kruger, E. Jacoby, A. Wollmer. Targeted molecular-dynamics simulation of conformational change - application to the T-R transition in insulin, *Mol. Simul.* **1993**, *10*, 291–308.

- [14] M. Akke and A. G. Palmer. Monitoring macromolecular motions on microsecond to millisecond time scales by R1 $\rho$ -R1 constant relaxation time NMR spectroscopy, *J. Am. Chem. Soc.* **1996**, *118*, 911–912.
- [15] L. E. Kay. Protein dynamics from NMR, *Nat. Struct. Biol.* **1998**, *5*, 513–517.
- [16] L. E. Kay, D. A. Torchia, A. Bax. Backbone dynamics of proteins as studied by <sup>15</sup>N inverse detected heteronuclear NMR spectroscopy: application to staphylococcal nuclease, *Biochemistry* **1989**, *28*, 8972–8979.
- [17] K. A. Henzler-Wildman, M. Lei, V. Tai, S. J. Kerns, M. Karplus, C. G. Hübner, D. Kern. A hierarchy of time scales in protein dynamics is linked to enzyme catalysis, *Nature* **2007**, *450*, 913–927.
- [18] F. Massi, M. J. Grey, A. G. Palmer. Microsecond timescale backbone conformational dynamics in ubiquitin studied with NMR R-1 $\rho$  relaxation experiments, *Protein Sci.* **2005**, *14*, 735–742.
- [19] K. A. Henzler-Wildman, V. Tai, M. Lei, M. Ott, M. Wolf-Watz, T. Fenn, E. Pozharski, M. A. Wilson, G. A. Petsko, M. Karplus, C. G. Hübner, D. Kern. Intrinsic motions along an enzymatic reaction trajectory, *Nature* **2007**, *450*, 838–844.
- [20] E. Z. Eisenmesser, O. Millet, W. Labeikovsky, D. M. Korzhnev, M. Wolf-Watz, D. A. Bosco, J. J. Skalicky, L. E. Kay, D. Kern. Intrinsic dynamics of an enzyme underlies catalysis, *Nature* **2005**, *438*, 117–121.
- [21] E. Z. Eisenmesser, O. Millet, W. Labeikovsky, D. M. Korzhnev, M. Wolf-Watz, D. A. Bosco, J. J. Skalicky, L. E. Kay, D. Kern. Intrinsic dynamics of an enzyme underlies catalysis, *Nature* **2005**, *438*, 117–121.
- [22] D. Kern, K. A. Henzler-Wildman, M. Wolf-Watz. Enzyme dynamics during catalysis measured by NMR spectroscopy, *Methods Enzymol* **2005**, *394*, 507–524.
- [23] D. Kern and E. R. P. Zuiderweg. The role of dynamics in allosteric regulation, *Curr. Opin. Struct. Biol.* **2003**, *13*, 748–757.
- [24] F. A. A. Mulder, B. Hon, A. Mittermaier, F. W. Dahlquist, L. E. Kay. Slow internal dynamics in proteins: application of NMR relaxation dispersion spectroscopy to methyl groups in a cavity mutant of T4 lysozyme, *J. Am. Chem. Soc.* **2002**, *124*, 1443–1451.
- [25] M. Tollinger, N. R. Skrynnikov, F. A. A. Mulder, J. D. Forman-Kay, L. E. Kay. Slow dynamics in folded and unfolded states of an SH3 domain, *J. Am. Chem. Soc.* **2001**, *123*, 11341–11352.
- [26] S. Y. Stevens, S. Sanker, C. Kent, E. R. P. Zuiderweg. Delineation of the allosteric mechanism of a cytidylyltransferase exhibiting negative cooperativity, *Nat. Struct. Biol.* **2001**, *8*, 947–952.
- [27] S. W. Englander. Hydrogen exchange and mass spectrometry: a historical perspective, *J. Am. Soc. Mass Spectrom.* **2006**, *17*, 1481–1489.



- [28] Y. W. Bai. Protein folding pathways studied by pulsed- and native-state hydrogen exchange, *Chem. Rev.* **2006**, *106*, 1757–1768.
- [29] M. Blackledge. Recent progress in the study of biomolecular structure and dynamics in solution from residual dipolar couplings, *Prog. Nucl. Reson. Spectrosc.* **2005**, *46*, 23–61.
- [30] J. R. Tolman and K. Ruan. NMR residual dipolar couplings as probes of biomolecular dynamics, *Chem. Rev.* **2006**, *106*, 1720–1736.
- [31] M. N. Triba, D. E. Warschawski, P. F. Devaux. Reinvestigation by phosphorus NMR of lipid distribution in bicelles, *Biophys. J.* **2005**, *88*, 1887–1901.
- [32] M. Ruckert and G. Otting. Alignment of biological macromolecules in novel non-ionic liquid crystalline media for NMR experiments, *J. Am. Chem. Soc.* **2000**, *122*, 7793–7797.
- [33] B. W. Koenig, J. S. Hu, M. Ottiger, S. Bose, R. W. Hendler, A. Bax. NMR measurement of dipolar couplings in proteins aligned by transient binding to purple membrane fragments, *J. Am. Chem. Soc.* **1999**, *121*, 1385–1386.
- [34] L. G. Barrientos, C. Dolan, A. M. Gronenborn. Characterization of surfactant liquid crystal phases suitable for molecular alignment and measurement of dipolar couplings, *J. Biomol. NMR* **2000**, *16*, 329–337.
- [35] M. Zweckstetter and A. Bax. Characterization of molecular alignment in aqueous suspensions of Pf1 bacteriophage, *J. Biomol. NMR* **2001**, *20*, 365–377.
- [36] H. J. Sass, G. Musco, S. J. Stahl, P. T. Wingfield, S. Grzesiek. Solution NMR of proteins within polyacrylamide gels: Diffusional properties and residual alignment by mechanical stress or embedding of oriented purple membranes, *J. Biomol. NMR* **2000**, *18*, 303–309.
- [37] O. F. Lange, N. A. Lakomek, C. Fares, G. F. Schroder, K. F. A. Walter, S. Becker, J. Meiler, H. Grubmuller, C. Griesinger, B. L. de Groot. Recognition dynamics up to microseconds revealed from an RDC-derived ubiquitin ensemble in solution, *Science* **2008**, *320*, 1471–1475.
- [38] Q. Zhang, A. C. Stelzer, C. K. Fisher, H. M. Al-Hashimi, *Nature* **2007**, *450*, 1263–1268.
- [39] H. M. Al-Hashimi, S. W. Pitt, A. Majumdar, W. Xu, D. J. Patel. Mg<sup>2+</sup>-induced variations in the conformation and dynamics of HIV-1 TAR RNA probed using NMR residual dipolar couplings, *J. Mol. Biol.* **2003**, *329*, 867–873.
- [40] S. W. Pitt, A. Majumdar, A. Serganov, D. J. Patel, H. M. Al-Hashimi. Argininamide binding arrests global motions in HIV-1 Tar RNA: comparison with Mg<sup>2+</sup>-induced conformational stabilization, *J. Mol. Biol.* **2004**, *338*, 7–16.
- [41] S. W. Pitt, Q. Zhang, D. J. Patel, H. M. Al-Hashimi. Evidence that electrostatic interactions dictate the ligand-induced arrest of RNA global flexibility, *Angew. Chem. Int. Ed.* **2005**, *44*, 3412–3415.

- [42] R. B. Fenwick, S. Esteban-Martin, B. Richter, D. Lee, K. F. A. Walter, D. Milovanovic, S. Becker, N. A. Lakomek, C. Griesinger, X. Salvatella. NMR residual dipolar couplings identify long range correlated motions in the backbone of the protein ubiquitin *J. Am. Chem. Soc.* **2011**, *133*, 10336–10339.
- [43] G. Bouvignies, P. Bernado, S. Meier, K. Cho, S. Grzesiek, S. Brüschweiler, M. Blackledge. Identification of slow correlated motions in proteins using residual dipolar and hydrogen-bond scalar couplings, *Proc. Natl Acad. Sci. USA* **2005**, *102*, 13885–13890.
- [44] G. Bouvignies, P. R. L. Markwick, S. Brüschweiler, M. Blackledge. Characterization of protein dynamics from residual dipolar couplings using the three dimensional Gaussian axial fluctuation model, *Proteins* **2008**, *71*, 353–363.
- [45] J. R. Tolman. A novel approach to the retrieval of structural and dynamic information from residual dipolar couplings using several oriented media in biomolecular NMR spectroscopy, *J. Am. Chem. Soc.* **2002**, *124*, 12020–12030.
- [46] W. Peti, J. Meiler, R. Brüschweiler, C. Griesinger. Model-free analysis of protein backbone motion from residual dipolar couplings, *J. Am. Chem. Soc.* **2002**, *124*, 5822–5833.
- [47] J. Meiler, J. J. Prompers, W. Peti, C. Griesinger, R. Brüschweiler. Model-free approach to the dynamic interpretation of residual dipolar couplings in globular proteins, *J. Am. Chem. Soc.* **2001**, *123*, 6098–6107.
- [48] N. A. Lakomek, T. Carlomagno, S. Becker, C. Griesinger, J. Meiler. A thorough dynamic interpretation of residual dipolar couplings in ubiquitin, *J. Biomol. NMR* **2006**, *34*, 101–115.
- [49] N. A. Lakomek, K. F. A. Walter, C. Fares, O. F. Lange, B. L. de Groot, H. Grubmüller, R. Brüschweiler, A. Munk, S. Becker, J. Meiler, C. Griesinger. Self-consistent residual dipolar coupling based model-free analysis for the robust determination of nanosecond to microsecond protein dynamics, *J. Biomol. NMR* **2008**, *41*, 139–155.
- [50] M. Zweckstetter and A. Bax. Evaluation of uncertainty in alignment tensors obtained from dipolar couplings, *J. Biomol. NMR* **2002**, *23*, 1271–137.
- [51] G. Bouvignies, P. Bernado, M. Blackledge. Protein backbone dynamics from NH-NH dipolar couplings in partially aligned systems: a comparison of motional models in the presence of structural noise, *J. Mag. Res.* **2005**, *173*, 328–338.
- [52] G. M. Clore. How much backbone motion in ubiquitin is required to account for dipolar coupling data measured in multiple alignment media as assessed by independent cross-validation, *J. Am. Chem. Soc.* **2004**, *126*, 2923–2938.
- [53] G. M. Clore and C. D. Schwieters. Concordance of residual dipolar couplings, backbone order parameters and crystallographic B-factors for a small  $\alpha/\beta$  protein: a unified picture of high probability, fast atomic motions in proteins, *J. Mol. Biol.* **2006**, *355*, 879–886.

- [54] B. Reif, A. Diener, M. Hennig, M. Maurer, C. Griesinger. Cross-correlated relaxation for the measurement of angles between tensorial interactions, *J. Mag. Res.* **2000**, *143*, 45–68.
- [55] I. C. Felli, C. Richter, C. Griesinger, H. Schwalbe. Determination of RNA sugar pucker mode from cross-correlated relaxation in solution NMR spectroscopy, *J. Am. Chem. Soc.* **1999**, *121*, 1956–1957.
- [56] B. Vogeli. Comprehensive description of NMR cross-correlated relaxation under anisotropic molecular tumbling and correlated local dynamics on all time scales, *J. Chem. Phys.* **2010**, *133*, 014501.
- [57] D. Frueh. Internal motions in proteins and interference effects in nuclear magnetic resonance, *Prog. Nucl. Mag. Res. Sp.* **2002**, *41*, 305–324.
- [58] P. Pelupessy, S. Ravindranathan, G. Bodenhausen. Correlated motions of successive amide N-H bonds in proteins, *J. Biomol. NMR* **2003**, *25*, 265–280.
- [59] P. Lundström, F. A., Mulder, M. Akke. Correlated dynamics of consecutive residues reveal transient and cooperative unfolding of secondary structure in proteins, *Proc. Natl Acad. Sci. USA* **2005**, *102*, 16984–16989.
- [60] B. Vogeli. Comprehensive description of NMR cross-correlated relaxation under anisotropic molecular tumbling and correlated local dynamics on all time scales, *J. Chem. Phys.* **2010**, *133*, 014501.
- [61] B. Vogeli and L. Yao. Correlated dynamics between protein HN and HC bonds observed by NMR cross relaxation, *J. Am. Chem. Soc.* **2009**, *131*, 3668–3678.
- [62] I. Solomon. Relaxation processes in a system of 2 spins, *Phys. Rev.* **1955**, *2*, 559–565.
- [63] J. Boisbouvier and A. Bax. Long-range magnetization transfer between uncoupled nuclei by dipole-dipole cross-correlated relaxation: A precise probe of  $\beta$ -sheet geometry in proteins, *J. Am. Chem. Soc.* **2002**, *124*, 11038–11045.
- [64] B. Vogeli, T. F. Segawa, D. Leitz, A. Sobol, A. Choutko, D. Trzesniak, W. van Gunsteren, R. Riek. Exact distances and internal dynamics of perdeuterated ubiquitin from NOE buildups, *Proc. Natl Acad. Sci. USA* **2002**, *124*, 13533–13537.
- [65] D. Leitz, B. Vogeli, J. Greenwald, R. Riek. Temperature dependence of  $^1H_N - ^1H_N$  distances in ubiquitin as studied by exact measurements of NOEs, *Proc. Natl Acad. Sci. USA* **2002**, *124*, 13533–13537.
- [66] D. W. A. Buchan, A. J. Shepherd, C. Lee, F. M. G. Pearl, S. C. G. Rison, J. M. Thornton, C. A. Orengo. Gene3D: Structural assignment for whole genes and genomes using the CATH domain structure database, *Genome Res.* **2002**, *12*, 503–514.
- [67] A. Arora, F. Abildgaard, J. H. Bushweller, L. K. Tamm. Structure of outer membrane protein A transmembrane domain by NMR spectroscopy, *Nat. Struct. Biol.* **2001**, *8*, 334–338.

- [68] C. Fernandez, K. Adeishvili, K. Wuthrich. Transverse relaxation-optimized NMR spectroscopy with the outer membrane protein OmpX in dihexanoyl phosphatidylcholine micelles, *Proc. Natl Acad. Sci. USA* **2001**, *98*, 2358–2363.
- [69] P. M. Hwang, W. Y. Choy, E. I. Lo, L. Chen, J. D. Forman-Kay, C. R. Raetz, G. G. Prive, R. E. Bishop, L. E. Kay. Solution structure and dynamics of the outer membrane enzyme PagP by NMR, *Proc. Natl Acad. Sci. USA* **2002**, *99*, 13560–13565.
- [70] B. Liang and L. K. Tamm. Structure of outer membrane protein G by solution NMR spectroscopy, *Proc. Natl Acad. Sci. USA* **2007**, *104*, 16140–16145.
- [71] C. Fernandez, C. Hilty, G. Wider, K. Wuthrich. Lipid-protein interactions in DHPC micelles containing the integral membrane protein OmpX investigated by NMR spectroscopy, *Proc. Natl Acad. Sci. USA* **2002**, *124*, 13533–13537.
- [72] J. J. Chou, J. D. Kaufman, S. J. Stahl, P. T. Wingfield, A. Bax. Micelle-induced curvature in a water-insoluble HIV-1 Env peptide revealed by NMR dipolar coupling measurement in stretched polyacrylamide gel, *J. Am. Chem. Soc.* **2002**, *124*, 2450–2451.
- [73] E. E. Mathews, M. Zoonens, D. M. Engelman. Dynamic helix interactions in transmembrane signaling, *Cell* **2006**, *127*, 447–450.
- [74] C. R. Sanders and G. C. Landis. Reconstitution of membrane-proteins into lipid-rich bilayered mixed micelles for NMR-studies, *Biochemistry* **1995**, *34*, 4030–4040.
- [75] J. A. Whiles, R. Deems, R. R. Vold, E. A. Dennis. Bicelles in structure-function studies of membrane-associated proteins, *Bioorg. Chem.* **2002**, *30*, 431–442.
- [76] R. R. Vold, R. S. Prosser, A. J. Deese. Isotropic solutions of phospholipid bicelles: A new membrane mimetic for high-resolution NMR studies of polypeptides, *J. Biomol. NMR* **1997**, *9*, 329–335.
- [77] K. J. Glover, J. A. Whiles, G. Wu, N. Yu, R. Deems, J. O. Struppe, R. E. Stark, E. A. Komives, R. R. Vold. Structural evaluation of phospholipid bicelles for solution-state studies of membrane-associated biomolecules, *Biophys. J.* **2001**, *81*, 2163–2171.
- [78] S. Gaemers and A. Bax. Morphology of three lyotropic liquid crystalline biological NMRmedia studied by translational diffusion anisotropy, *J. Am. Chem. Soc.* **2001**, *123*, 12343–12352.
- [79] E. V. Bocharov, Y. E. Pustovalova, K. V. Pavlov, P. E. Volynsky, M. V. Goncharuk, Y. S. Ermolyuk, D. V. Karpunin, A. A. Schulga, M. P. Kirpichnikov, R. G. Efremov, I. V. Maslennikov, A. Arseniev. Unique dimeric structure of BNip3 transmembrane domain suggests membrane permeabilization as a cell death trigger, *J. Biol. Chem.* **2007**, *282*, 16256–16266.
- [80] K. J. Glover, J. A. Whiles, R. R. Vold, G. Melacini. Position of residues in transmembrane peptides with respect to the lipid bilayer: A combined lipid NOEs and water chemical exchange approach in phospholipid bicelles, *J. Biomol. NMR* **2002**, *22*, 57–64.

- [81] E. V. Bocharov, K. S. Mineev, P. E. Volynsky, Y. S. Ermolyuk, E. N. Tkach, A. G. Sobol, V. V. Chupin, M. P. Kirpichnikov, R. G. Efremov, A. Arseniev. Spatial structure and pH-dependent conformational diversity of dimeric transmembrane domain of the receptor tyrosine kinase EphA1, *J. Biol. Chem.* **2008**, *283*, 6950–6956.
- [82] J. Vogt and G. E. Schulz. The structure of the outer membrane protein OmpX from *Escherichia coli* reveals possible mechanisms of virulence, *Structure with Folding & Design* **1999**, *7*, 1301–1309.
- [83] B. Richter, J. Gsponer, P. Varnai, X. Salvatella, M. Vendruscolo, The MUMO (minimal under-restraining minimal over-restraining) method for the determination of native state ensembles of proteins. *J. Biomol. NMR* **2007**, *37*, 117–135.
- [84] K. Lindorff-Larsen, R. B. Best, M. A. Depristo, C. M. Dobson, M. Vendruscolo. Simultaneous determination of protein structure and dynamics, *Nature* **2005**, *433*, 128–132.
- [85] J. R. Tolman. A novel approach to the retrieval of structural and dynamic information from residual dipolar couplings using several oriented media in biomolecular NMR spectroscopy, *J. Am. Chem. Soc.* **2002**, *124*, 12020–12030.
- [86] L. Yao, B. Voegeli, D. A. Torchia, A. Bax. Simultaneous NMR study of protein structure and dynamics using conservative mutagenesis, *J. Chem. Phys.* **2008**, *112*, 6045–6056.
- [87] T. S. Ulmer, D. A. Calderwood, M. H. Ginsberg, I. D. Campbell. Domain-specific interactions of talin with the membrane-proximal region of the integrin  $\beta 3$  subunit, *Biochemistry* **2003**, *42*, 8307–8312.
- [88] G. Bouvignies, P. Bernado, M. Blackledge. Identification of slow correlated motions in proteins using residual dipolar and hydrogen-bond scalar couplings, *Proc. Natl. Acad. Sci. USA* **2005**, *102*, 13885–13890.
- [89] K. Walter. Determination of the dynamic of ubiquitin in solution by orientation dependent NMR parameters, diploma thesis, 2005.
- [90] E. M. Johnson, G. A. Lazar, J. R. Desjarlais, T. M. Handel. Solution structure and dynamics of a designed hydrophobic core variant of ubiquitin, *Structure Fold Des* **1999**, *7*, 967–976.
- [91] T. Cierpicki and J. H. Bushweller. Charged gels as orienting media for measurement of residual dipolar couplings in soluble and integral membrane proteins, *J. Am. Chem Soc.* **2004**, *126*, 16259–16266.
- [92] C. R. Sanders, J. H. Prestegard. Magnetically orientable phospholipid bilayers containing small amounts of a bile salt analogue, CHAPSO, *Biophys. J.* **1990**, *58*, 447–460.
- [93] G. Cornilescu, J. L. Marquardt, M. Ottiger, A. Bax. Validation of protein structure from anisotropic carbonyl chemical shifts in a dilute liquid crystalline phase, *J. Am. Chem. Soc.* **1998**, *120*, 6836–6837.

- [94] M. Ottiger and A. Bax. Determination of relative N-H(N), N-C', Ca-C' and  $C\alpha-H\alpha$  effective bond length in a protein by NMR in a dilute liquid crystalline phase, *J. Am. Chem. Soc.* **1998**, *120*, 12334–12341.
- [95] K. B. Briggman and J. R. Tolman. De novo determination of bond orientations and order parameters from residual dipolar couplings with high accuracy, *J. Am. Chem. Soc.* **2003**, *125*, 10164–10165.
- [96] K. Ruan and J. R. Tolman. Composite alignment media for the measurement of independent sets of NMR residual dipolar couplings, *J. Am. Chem. Soc.* **2005**, *127*, 15032–15033.
- [97] R. Ramage, J. Green, T. W. Muir, O. M. Ogunjobi, S. Love, K. Shaw. Synthetic, structural and biological studies of the ubiquitin system: the total chemical synthesis of ubiquitin, *Biochem. J.* **1994**, *299*, 151–158.
- [98] C. A. Rohl, C. E. M. Strauss, K. M. S. Misura. Protein structure prediction using Rosetta, *Numerical computer methods* **2004**, *383*, 66–93.
- [99] R. Das and D. Baker. Macromolecular modeling with Rosetta, *Annu. Rev. Biochem.* **2008**, *77*, 363–382.
- [100] M. Zweckstetter and A. Bax. Prediction of sterically induced alignment in a dilute liquid crystalline phase: Aid to protein structure determination by NMR, *J. Am. Chem. Soc.* **2000**, *122*, 3791–3792.
- [101] J. C. Hus and R. Bruschweiler. Principal component method for assessing structural heterogeneity across multiple alignment media, *J. Biomol. NMR* **2002**, *24*, 123–132.
- [102] J. C. Hus, W. Peti, C. Griesinger, R. Bruschweiler. Self-consistency analysis of dipolar couplings in multiple alignment of ubiquitin, *J. Am. Chem. Soc.* **2003**, *125*, 5596–5597.
- [103] K. A. Dill and H. S. Chan. From Levinthal to pathways to funnels, *Nat. Struc. Biol.* **1997**, *4*, 10–19.
- [104] G. M. Clore and C. D. Schwieters. Amplitudes of protein backbone dynamics and correlated motions in a small a / b protein: correspondence of dipolar coupling and heteronuclear relaxation measurements, *Biochemistry* **2004**, *43*, 10678–10691.
- [105] V. Sklenar, M. Piotto, R. Leppik, V. Saudek. Gradient-tailored water suppression for  $^1\text{H}-^{15}\text{N}$  HSQC experiments optimized to retain full sensitivity, *J. Magn. Res.* **1993**, *102*, 241–245.
- [106] F. Delaglio, S. Grzesiek, G. W. Vuister, G. Zhu, J. Pfeifer, A. Bax. NMRPipe: A multidimensional spectral processing system based on UNIX pipes, *J. Biomol. NMR* **1995**, *6*, 2770–293.
- [107] R. Keller and K. Wuthrich, Computer-aided resonance assignment (CARA), Available from <http://www.nmr.ch>.
- [108] S. Vijay-Kumar, C. E. Bugg, W. J. Cook. Structure of ubiquitin refined at 1.8 Å resolution, *J. Mol. Biol.* **1987**, *194*, 531–544.

- [109] G. Cornilescu, J. L. Marquardt, M. Ottiger, A. Bax. Validation of protein structure from anisotropic carbonyl chemical shifts in a dilute liquid crystalline phase, *J. Am. Chem. Soc.* **1998**, *120*, 6836–6837.
- [110] S. Wimperis and G. Bodenhausen. Relaxation-allowed transfer of coherence in NMR between spins which are not scalar coupled, *Chem. phys. Lett.* **1987**, *140*, 41–45.
- [111] S. Wimperis and G. Bodenhausen. Relaxation-allowed cross-peaks in two dimensional NMR correlation spectroscopy, *Mol. Phys.* **1989**, *66*, 897–919.
- [112] R. Bruschweiler and R. R. Ernst. Molecular-dynamics monitored by cross-correlated cross relaxation of spins quantized along orthogonal axes, *J. Chem. Phys.* **1992**, *96*, 1758–1766.
- [113] S. J. F. Vincent and C. Zwahlen. Dipole-dipole cross-correlation at C-13 natural abundance: A structural tool for polysaccharides, *J. Am. Chem. Soc.* **2000**, *122*, 8307–8308.
- [114] N. K. Goto, K. H. Gardner, G. A. Mueller, R. C. Willis, L. E. Kay. A robust and cost-effective method for the production of Val, Leu, Ile (d1) methyl-protonated <sup>15</sup>N,<sup>13</sup>C,<sup>2</sup>H-labeled proteins, *J. Biomol. NMR* **1999**, *13*, 369–374.
- [115] P. Gans, O. Hamelin, R. Sounier, I. Ayala, M. A. Dura, C. D. Amero, M. Noirclerc-Savoie, B. Franzetti, M. J. Plevin, J. Boisbouvier. Stereospecific isotopic labeling of methyl groups for NMR spectroscopic studies of high-molecular-weight proteins, *Angew. Chem. Int. Ed.* **2010**, *49*, 1958–1962.
- [116] C. Griesinger, G. Otting, K. Wuthrich, R. R. Ernst. Clean TOCSY for proton spin system identification in macromolecules, *J. Am. Chem. Soc.* **1988**, *110*, 7870–7872.
- [117] T. Herrmann, P. Guntert, K. Wuthrich. Protein NMR structure determination with automated NOE-identification in the NOESY spectra using the new software AT-NOS, *J. Biomol. NMR* **2002**, *24*, 171–189.
- [118] T. Herrmann, P. Guntert, K. Wuthrich. Protein NMR structure determination with automated NOE assignment using the new software CANDID and the torsion angle dynamics algorithm DYANA, *J. Mol. Bio.* **2002**, *319*, 209–227.
- [119] T. D. Goddard and D. G. Kneller, SPARKY 3, University of California, San Francisco, USA.
- [120] C. Fernandez, K. Adeishvili, K. Wuthrich. Transverse relaxation-optimized NMR spectroscopy with the outer membrane protein OmpX in dihexanoyl phosphatidylcholine micelles, *Proc. Natl Acad. Sci. USA* **2001**, *98*, 2358–2363.
- [121] D. Lee, C. Hilty, G. Wider, K. Wuthrich. Effective rotational correlation times of proteins from NMR relaxation interference, *J. Mag. Res.* **2006**, *178*, 72–76.
- [122] K. Pervushin, R. Riek, G. Wider, K. Wuthrich. Attenuated T-2 relaxation by mutual cancellation of dipole-dipole coupling and chemical shift anisotropy indicates an avenue to NMR structures of very large biological macromolecules in solution, *Proc. Natl Acad. Sci. USA* **1997**, *94*, 12399–12371.

- [123] C. Hilty, G. Wider, C. Fernandez, K. Wuthrich. Membrane protein-lipid interactions in mixed micelles studied by NMR spectroscopy with the use of paramagnetic reagents, *Chem. Bio. Chem.* **2004**, *5*, 467–473.
- [124] L. Donghan, K. F. A. Walter, A. K. Bruckner, C. Hilty, S. Becker, C. Griesinger. Bilayer in small bicelles revealed by lipid-protein interactions using NMR spectroscopy, *J. Am. Chem. Soc.* **2008**, *130*, 13822–13823.
- [125] D. S. Wishart, B. D. Sykes, F. M. Richards. The chemical shift index: a fast and simple method for the assignment of protein secondary structure through NMR spectroscopy, *Biochemistry* **1992**, *31*, 1647–1651.
- [126] D. S. Wishart & B. D. Sykes. The C-13 chemical shift index - a simple method for the identification of protein secondary structure using a C-13 chemical shift data, *J. Biomol. NMR* **1994**, *4*, 171–180.
- [127] M. Schmidt, P. Haberz, A. Leonov, C. Griesinger. Future directions in NMR (INSA) (C. L. Khetrapal, A. Kumar, K. V. Ramanathan), Springer, Heidelberg, 2009, 93–100.
- [128] S. M. Douglas, J. J. Chou, W. M. Shih. DNA-nanotube-induced alignment of membrane proteins for NMR structure determination, *Proc. Natl Acad. Sci.* **2007**, *104*, 6644–6648.
- [129] J. Lorieau, L. Yao, A. Bax. Liquid crystalline phase of G-Tetrad DNA for NMR study of detergent-solubilized proteins, *J. Am. Chem. Soc.* **2008**, *130*, 7536–7537.
- [130] The PyMOL Molecular Graphics System, Version 1.3, Schrödinger, LLC.
- [131] L. R. Brown, C. Bosch, K. Wuthrich. Location and orientation relative to the micelle surface for glucagon in mixed micelles with dodecylphosphocholine EPR and NMR studies, *Biochim. Biophys. Acta* **1981**, *642*, 296–312.
- [132] C. H. M. Papavoine, R. N. H. Konings, C. W. Hilbers, F. J. M. van de Ven. Location of M13 coat protein in sodium dodecyl sulfated micelles as determined by NMR, *Biochemistry* **1994**, *33*, 12990–12997.
- [133] C. Fernandez, C. Hilty, S. Bonjour, K. Adeishvili, K. Pervushin, K. Wuthrich. Solution NMR studies of the integral membrane proteins OmpX and OmpA from *Escherichia coli*, *FEBS Letter* **2001**, *504*, 173–178.
- [134] R. R. Vold & R. S. Prosser. Magnetically oriented phospholipid bilayered micelles for structural studies of polypeptide. Does the ideal bicelle exist?, *J. Magn. Reson. Series B* **1996**, *113*, 267–271.



# Curriculum Vitae

<b>Name</b>	<b>Korvin Felix Andreas Walter</b>
Date of Birth	18th October 1982
Place of Birth	Rheine
Citizenship	German
<hr/>	
Since October 2007	PhD student in the department for NMR-based structural biology at the Max-Planck-Institut for biophysical chemistry
September 2007	Diploma in Chemistry
October 2005 – September 2007	Studies of Physics, Georg-August-University, Göttingen
April 2005 – September 2007	Studies of Chemistry, Georg-August-University, Göttingen
April 2003 – March 2005	Studies of Chemistry, Carl-von-Ossietzky-University, Oldenburg
July 2002 – March 2003	Military Service, Delmenhorst
June 2002	Abitur
<hr/>	

## Publications

D. Long, L. Da-Wei, K. F. A. Walter, C. Griesinger, R. Brüschweiler. Toward a predictive understanding of slow methyl group dynamics in proteins, *Biophys. J.*, **2011**, *101*, 910–915.

R. B. Fenwick, S. Esteban-Martin, B. Richter, D. Lee, K. F. A. Walter, D. Milovanovic, S. Becker, N. A. Lakomek, C. Griesinger, X. Salvatella. NMR residual dipolar couplings identify long range correlated motions in the backbone of the protein, *J. Am. Chem. Soc.*, **2011**, *133*, 10336–10339.

C. Fares, N. A. Lakomek, K. F. A. Walter, B. T. C. Frank, J. Meiler, S. Becker, C. Griesinger. Accessing the ns- $\mu$ s side chain dynamics in ubiquitin with methyl RDCs, *J. Biomol. NMR*, **2009**, *45*, 23–44.

L. Salmon, G. Bouvignies, P. Markwick, N. A. Lakomek, S. Showalter, D. W. Li, K. Walter, C. Griesinger, R. Bruschweiler, M. Blackledge. Protein conformational flexibility from structure-free analysis of NMR dipolar couplings: quantitative and absolute determination of backbone motion in ubiquitin, *Angew. Chem. Int. Ed.*, **2009**, *48*, 4154–4157.

H. Schmidt, S. Himmel, K. F. A. Walter, V. Klaukien, M. Funk, D. Lee. Transverse relaxation-optimized HCN experiment for tautomeric states of histidine sidechains, *J. Korean Mag. Res. Soc.*, **2008**, *12*, 89–95.

N. A. Lakomek, O. F. Lange, K. F. A. Walter, C. Fares, D. Egger, P. Lunkenheimer, J. Meiler, H. Grubmüller, S. Becker, B. L. de Groot, C. Griesinger. Residual dipolar couplings as a tool to study molecular recognition of ubiquitin, *Biochem. Soc. Trans.*, **2008**, *36*, 1433–1437

D. Lee, K. F. A. Walter, A. K. Brückner, C. Hilty, S. Becker, C. Griesinger. Bilayer in small bicelles revealed by lipid-protein interactions using NMR spectroscopy, *J. Am. Chem. Soc.*, **2008**, *130*, 13822–13823

N. A. Lakomek\*, K. F. A. Walter\*, C. Fares, O. F. Lange, B. L. de Groot, H. Grubmüller, R. Bruschweiler, A. Munk, S. Becker, J. Meiler, C. Griesinger. Self-consistent residual dipolar coupling based model-free analysis for the robust determination of nanosecond to microsecond protein dynamics, *J. Biomol. NMR*, **2008**, *41*, 139–155.

O. F. Lange, N. A. Lakomek, C. Fares, G. F. Schroder, K. F. A. Walter, S. Becker, J. Meiler, H. Grubmüller, C. Griesinger, B. L. de Groot. Recognition dynamics up to microseconds revealed from an RDC-derived ubiquitin ensemble in solution, *Science*, **2008**, *320*, 1471–1475.

\*= both authors contributed equally